DIEF - Dipartimento di Ingegneria Industriale

PhD School: *Energetica e Tecnologie Industriali e Ambientali Innovative*

Scientific Area: ING-IND/09

EXPERIMENTAL CHARACTERIZATION OF THE UNSTEADY INTERACTION BETWEEN EFFUSION COOLING AND SWIRLING FLOWS IN A GAS TURBINE COMBUSTOR MODEL

PhD Candidate: Ing. Tommaso Lenzi

Tutor: Prof. Ing. Bruno Facchini

Co-Tutor: Dott. Ing. Antonio Andreini

PhD School Coordinator: Prof. Ing. Giampaolo Manfrida

PhD School Cycle: XXXIII (2017-2020)

Contents

List of Figures

List of Tables

Abstract

The analysis of the interaction between the swirling and cooling flows, promoted by the liner film cooling system, is a fundamental task for the design of turbine combustion chambers since it influences different aspects such as emissions and cooling capability. The requirements for improving the modern gas turbine combustors are: swirler injectors for flame stabilization, increasingly higher temperature and pressure values, and an increased amount of air dedicated to the combustion process. All these aspects make the design of even more efficient cooling systems, and the correct estimation of liners heat load, a hard task. Experimental works in the literature have addressed the problem with dedicated test rigs using steady-state measurement techniques to analyze the interaction between swirling main flow and effusion cooling flow. However, the fluid dynamic mechanisms, which govern turbulent mixing between main and coolant, are the flow field instabilities. In particular high turbulence oscillations, eddies, and tangential velocity components induced by the swirling flow deeply affect the behavior of effusion cooling jets demanding for dedicated unsteady flow field (near-wall coolant sub-layer) and adiabatic effectiveness experimental analysis. For this reason the present research activity is aimed at an unsteady characterization of the turbulent interaction between effusion cooling and swirling flows in a gas turbine combustor model. The experimental setup of this work consists of a non-reactive single-sector linear combustor test rig scaled up with respect to engine dimensions to increase spatial resolution and reduce the frequencies of the unsteadiness. The test section was equipped with an effusion plate with standard inclined cylindrical holes to simulate the liner cooling system. The degree of swirl for a swirling flow is usually characterized by the swirl

number, Sn, defined as the ratio of the tangential momentum flux to axial momentum flux. To assess the impact of such parameter on the near-wall effusion behavior, a set of three different axial swirlers with swirl number equal to Sn = 0.6 - 0.8 - 1.0 were designed and tested in the experimental apparatus. The tests were also carried out by varying the feeding pressure drop of the effusion plate to evaluate the effect of this parameter.
During the first phase of the research, the rig was instrumented with a 2D Time-Resolved Particle Image Velocimetry system, focussing on different field of views. An analysis of the main flow field by varying the Sn was first performed in terms of average velocity, Root Mean Square, and turbulence related quantities like kinetic energy spectra and length scale information. In a second step, the analysis was focussed on the near-wall regions: the impact of Sn on the coolant jets was quantified in terms of vorticity analysis and jet oscillation, highlighting a strong effect of the swirl number on film behavior. Subsequently, film effectiveness was acquired using the Fast Response Pressure Sensitive Paint technique; the scale of the model and the acquisition frequency allowed to track the effusion jets unsteadiness. With both the measurement techniques, the collected results show the importance of using an unsteady analysis to perform an in-depth characterization of the mixing phenomena between the main flow and the coolant, which in significantly affected by the Sn value.

Nomenclature

Symbols

A	Area	$[m^2]$
BR	Blowing ratio	$[-]$
D	Diameter	$[m]$
DR	Density ratio	$[-]$
f	Frequency	$[Hz]$
h	Height	$[m]$
K	Turbulent kinetic energy	$[m^2/s^2]$
l,L	Length	$[m]$
Le	Lewis number	$[-]$
M	Mach number	$[-]$
MR	Momentum ratio	$[-]$
P	Pressure	$[Pa]$
Pr	Prandtl number	$[-]$

Re	Reynolds number	$[-]$
Sc	Schmidt number	$[-]$
S_n	Swirl number	$[-]$
S_x	Streamwise hole pitch	$[m]$
S_z	Spanwise hole pitch	$[m]$
t	Time	$[s]$
Tu	Turbulence intensity	$[-]$
u,U, v, V	Velocity	$[m/s]$
u'	Fluctuating Velocity	$[m/s]$
u_{ax}	Axial Velocity	$[m/s]$
u_x	x-Velocity	$[m/s]$
u_y	y-Velocity	$[m/s]$
u_z	z-Velocity	$[m/s]$
VR	Velocity Ratio	$[-]$
x,y,z	Cartesian coordinates	$[m]$

Greeks

α	Hole inclination angle	$[^\circ]$
η	Adiabatic effectiveness	$[-]$
μ	Dynamic viscosity	$[Pa \cdot s]$
ρ	Density	$[kg/m^3]$
τ	Time	$[s]$

Subscripts-Superscripts

$\bar{.}$	Time-averaged quantity
$.'$	Instantaneous quantity
ad	Adiabatic
air	Air
$cool$	Coolant
$dark$	Dark image
eff	Effusion
fg	Foreign gas
$mean$	averaged quantity
O_2	Oxygen
p	Particle
RMS	Root-Mean-Square
skn	Skewness
$swirler$	Swirler
Tu	Turbulent
x	x-direction
y	y-direction
z	z-direction

Acronyms

CCD	Couple Charged Device
CFD	Computational Fluid Dynamics
$CRVP$	Counter Rotating Vortex Pair
FoV	Field of View
$FPSP$	Fast responding Pressure Sensitive Paint
HTC	Heat Transfer Coefficient
HWA	Hot Wire Anemometry
IA	Interrogation Area
IRZ	Inner Recirculation Zone
ISL	Inner Shear Layer
JCF	Jet in Cross Flow
KH	Kelvin Helmholtz
LDA	Laser Doppler Anemometry
LDV	Laser Doppler Velocimetry
$MFRR$	Mass Flow Rates Ratio

ORZ	Outer Recirculation Zone
OSL	Outer Shear Layer
$OTMZ$	Omogeneous Turbulent Mixing Zone
POD	Proper Orthogonal Decomposition
PIV	Particle Image Velocimetry
PR	Peak Ratio
PSD	Power Spectral Density
PSP	Pressure Sensitive Paint
PVC	Precessing Vortex Core
$RANS$	Reynolds Averaged Navier-Stokes Equations
RMS	Root Mean Square
SCC	Standard Cross Correlation
SNR	Signal to Noise Ratio
TKE	Turbulent Kinetic Energy
TLC	Thermocromic Liquid Crystals
TLS	Turbulent Length Scale
TR	Time Resolved
$TRPIV$	Time Resolved Particle Image Velocimetry
UV	Ultra-Violet

Chapter 1

Problem Overview

Contents

The development of ever more modern gas turbines, characterized by high performance and reduced harmful chemical emissions, passes through some principal aspects:

- achievement of high temperatures and overall pressure ratio in the combustion chamber;
- flame stability promoted by swirler injectors;
- a very unbalanced flow split in favor of the main flow to promote lean flames.

All these aspects make the film cooling of the combustion chamber walls an increasingly hard task. Above all, due to ever lower cooling mass flow rates of the liner which interact with aggressive and highly turbulent swirling flows. This last aspect greatly reduces the wall film cooling capabilities due to the

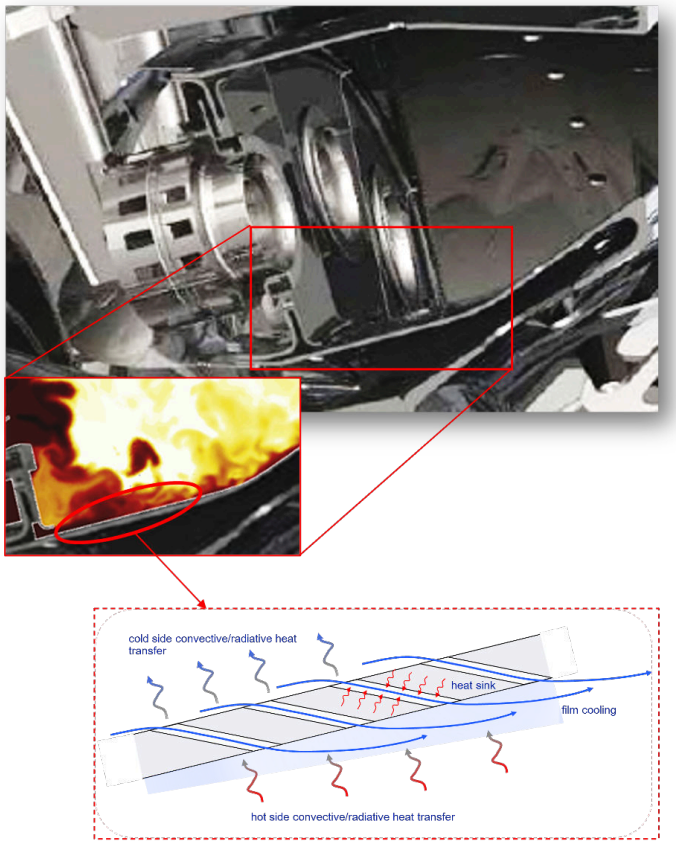

Figure 1.1: Operating principle of the liner effusion cooling technology.

strong increase in mixing between main and coolant flows. At the same time, the metal temperature must be maintained below acceptable values that, according to Lefebvre [1], for nickel-based alloys should not exceed 1300 K, with flame temperatures usually above 2000 K. In this context, the effusion cooling technology is the most established among the possibilities to generate a film cooling. It is widely used in modern combustors because it increases thermal effectiveness with low coolant consumption compared to other technologies. Effusion cooling consists of an array of closely spaced discrete film cooling holes distributed on the wall liner surface, as shown in Fig. 1.1. With respect to the classical film cooling configurations, effusion one is characterized by a greater number of holes with smaller diameters to both create a more defined cold layer between walls and hot gases and

the heat sink effect. Krewinkel [2] quite recently proposed an exhaustive review about effusion cooling technology for several applications. In this scenario, the development of increasingly advanced measurement techniques to characterize mixing between main and coolant flows is an essential research topic in the turbomachinery field. Therefore, it is important to develop Time-Resolved and High-Frequency experimental investigations, in addition to the consolidated steady-state analysis, for a complete characterization of the flow unsteadiness and turbulent mixing in the combustion chambers. In fact, in-depth knowledge of the unsteady interaction between swirling main and effusion coolant flows can provide essential information to design well-performing cooling systems.

1.1 Swirling Main Flow

For decades many works have focused on analyzing flow structures in average terms in the combustion chamber [3] and the dynamic of the vortex break down [4]. These studies served to identify the Sn = 0.6 minimum value for the generation of the swirling jet vortex break down with the formation of a toroidal recirculation zone called Inner Recirculation Zone IRZ useful for flame stabilization. As shown in Fig. 1.2, due to the confinement of the flow in the combustion chamber, it is possible to identify other recirculation zones located on the outer shear layer of the jet called the outer recirculation zones ORZ. The Swirl number (Sn) plays a fundamental role in the flow field configuration produced by a swirler. In fact, the size and shape of the mentioned recirculation zones are directly connected to the Sn value. Numerous numerical and experimental studies were conducted by varying the swirl number to estimate its impact on flame stabilization and flow field properties [5, 6, 7]. With an unsteady nature of time-coherent type, another structure is represented by the Precessing Vortex Core (PVC) located on the inner shear layer of the swirling jet.

Over the years, through the use of 1D measurement techniques, such as HWA and LDV, experimental characterizations of PVC behavior on the inner shear layer have been performed in the frequency domain [9, 10]. The

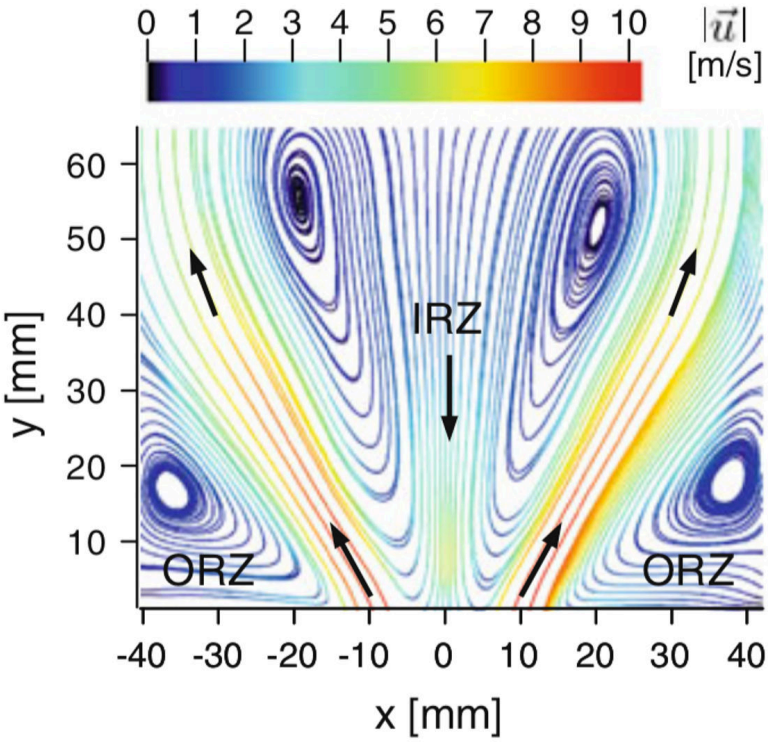

Figure 1.2: Average swirling flow field [8].

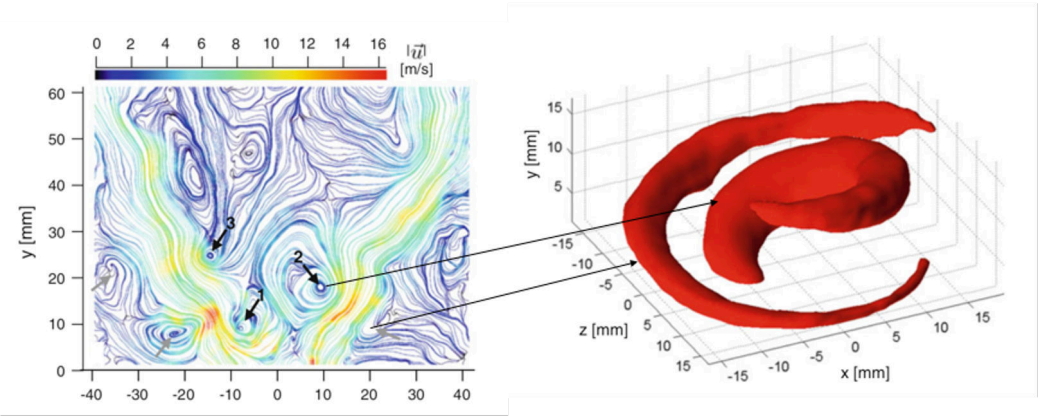

Figure 1.3: Shear layers unsteadiness [8].

development of ever more advanced measurement in the PIV sector made it possible to carry out analyzes (also in reactive condition) to acquire instan-

taneous snapshots of the flow field insight combustor simulators. This allows a study of the unsteady structures that develop in the swirling jet shear layers, such as the PVC on the ISL (Fig. 1.3). Furthermore, through numerical methods such as the Proper Orthogonal Decomposition (POD), it is possible to have both steady (IRZ, ORZ, Jet shear layer) and unsteady (PVC) characterization of the flow structures and information about the energy content of the unsteady structures[11, 12, 8]. In fact, the POD consists of splitting temporal from spatial information of the flow field analysis, allowing the distinction between deterministic and random fluctuations without an external trigger signal. More recently, the development of lasers and acquiring camera capable of working at high frequencies has made it possible to conduct the 2D PIV analyzes in Time-Resolved and High-frequency mode. This allows a complete and direct characterization of the unsteady flow structures. In this scenario, Ek et al. [13] and Providakis et al. [14] have carried out simultaneous high-speed PIV and flame measurements using high frequency experimental setups. Employing these measurements, the simultaneous fuel distribution, flame position, and flow velocity can be studied. Moreover, they used several average and statistics approaches to analyze the dynamical flow features of shear layers.

1.2 Effusion Cooling

1.2.1 Fluid dynamics of the effusion jets

Several fluid dynamics and geometrical parameters affect film cooling jet behavior and, consequently, the coolant layer promoted by an effusion cooling system. Several equations and correlations, starting from these parameters, were proposed in the literature to assess the performance of the cooling schemes. It is useful to start from Newton's law for convective heat flux, reviewed by Goldstein et al. [15]. The heat transfer to a cooled surface has been calculated using the equation:

$$q = HTC_{main} A(T_w - T_{ad}); \tag{1.1}$$

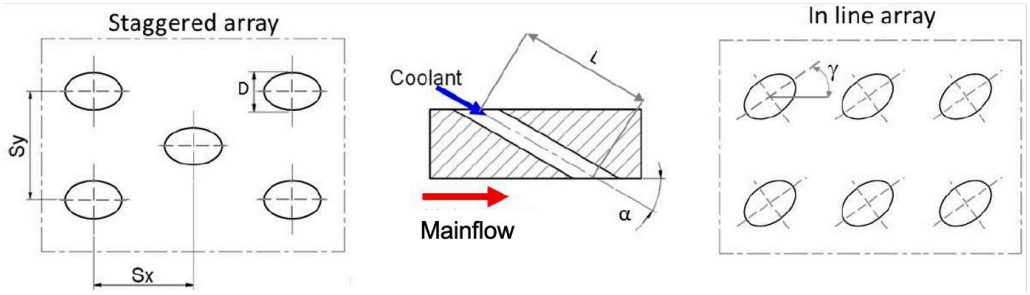

Figure 1.4: Main geometrical parameters for effusion cooling arrangements.

Where main refers to the hot gas side. The driving parameters which control the heat flux to the liner wall are the difference between the wall temperature T_{w} and the adiabatic wall temperature T_{ad}, the exchange surface A, and HTC main value. The T_{ad} parameter is defined as the temperature obtained locally on a perfectly insulated surface (i.e. adiabatic wall). The definition of heat load based on the adiabatic wall assumption leads to a definition of a heat transfer coefficient (HTC) independent of the temperature and only dependent on the flow field. Adiabatic wall temperature is always presented through a non-dimensional equation called adiabatic effectiveness law:

$$\eta_{ad} = \frac{T_{main} - T_{ad}}{T_{main} - T_{cool}}; \tag{1.2}$$

T_{main} represents the main flow total temperature and T_{cool} the coolant flow temperature injected from the cooling system. When the adiabatic effectiveness is equal to 1.0, it means that the film produces complete protection of the cooled surfaces. Moving to the flow and geometrical parameters (Fig. 1.4) that directly affect the HTC and the adiabatic effectiveness values, it is possible to define: the hole diameter (D) and length (L), stream-wise (S_x), and span-wise (S_y) pitch, hole injection (α) and compound (γ) angles, and perforation porosity. Regarding the flow parameters, a set of dimensionless numbers that govern the jets and the mainstream interaction can

be identified in the classical litterature: density ratio DR, velocity ratio VR, blowing ratio BR, and momentum flux ratio MR.

$$DR = \frac{\rho_c}{\rho_g} \tag{1.3a}$$

$$VR = \frac{V_c}{V_g} \tag{1.3b}$$

$$BR = \frac{(V\rho)_c}{(V\rho)_g} \tag{1.3c}$$

$$MR = \frac{(V^2\rho)_c}{(V^2\rho)_g} \tag{1.3d}$$

$$\tag{1.3e}$$

Often VR is used to distinguish the different coolant regimes in accord with the classification proposed by Han et al. [16]: $VR < 0.25$ addition mass flow rate regime, $0.25 < VR < 0.8$ mixing regime, $VR > 0.8$ penetration regime. The typical regime of the liner effusion systems is the penetration regime ($VR > 0.8$). This is characterized by a complex interaction between main and coolant and a strong turbulent diffusivity, which makes the prediction of adiabatic effectiveness values particularly complicated. Further difficulties are given by the aero-thermal flow field complexity inside the combustion chamber: ORZ, swirling jet impingement region, strong tangential velocity component, swirling flow unsteadiness, etc. For this reasons, general guidelines are difficult to be drawn: the potential range of VR can be about 1-15 while the DR is around 1.5-3.0. These parameters describe the boundary conditions in which the effusion cooling jets work. The jets complexity, especially in the penetration regime, has promoted numerous investigations over the years to characterize their aero-thermal flow field and adiabatic effectiveness for a wide range of boundary conditions. The goal is to better understand the mixing phenomena between the coolant and main flows, which is the main reasons of effectiveness reduction. The complex flow structures of the jets in cross-flow, in general, make this objective particularly difficult.

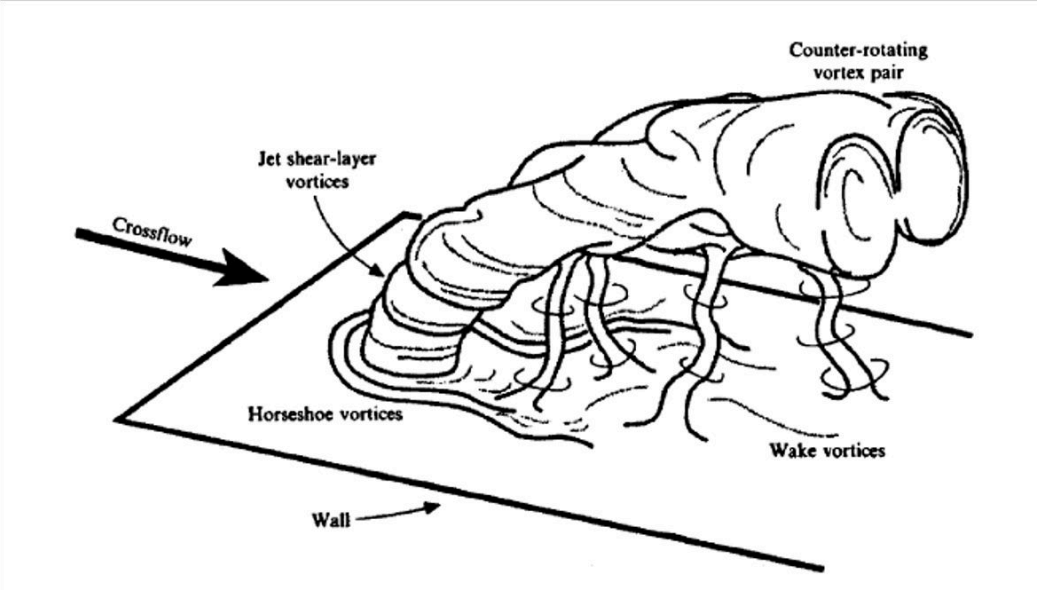

Figure 1.5: Jet in cross-flow [17].

In fact, as can be seen in the figure1.5, a cross-flow jet is characterized by a large number of secondary and unsteady flow structures [17]. Four different coherent structures are recognizable:

- The jet shear-layer vortices (Kelvin-Helmholtz instability. KH).
- The horseshoe vortices wrapping the jet base.
  - Due to hole upstream deceleration, which promotes a three-dimensional separation of the external boundary layer.
- The counter-rotating vortex pair (CRVP).
  - Their structure is promoted in the hole perforation; the jet bending, together with the strong shear stress on its external structure, strengthens the vortex pair.
  - They entrain surrounding fluid into the jet core, resulting in the typical kidney-shaped structure.
- The wake vortices.

– They are formed due to the vortex shedding in the hole downstream deceleration region.

1.2.2 Trend of the experimental investigations

Several works are available in the literature regarding the film cooling behavior; pioneering studies on this topic generally present time-averaged flow field and turbulence measurements with axial mainstream performed with different techniques. Thole et al. [18] and Scrittore et al. [19], using the laser Doppler velocimetry (LDV) and PIV technique, provided a large amount of data in terms of velocity contour and profile, turbulence and shear stress values by varying the classic fluid dynamic parameters and the holes shape (cylindrical and expanded exit holes). The same authors, more recently, have also carried out PIV measurements in the plane normal to the axial flow direction analyzing the contribution of the CRVP in terms of RMS and shear stress, and evaluating their impact on the wall temperature and adiabatic effectiveness values [20]. In order to estimate the effect of highly turbulent main flows, such as in the combustion chamber, Kadotani and Goldstein [21][22] and Kohli and Bogard [23] focused their activities on the measurement of adiabatic film cooling effectiveness (IR camera) and 1D velocity measurements (high-frequency velocity probe) of the flow field of cylindrical cooling holes by varying the turbulence intensities of the main flow from Tu = 0.5% up to Tu = 20%. Saumweber et al. [24] [25] compared adiabatic effectiveness values promoted by cylindrical and shaped holes at various turbulence intensities between Tu = 2% and 11% by means of IR camera test campaigns.

More recently, several authors, with the aim of having a complete characterization of the unsteady structures of the film cooling jets, presented experimental results using the Time-Resolved PIV technique since it gives the opportunities to analyze vorticity evolution and the unsteady aero-thermal fields. Eberly and Thole [26] used Time-Resolved PIV to study a single row of holes with an axial mainstream, varying the main fluid dynamic parameters that affect the behavior of the jets (i.e. blowing ratio BR, momentum ratio MR, and velocity ratio VR) and showing results in terms of turbu-

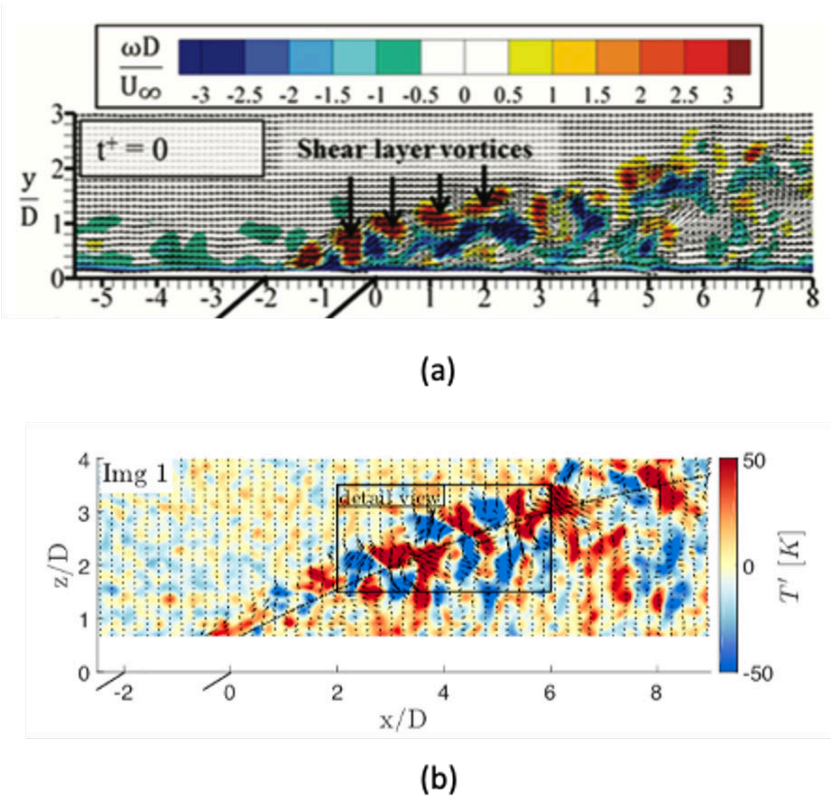

Figure 1.6: (a) Instantaneous KH vorticity values [26] for a JCF. (b) instantaneous temperature and velocity field for a JCF: KH contribute to the turbulent mixing [27].

lence and vorticity. This work highlights the behavior of the shear layer vortices (Kelvin-Helmholtz instabilities): size, spacing, and turbulence decay (Fig. 1.6(a)). Innovative techniques, such as the thermographic Particle Image Velocimetry, which also provides temperature information, have been exploited by Abram et al. [32] and Straubald et al. [27] to provide additional contributions to the topic. This measurement was applied in a closed-loop wind tunnel equipped with angled and trenched film cooling holes plates using BAM:Eu2+ thermographic phosphor technique. A pulsed high-speed UV laser was used for a two-colors radiometric approach measuring the temperature and, at the same time, the velocity flow field with an acquisition frequency of about 6kHz. This setup allowed to perform time resolved and spectral type measurements of the coolant jets to detect coherent time struc-

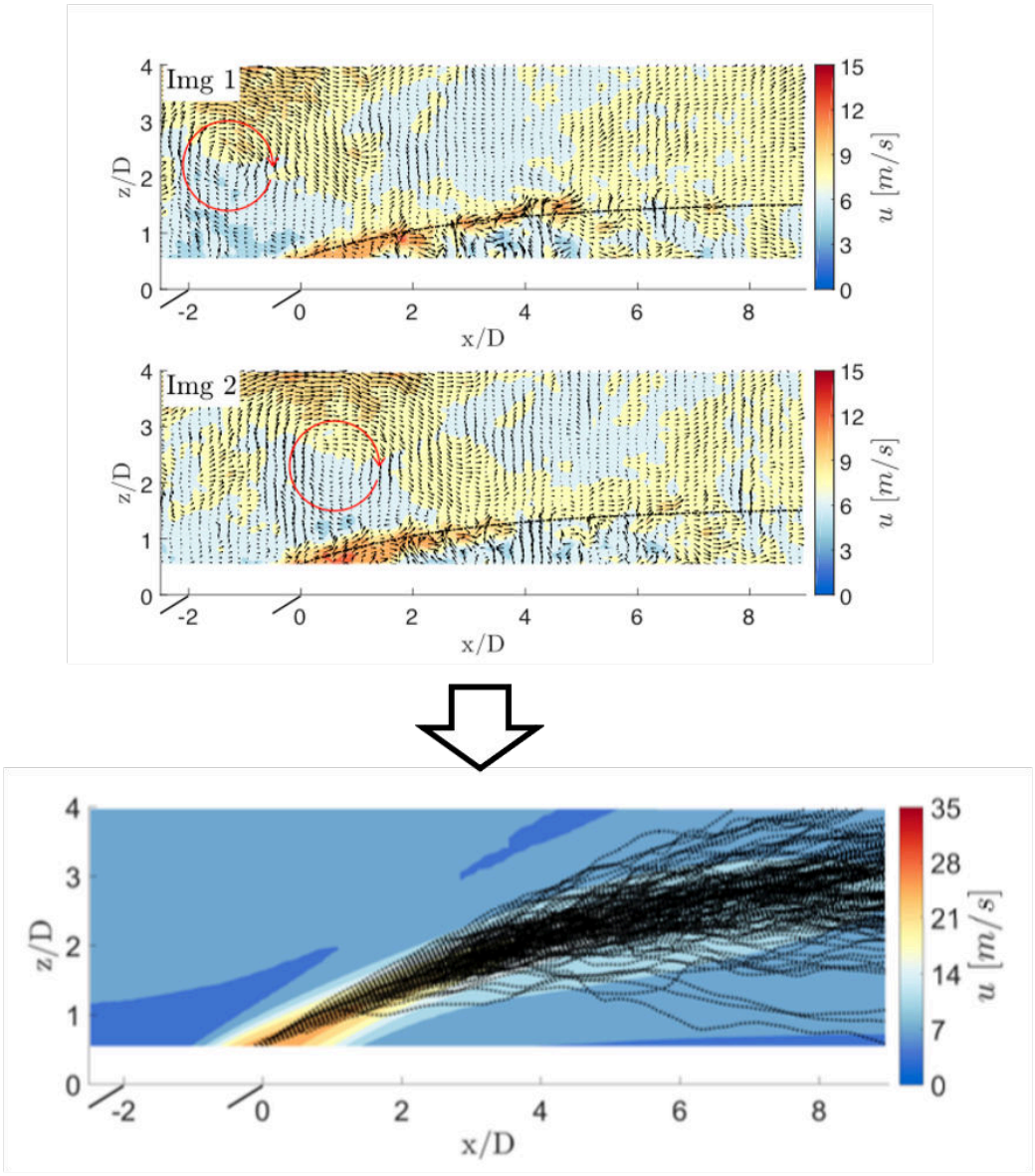

Figure 1.7: Jet oscillatory behavior promoted by the turbulent main flow [28].

tures such as shear layer and wake vortices. As illustrated in Fig. 1.6(b), these measurements showed that, due to the Kelvin-Helmholtz unsteadiness of the jets, hot air breaks through the cooling film and almost reaches the wall surface, revealing that the instantaneous gas temperature close to the wall can be significantly higher than what is expected from the average tem-

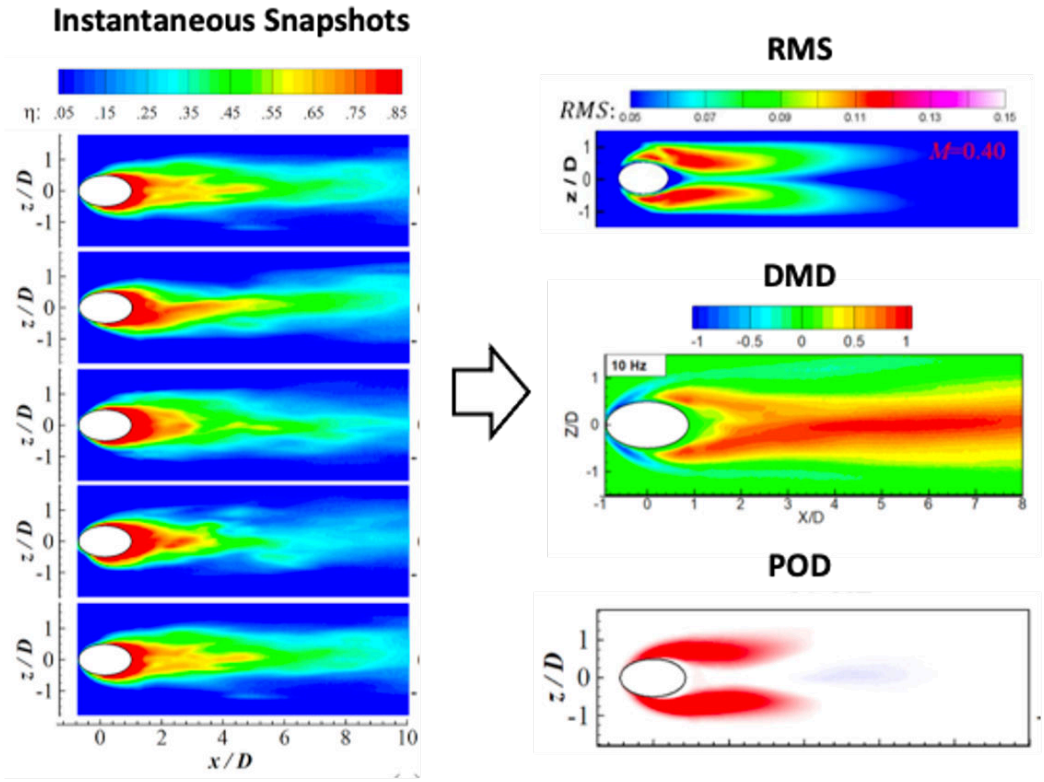

Figure 1.8: High-frequency adiabatic effectiveness measurements: FPSP technique [29, 30, 31].

perature field. Strau wald et al. [28] carried out high-speed PIV to visualize and analyze the interaction of turbulent main flow and cooling air, detecting another unsteady behavior of the JCF: the oscillatory phenomena of the film cooling jets that occurs when they interact with the high turbulent main flow as shown in Fig. 1.7. The tests have been carried out with main flow turbulence intensities of Tu = 18.5% and Tu = 21.5%. The authors have shown that low-momentum jets are strongly affected by small and large turbulent structures. Main flow eddies either lift off the jet from the wall or pushes the jet towards the surface. High-momentum jets are more stable but still affected by the larger main flow eddies. Works with unsteady adiabatic effectiveness measurements have also been presented very recently, parallel to the aero-thermal unsteady type just described. For the first time, Zhou et al.

[29],[30, 31] presented unsteady adiabatic effectiveness measurements for film cooling holes with different geometries and in the presence of periodic fluctuation of the main flow. The high-frequency measurements were performed using Fast-response pressure sensitive paint (FPSP) and a high-speed camera with an acquisition frequency of 6 kHz. The instantaneous snapshots were post-processed by statistical (Root Mean Square) approaches and POD and DMD analyzes for statistic and dynamic information of the effectiveness distribution respectively. The unsteady contribution to the turbulent mixing of the CRVP, horseshoe vortex, and near-hole structures were identified clearly from the large dataset through POD and DMD analysis of the effectiveness fluctuations, as shown in Fig. 1.8.

1.3 Effusion Cooling and Swirling Flow Interaction

As shown in the previous section, the scientific works on effusion cooling systems analyze the aero-thermal behavior of the jets in presence of relatively simple conditions: experimental configurations are based on plates with a single row of holes and axial main flow. Very few works present test rigs dedicated to a characterization of the effusion systems in the presence of swirling main flow, simulating realistic conditions that can be observed in a real combustion chamber.

Pioneering research activity in this field was done by Wurm et al. [33]. They developed a warm planar tri-sector rig equipped with an LDI injector [34] for steady-state analysis of the interaction between main and cooling flows. The rig allowed laser optical diagnostics like PIV and 3D component LDA for the main flow field analysis. The thermal measurements for the adiabatic effectiveness characterization of the cooling system are based on highly resolved temperature mappings of the cooled surface by means of infrared thermography. As shown in Fig. 1.9, this work provides average term information about the influence of the swirling main flow on the coolant sub layer

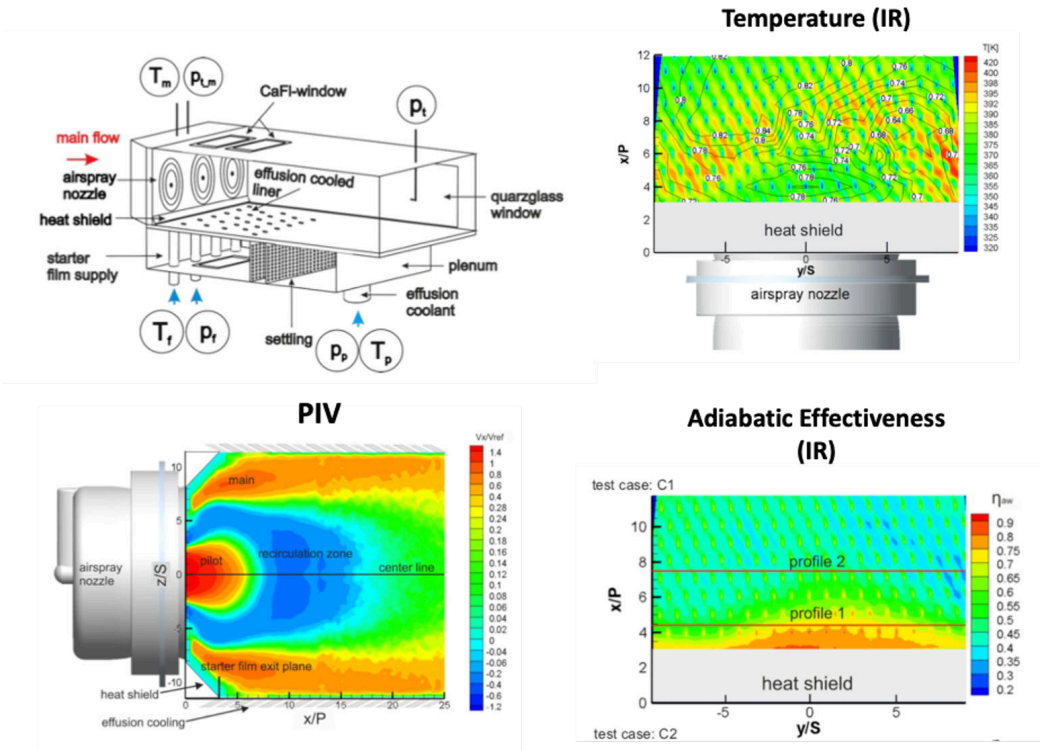

Figure 1.9: A sketch of the experimental investigation carried out by Wurm et al. [33, 34].

development. The remarkable influence of the swirling flow on the cooling effectiveness was detected, especially near the identified swirler jet impinging region and the outer recirculation zones. The results indicate that better adiabatic effectiveness can be achieved by increasing the pressure drop across the multi-perforated plate from 1% to 3%; in fact, with low pressure drop values, the cooling penetration is significantly blocked by the main flow. Andreini et al. [35, 36, 37] provided another important contribution to this type of steady-state analysis with a similar experimental set up. The rig is a linear tri-sector cold rig with the possibility to warm the effusion plate to conduct heat transfer analyses. It is equipped with lean low NOx combustor swirlers. A summary of the measurements performed with this experimental setup is illustrated in Fig. 1.10. The flow fields measurements were carried out by means of PIV, highlighting a strong mutual interaction between swirling and

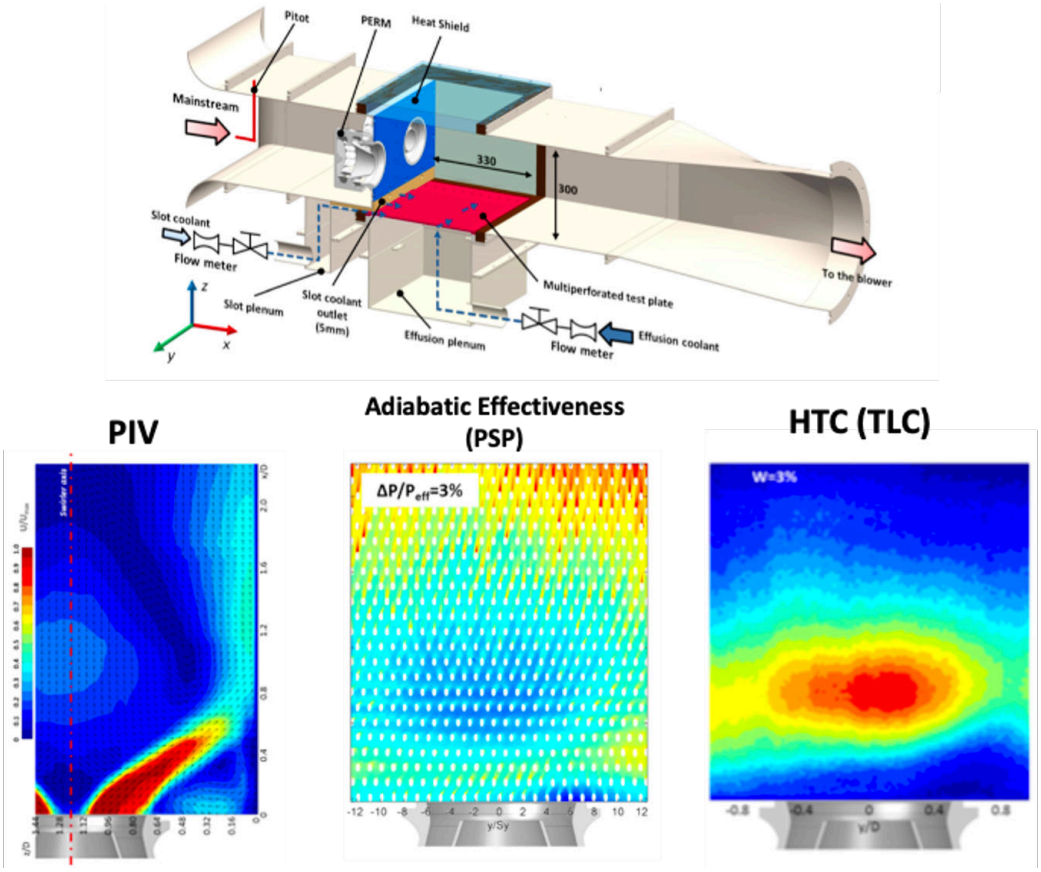

Figure 1.10: A sketch of the experimental investigation carried out by Andreini et al. [35, 36, 37].

effusion cooling flows. Adiabatic effectiveness measurements were performed through the PSP technique and, in agreement with Wurm et al. [33] results, a strong interaction between main and coolant flows, mainly in the impingement region, is shown. Combining the results of the adiabatic effectiveness with the heat transfer ones performed by Thermochromic Liquid Crystal technique, NHFR values were provided, highlighting that the reduction of heat flux is obtained by lowering the feeding pressure drop of the effusion system.

Other important contributions, with reactive test rigs, have been provided by Ji et al. [38] and Greifenstein et al. [39]. Ji et al. [38] developed

a three-sector annular combustor test rig to conduct an experimental investigation on the liner effusion cooling performance using a steady-state infrared radiation thermography method at reacting flow conditions. Instead, Greifenstein et al. [39] carried out a very in-depth characterization of the film cooling behavior in a reactive test rig in the presence of swirling main flows. Their work presents a flame-cooling investigation, thanks to a single sector effusion-cooled reactive test rig, through wall temperature (2D thermographic phosphor thermometry), gas-phase temperature (coherent anti-Stokes Raman spectroscopy), flame structures (planar laser-induced fluorescence of OH), and flow field (particle image velocimetry) measurements. The rig works in almost real boundary conditions with elevated temperature and pressure [40]. The main parameter, such as swirl number, fuel staging, and effusion cooling mass flow rate, were varied to investigate their effect on total film cooling effectiveness. The implemented measurement set-up provides a steady-state and acquiring instantaneous snapshots useful for a statistical analysis. As shown in the graphical abstract of Fig. 1.11 the results highlight local rupture of the coolant sub-layer, interaction of the swirling flow with the effusion jets, strong liner surface temperature gradients, and a marked difference in statistical behavior of temperature and total effectiveness values on the liner surface by varying the Sn and the fuel staging.

1.4 Thesis Motivation and Structure

As shown in this chapter, the requirements for improving the gas turbine combustors make the design of even more efficient cooling systems and the correct estimation of liners heat load a hard task. Due to the complex flow field produced by the swirler injectors and the effusion cooling systems, their interaction is difficult to predict. Consequently, the adiabatic effectiveness distributions on the liner surface cannot be estimated with accuracy using classical simplified correlations. For this reason, understanding the effects of the swirling flow on the near-wall coolant sub-layer is fundamental to support the development of better effective cooling schemes and improve combustors durability. Section 1.3 explains that there are few works in literature deal-

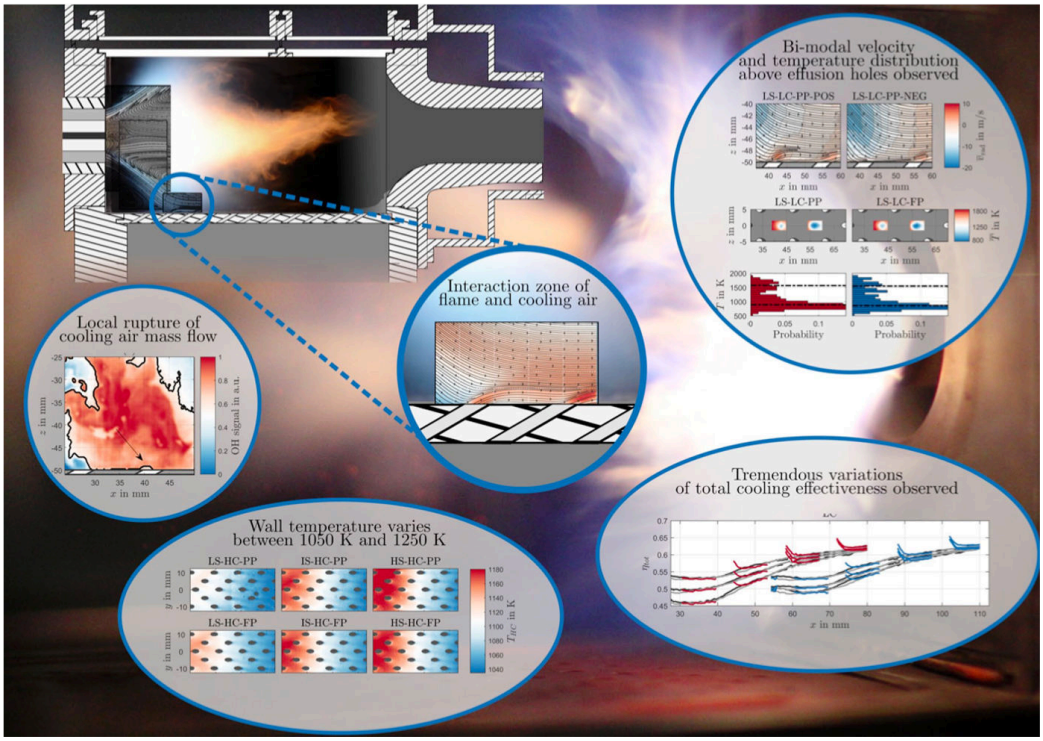

Figure 1.11: A graphical abstract of the experimental investigation carried out by Greifenstein et al. [39].

ing with these topics. Furthermore, these works are of the steady-state type but the fluid dynamic mechanisms, which govern turbulent mixing between main and coolant, are the instabilities of the flow field. For these reasons, the present work aims at deepening the knowledge of the unsteady interaction between swirling main and effusion cooling flows from an experimental point of view. In order to achieve this goal, unsteady measurements of the flow field (TRPIV) and adiabatic effectiveness (FPSP) were carried out in a test rig. Previous literature surveys report that several parameters affect the effusion cooling behavior; two of these were chosen to conduct the experimental campaigns: the main flow Sn and cooling jets VR (effusion plate pressure drop).

The work of this Ph.D. course was thus structured:

- **Test rig design**. A linear, non-reactive, and isothermal (ambient

temperature) single sector test rig has been designed. Therefore, three swirler injectors characterized by different swirl numbers (1.0, 0.8, and 0.6) were designed and printed in PA. During the design phase, to obtain the desired Sn, numerical simulations (RANS, k-epsilon turbulence model) were carried out.

- **Experimental setup development.** Experimental setups have been developed in the THT Lab of the University of Florence for the velocity field and adiabatic effectiveness measurements.
  - Time-Resolved Particle Image Velocimetry: Optical trails were designed to make laser sheet on the analyzed planes. Measurements were made to estimate uncertainty with different optical and test conditions setups.
  - Fast Response Pressure Sensitive Paint: The paints have been calibrated and characterized. Measurements were made to estimate uncertainty as the measurement conditions vary. A linearity check of the camera sensor at low counts was made to avoid systematic errors.
- **Tests and post-process.** By varying the operating conditions (Sn of the injectors and feeding pressure drop of the liner), TR-PIV, and adiabatic effectiveness measurements were performed. The collected data were post-processed as follow:
  - Velocity flow field: mean values, Time-Resolved snapshots, turbulence levels, spectral analysis of kinetic energy, integral length scale analysis, tracking of the oscillatory behavior of the cooling jets, and vorticity analysis.
  - Adiabatic effectiveness: mean values, Time-Resolved snapshots, statistical processing with descriptive statistics parameters to evaluate the unsteady behavior of the jets trace on the liner.

The resulting goal is to highlight that an unsteady type analysis is strictly necessary to provide a complete characterization of the behavior of the cold

sub-layer and its turbulent mixing with the main flow, which directly affects the cooling capability of the film cooling systems and the liners lifetime.

The results also represent one of the research contributions of the University of Florence within the SOPRANO (SOot Processes and Radiation in Aeronautical inNOvative combustors) European project [1]. The SOPRANO initiative aims to provide new elements of knowledge, analysis and improved design tools, opening the way to alternative designs of combustion systems for future aircrafts capable of simultaneously reducing gaseous pollutants and particles, and improve the liner lifetime. Specifically, the work of this thesis is placed in the Work Package 3 of the project: increase the reliability of cooling design for durable combustors through the improvement of the accuracy in the prediction of the metal temperature of combustor liners by using new experimental measurement on realistic test cases.

[1] https://www.soprano-h2020.eu/

Chapter 2

Single Sector Rig

Contents

2.1 Experimental Apparatus

Test Rig

According to what was described in the previous chapter and to the goal of this Ph.D. work, a test rig has been designed to assess the impact of the Sn parameter on the near-wall effusion behavior. The test rig, shown in Fig. 2.1 and operated in the open loop wind tunnel of the THT LAB at the University of Florence, consists of a non-reactive single sector planar rig working at ambient temperature; it allows the control of two separated flows: the swirling main-flow, which enters into the test section across a swirler, and the cooling flow, to feed an effusion plate. The test chamber has an aspect ratio (H/L_z) equal to 1 (square section) with a side H length of 395mm ($2D_{ext}$ swirler). The length in the y direction of the test section is equal to 5H. On the bottom wall of the test section a multi-perforated plate, with cylindrical holes was

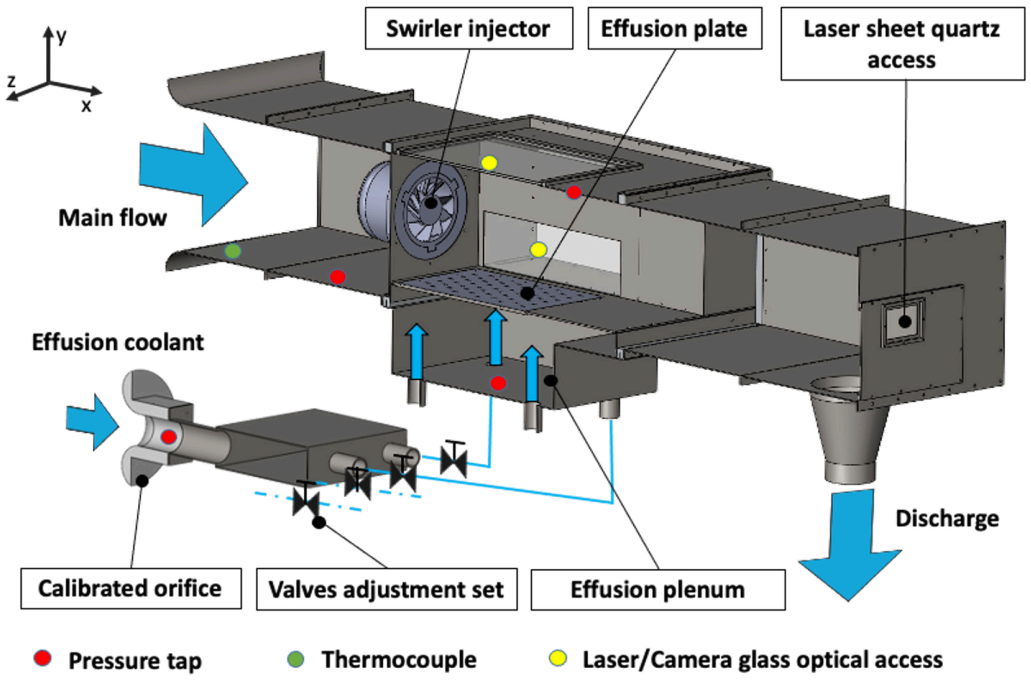

Figure 2.1: Sketch of the test rig.

installed and fed by a plenum chamber, to simulate an effusion cooled liner. A $90kW$ centrifugal blower, with a maximum flow rate capability of about 8400 m^3/h, is connected to the discharge duct of the rig. Compared to typical engine dimensions, the rig was scaled up, around 9:1, in order to increase the spatial resolution of the measurements. Moreover, a scaled up geometry helps in reducing the characteristic frequency of the unsteady phenomena. Calibrated orifices were used to measure main and coolant mass flow rates. One of them, as sketched in Fig. 2.1, is positioned upstream of the coolant valves, to directly measure the coolant mass flow, while the second is located downstream of the discharge of the test rig, allowing to measure the sum of mainstream and coolant mass flow rates. In order to vary the test rig operating conditions, the coolant plenum is preceded by a regulation system composed with four 2" valves as shown in Fig. 2.1; this feeding system allow a precise regulation of the pressure drop through the effusion plates. The dimensions of the cooling system supply plenum guarantee almost static con-

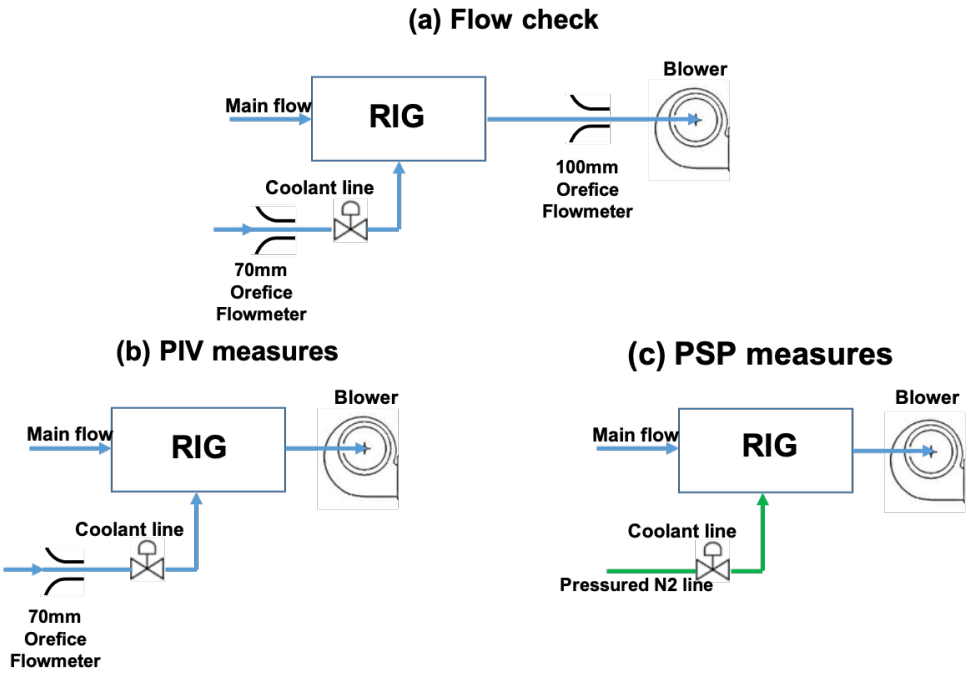

Figure 2.2: Sketch of the test rig.

ditions of plate feeding flow. The pressure inside the test section is instead controlled by adjusting the RPM of the blower. The rig is equipped with 3 optical (glass and quartz) accesses for the light sources and the camera to conduct the PIV and PSP measurements on the three different spatial planes.

Fig. 2.2 shows how the test rig is installed in the laboratory facility during the tests carried out. Fig. 2.2 (a) shows the configuration for the swirlers and effusion plate flow check. The use of two calibrated orifices allows to separate the contributions of the main flow and the coolant mass flow rate. The discharge coefficient (C_d) and consequently the effective area (A_{eff}) of the injectors and effusion plate were estimated using this setup configuration during separate tests performing a flow check by varying the feeding pressure drop. The effective area A_{eff} is defined as: $A_{eff} = A_{geom} \cdot C_d$; were A_{geom} is the cross section geometric area respectively of the injector and effusion plate. The second set up (Fig. 2.2 (b)) was used for PIV measurements; Fig. 2.2 (c)

instead shows the facility used for the adiabatic effectiveness measurements. In this case the coolant plenum is fed by a tracer gases (N2) from a pressured line. Static pressure taps and thermocouples were installed in the test rig as shown in Fig. 2.1 to control the principal fluid dynamic parameter during the tests. The control of the mass flow rate of the injector and effusion plate during the PIV and PSP tests is guaranteed measuring the pressure drop and the air temperature thanks to the flow checks previously made for both the components. A custom-tailored *Labview*-based application, in-house developeded, provided accurate monitoring and recording of the conventional data from measurement data scanners. A pressure scanner *NetScannerTM System 9116* with temperature compensated piezo-resistive relative pressure sensors is employed to measure static pressure in different locations inside the rig, highlighted in yellow in Fig. 2.1. The maximum uncertainty is ±52 Pa with a level of confidence of 95%. A *HP/Agilent* 34972*A* data acquisition/switch unit is used to monitor the flow temperature measured by means of T-type thermocouple (±0.5 K uncertainty, 95% level of confidence) in the main flow intake tunnel. Mass flow rates were measured by means the two calibrated orifices (70 and 100mm); they are affected by an error of 2-3% according to the standard ANSI/ASME PTC 19.1 [41] based on the Kline and McClintock method [42].

Effusion Plate

The effusion plate has 55 holes in staggered configuration which form 10 cooling rows. As shown in Fig. 2.3, the holes have an inclination of 20°. Reduced inclinations of this type, which guarantee good film effectiveness, are in fact to be considered an industrial reference target in the design of new combustors. The leading edge of the first horizontal row of holes was placed at a distance of 0.5 swirler external diameters (D_{extSW}) from the dome wall and from the swirler, where the x=0 value is located. The pitch in the x direction (2 Sx) is equal to 97.20mm and in the y one (Sz) to 48.6mm. All the geometrical information concerning the multi-perforated plate are summarized in the table at the bottom part of Fig. 2.3.

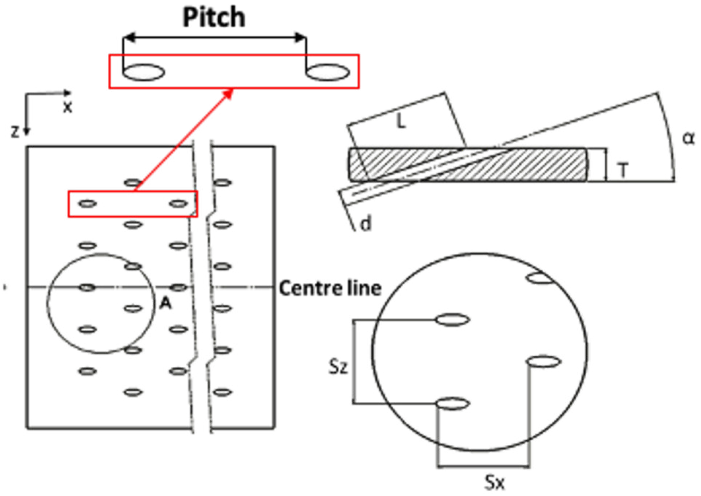

d [mm]	α [deg]	L/d [-]	T/d [-]	Sx/d [-]	Sz/d [-]	Porosity
6.08	20	6	2.1	8	8	5%

Figure 2.3: Principal features of the effusion plates.

Swirler Injectors

Three axial swirlers have been specifically designed and 3D-printed (PA) to assess the impact of the Sn parameter on the near-wall effusion behavior; a sectional view and other geometry information of this swirlers are reported in Fig. 2.4. They were designed by a preliminary CFD phase (RANS, k-ϵ turbulence model) starting from the correlation in Eq. 2.1 to define the right vane angle.

$$Sn = \frac{2}{3}\frac{1-(D_{int}/D_{ext})^3}{1-(D_{int}/D_{ext})^2}tan(\theta); \tag{2.1}$$

$$Sn = \frac{G_\Phi}{G_x r}; \tag{2.2}$$

Where D_{int} and D_{ext} are the internal and external diameters of the swirler and θ the vane angle. Eq. 2.2, where G_Φ is the angular and G_x the axial

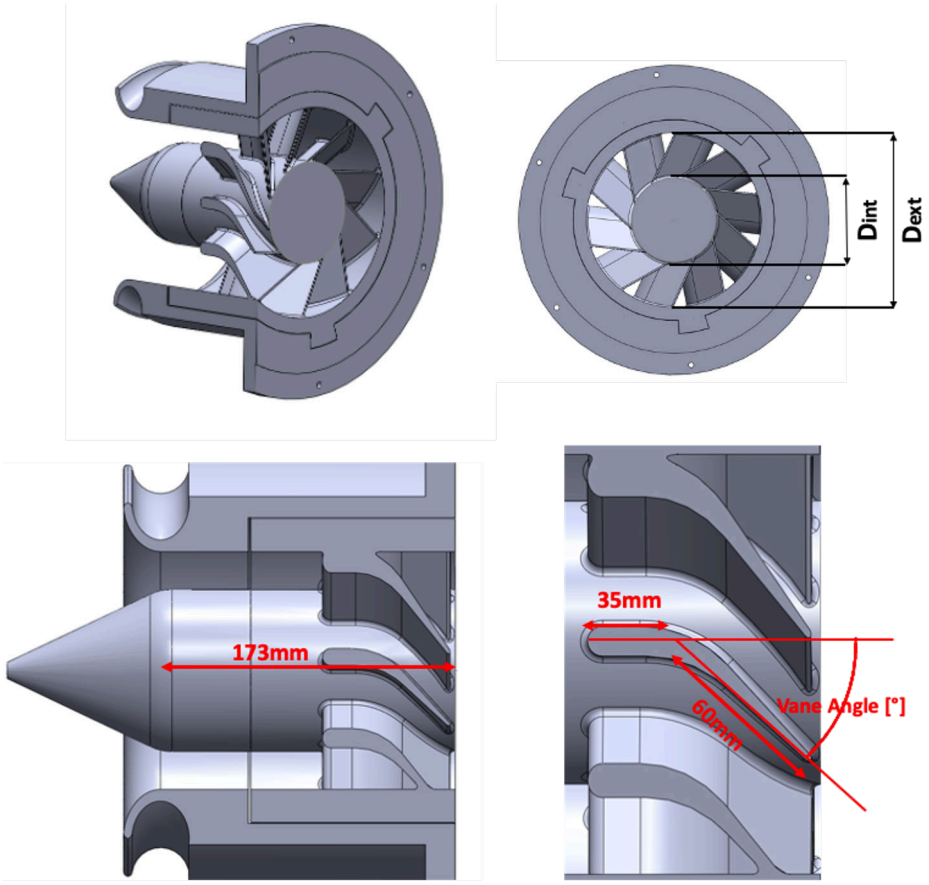

Figure 2.4: Sketch of the principal features of the injectors.

momentum, was used to measure the Sn with the results of the CFD analysis. r refers to the mean radius of the vanes annulus, defined as: $r = r_{int} + (r_{ext} - r_{int})/2$. The target Sn parameters (0.6 - 0.8 - 1.0) were satisfied in the design phase, by varying the vane angle, as shown in the Fig. 2.5. The number of vanes is equal to 10 and the internal body has a D_{int} of 95 mm, while the external diameter (D_{ext}) is 197.5 mm. As shown in Fig. 2.4, the swirler tube is 173 mm long and is equipped with an aerodynamic intake at the entrance to reduce pressure losses. The profile of the vanes has a first axial part of 35 mm while the inclined part is 60mm long. To generate the three levels of Sn, a different inclination of the vane was adopted from 35° to 52.5°. As a result the effective area is higher at low Sn (i.e. reducing the vanes

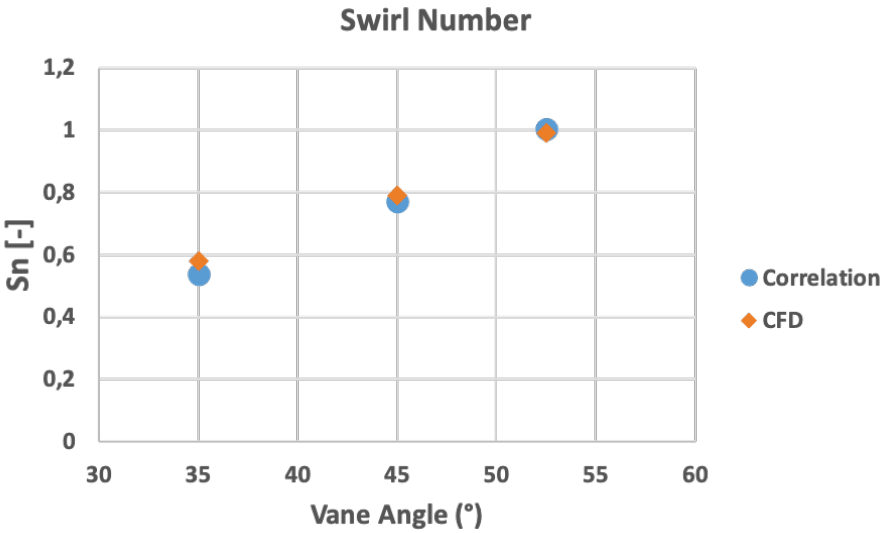

Figure 2.5: Design (Eq. 2.1) and CFD (Eq. 2.2) Sn evaluation camparison.

inclination angle) as remarked in Fig. 2.6. The graph also shows that the results of the experimental and numerical effective area measurements are in good agreement. This allows to have confidence on the CFD Sn estimate.

2.2 Test Conditions

In order to ensure comparability with the engine conditions, a dimensional analyses aimed at identifying the relevant dimensionless quantities were performed in the first design phase of the rig. Performing velocity and adiabatic effectiveness measurements, the relevant parameters considered during the preliminary design phase of the test rig were:

$$R_e = \frac{uL}{\nu} \tag{2.3}$$

$$\Delta P/P = \frac{P_{upstream} - P_{downstream}}{P_{upstream}} \tag{2.4}$$

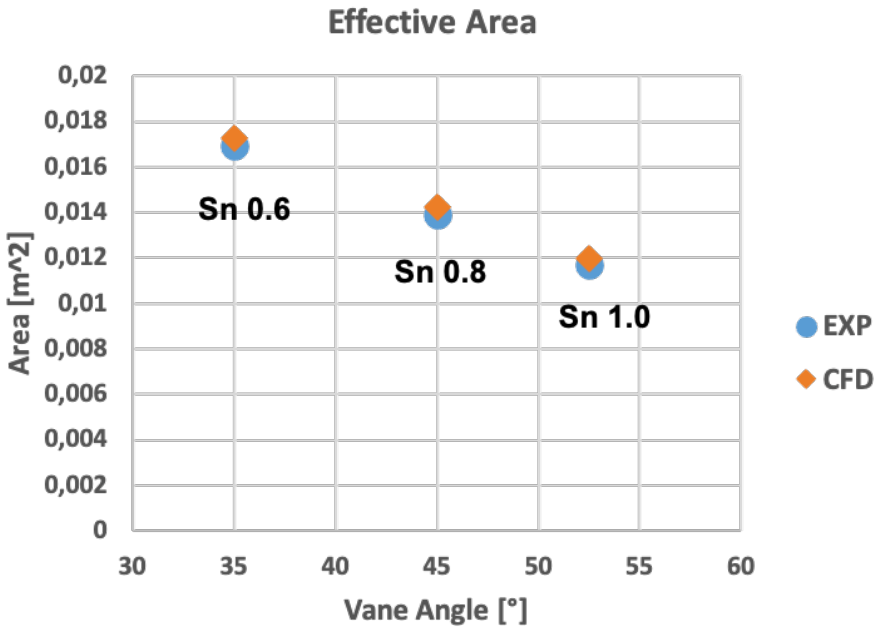

Figure 2.6: Experimental and CFD comparison of the measured effective area.

$$DR = \frac{\rho_{cool}}{\rho_{main}} \tag{2.5}$$

where the Reynolds number (Re) is evaluated using L equal to D_{extSW} and D_{hole}. $\Delta P/P$ represents the non dimensional pressure drop across the injectors and the effusion plate evaluated using the static pressure taps equipped in the test rig. The pressure drop can be considered to be the most important parameter to replicate the flow field inside a combustion chamber. For this reason, only this parameter has been matched during the test phase, neglecting the Reynolds number similitude. In fact, working at atmospheric conditions and considering the scaled dimension of the test rig it was impossible to have a Reynolds number similitude. Anyway the 9:1 scale of the test section guarantees a fully turbulent regime of the flow inside the rig with a Reynolds number of the main jet $\approx 9.6 \cdot 10^5$. Such scale factor represents the maximum value that can be selected considering the blower capability of the

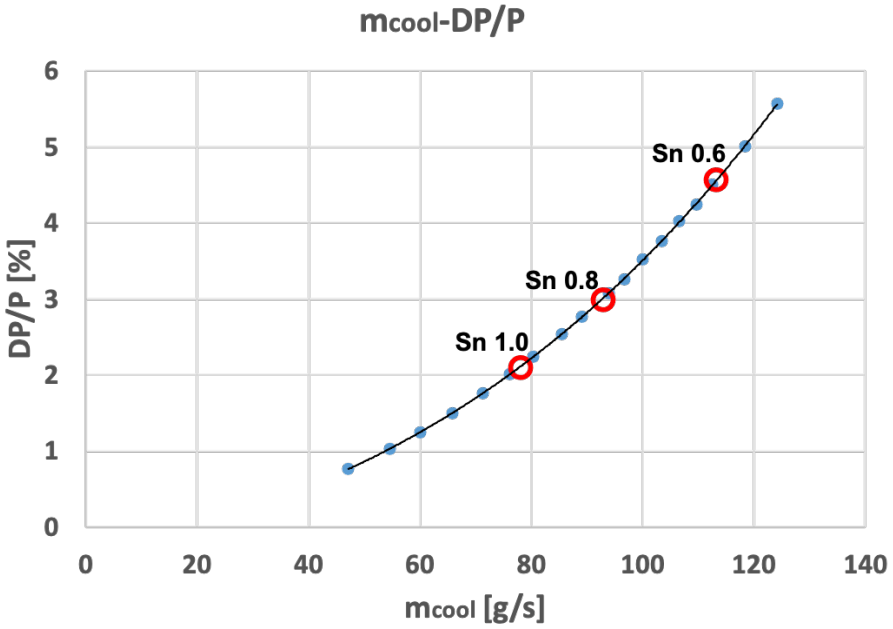

Figure 2.7: Flow check of the effusion plate.

facility. The pressure drop was also used as scale parameter for the coolant flow considering that in atmospheric conditions is impossible to match the DR with the real engine conditions. For this reason the DR was guaranteed equal to 1 for both PIV and PSP measurements, in fact nitrogen has been used at ambient temperature (DR=1) to feed the cooling line during the PSP tests (Fig. 2.2 (c)).

During the tests a constant pressure drop equal to 3% across the injectors was setted. This creates different main mass flow rate due to the different effective areas of the swirlers (Fig. 2.6). The case Sn=0.8 with Δ P/P_{main} = 3% and Δ P/P_{cool} = 3% has been chosen as reference case. By varying the Sn the effusion system pressure drop was regulated to match the mass flow rate ratio (MFRR) between main and coolant (m_{cool}/ m_{main}) with respect the reference case using the flow check curve in Fig. 2.7. A resume of the test conditions matching the mass flow rate is shown in Table 2.1 (Test Conditions A). Measurements were also carried out imposing Δ P/P_{eff} = 3%, without matching the m_{cool} / m_{main}, for all the Sn case as summarized in Table 2.2

Sn	1	0.8	0.6
$\Delta P/P_{main}$	3%	3%	3%
$\Delta P/P_{cool}$	2.14%	3%	4.61%
m_{cool}/m_{main}	0.077	0.077	0.077

Table 2.1: Test conditions A: matching m_{cool}/ m_{main} with respect the reference Sn0.8 case

Sn	1	0.8	0.6
$\Delta P/P_{main}$	3%	3%	3%
$\Delta P/P_{cool}$	3%	3%	3%
m_{cool}/m_{main}	0.064	0.077	0.092

Table 2.2: Test conditions B: imposing Δ $P/P_{cool} = 3\%$

(Test Conditions B).

Chapter 3

Experimental Techniques

Contents

3.1 Flow Field Measurement: Time-Resolved PIV

Particle Image Velocimetry (PIV) is a non-intrusive technique to instantaneously measure the flow velocity in an extended region. As shown in Fig. 3.1 it is based on the addition of seeding particles in a flow tracing their movement over time to calculate the velocity of the flow field. These particles are usually illuminated by a laser sheet in a flow plane, at least twice in a time interval. The light scattered by the particles is caught by a CCD (Charge-Coupled Device) camera. The recorded images are divided into smaller Interrogation Area (IA), assuming that the particles inside one IA are moving homogeneously, and their displacement vector between the two consecutive images is evaluated by statistical methods as auto and cross-correlation. Finally, the velocity vectors field is calculated by dividing the displacement vectors (transformed from pixel to physical length through a previous spatial calibration) by the time delay between the two consecutive laser impulses. Therefore through a PIV analysis, it is possible to obtain instantaneous images of the flow field useful for calculating a mean flow field and carrying out a statistical analysis to estimate turbulence values. For decades the limits imposed by lasers (frequency limit) and the acquisition camera (spatial resolution and frequency limits) have not allowed detailed analyzes of unsteady flows: limits on the length scale analysis of the vortices (spatial resolution limit) and impossibility to acquire time-related images (frequency limit). From this point of view, Westerweel [43] and Adrian [44] describe the measurement principle related to its limitations, whereas more recently, Adrian [45] did a review about the development of the method in the last two decades. Recently, with the introduction of high speed and high repetition rate lasers, the PIV measurements frame rate has increased strongly, opening the scenario of the Time-Resolved Particle Image Velocimetry (TR-PIV). With current instrumentation, turbulent flows, with moderate Reynolds number, can be completely characterized up to the Kolmogorov scales. Henning and Ehrenfried [46] gave a characterization of the temporal frequency response of a high repetition rate PIV system paying attention to

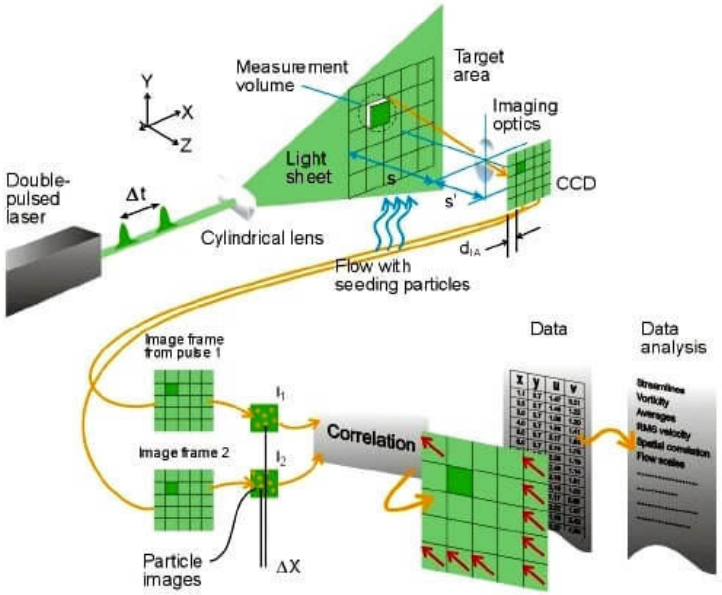

Figure 3.1: Experimental setup for 2D-PIV measurements

the influence of the IA size. Others [47, 48, 49] have proposed de-noising methods for the high-frequency PIV measurements for better spectral analysis. Therefore, these latest developments and related data-reduction have increased the level of unsteady high frequency analysis in the various fields of fluid dynamics, including turbo gas diagnostic applications. Regarding the turbo gas applications, inherent to the fluid dynamics of combustors (swirling flow and jets in cross flow), works carried out by TR-PIV measurements technique have already been presented in chapter1.

To carry out the flow field measurements, a 2D Time-Resolved PIV measurement setup was implemented. Considering the vastness of the topic, in this section only the PIV notions functional to the experimental setup characterization will be provided.

Measurement Theory

The seeding particles are constituted by inert substance and must have a small diameter in order to follow the streamlines of the flow field. A dimensionless number able to describe the capability of particles to follow the mean flow field is the Stokes number:

$$St = \frac{\tau U}{d_p} \tag{3.1}$$

$$\tau = d_p^2 \frac{\rho_p}{18\mu} \tag{3.2}$$

where τ is a characteristic response time of particle drag phenomena, U is the flow velocity, and d_p is the particle diameter. Eq. 3.2 is valid when the seeding density is much greater than the fluid density. To follow the streamlines, the particles must have a value of St number as low as possible. The particle response time consequently generates a velocity lag of the particle with respect to the real velocity of a fluid in constant acceleration. This generates a response trend of the particle velocity (Up) function of the time (t), which is described by the exponential equation 3.3 where U is the real velocity of the fluid.

$$Up(t) = U(1 - \exp(-\frac{t}{\tau})) \tag{3.3}$$

This exponential decay formulation is valid assuming constant acceleration, a great density differences between the seeding particles and the fluid, and taking into account the Stoke's law hypothesis (laminar behavior of the spherical particle in the flow, Re < 1). In different cases, like for the turbomachinery applications, the solution would be more complex to solve but

nevertheless Eq. 3.2 and Eq. 3.3 remain good approximations for a convenient measure for the tendency of particles to attain velocity equilibrium with the fluid.

The time response of the particles, and the related velocity lag, introduces not only a source of error in the measurement phase but also cut-off frequency limit. If the particle-fluid density ratio is high, as in the case of air when it is seeded, the particles introduce a low-pass filtering behavior as described well by Mei [50] and Henning and Ehrenfried [46]. In fact, the flow velocity oscillations with a frequency higher than the cut-off frequency can not be followed by the particles. Mei [50] propose an equation to estimate the cut-off frequency, based on a 50 % energy response of the particle:

$$f_{cut-off} = \frac{\upsilon}{\pi}(\frac{\xi_{cutoff}}{d_p})^2 \tag{3.4}$$

Where υ is the kinematic viscosity of the fluid while the $\xi_{\text{cut-off}}$ coefficient is defined with the following equation:

$$\xi_{cut-off} = ((\frac{3}{2\rho^{0.5}})^\gamma + (\frac{0.932}{\rho - 1.621})^\gamma)^{1/\gamma} \tag{3.5}$$

which is valid for $\rho > 1.621$ while $\gamma = 1.05$.

3.1.1 PIV setup

PIV measurements have been performed using a Dantec-Dynamics PIV system. The measurement setup is equipped with two lasers: a low sampling rate laser for average measurements in the main flow and a high sampling rate for high-frequency measurements in the main and coolant flows. The first is a 120mJ New Wave Solo Nd:YAG pulsed laser operating with a wavelength of 532nm and with a maximum sampling rate of 15Hz. The second one for the Time-Resolved approach is a Nd:YAG pulsed laser (Litron LDY303), operating at a wavelength of 527nm with a power range of 0-20mJ

and sampling rate range of 0.2-20kHz. A Phantom Miro M340 camera with a resolution of 2560x1600 pixels and 12-bit sensor depth was used to record the images. The sensor is a 4 Mpx CMOS 25.6 mm x 16.0 mm with 10 μm pixel size. The frequency acquisition is about 800 fps in full-size sensor mode but can be increased up to 50.0 kHz, reducing the camera resolution (image crop). The camera has been equipped with two different lenses according to the measurement to be carried out: a Micro NIKKOR 60mm $f/2.8$ and a Sigma 150mm $f/2.8$. All devices are controlled by $Dantec-FlowManager©$ commercial software that allows the synchronization of the system and the acquisition and the processing of the data. A programmable timing unit (PTU) controlled by the software provides the trigger signals to the camera and lasers systems. The particles, with a mean diameter of about 1μm, have been generated by means of a Laskin nozzle [51] and used to seed both the main and coolant flows.

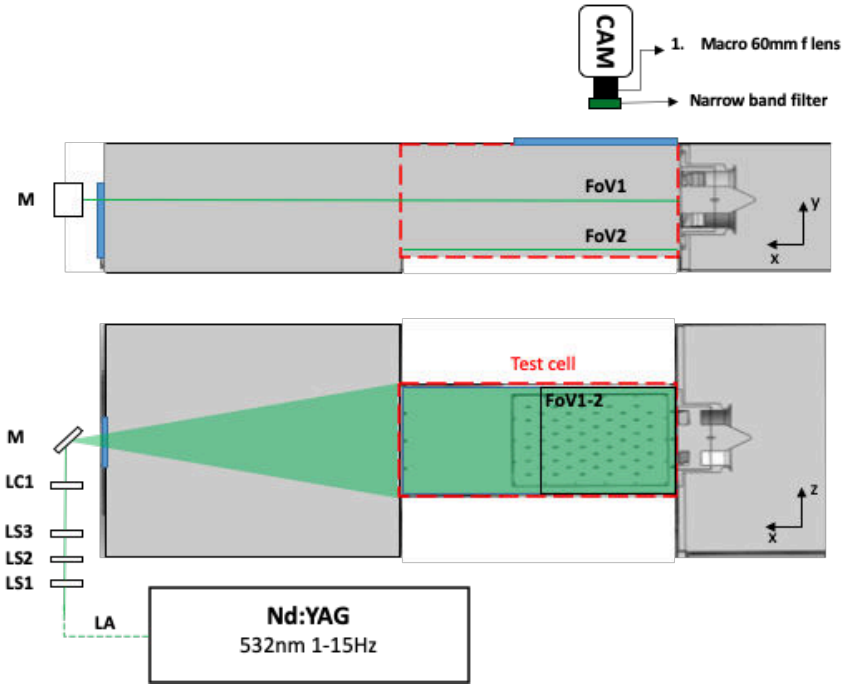

Figure 3.2: PIV setup XZ-Plane measures

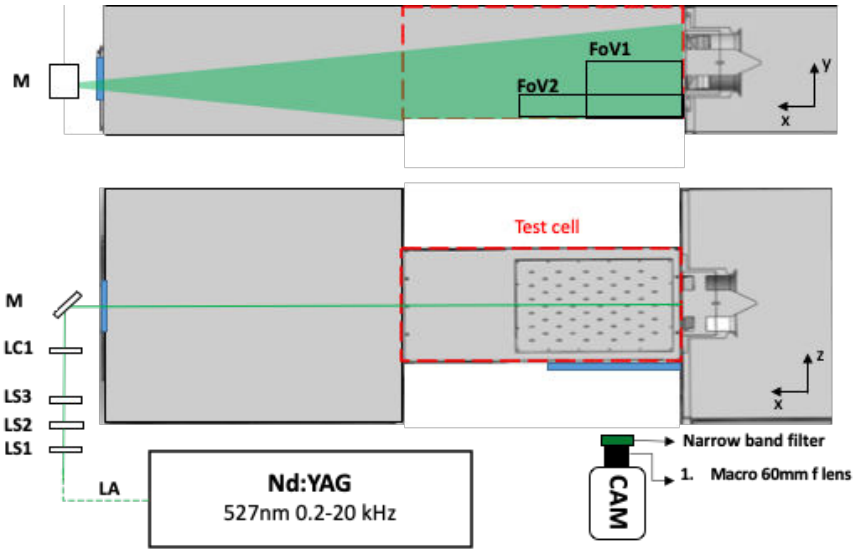

Figure 3.3: PIV setup XY-Plane measures

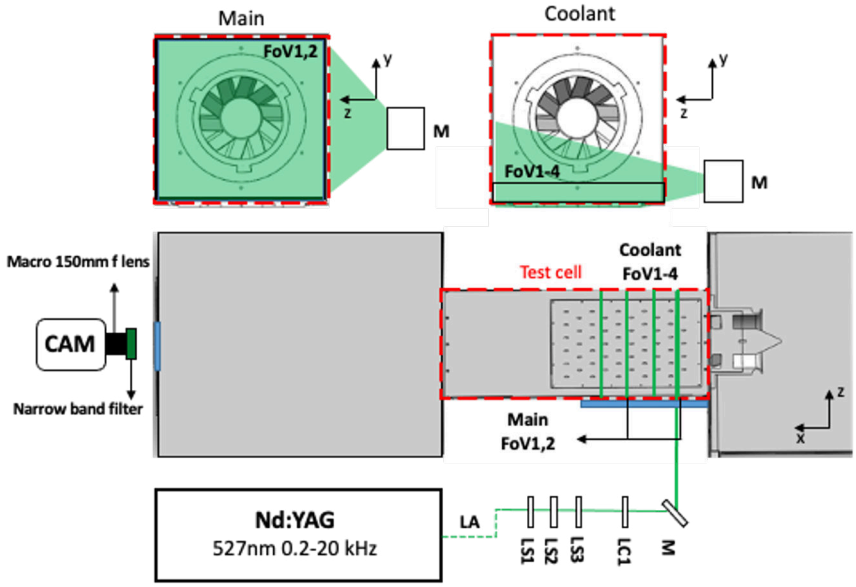

Figure 3.4: PIV setup ZY-Plane measures

Moving more in detail, in order to analyze as the PIV setup is con-

figured, Fig. 3.2, Fig. 3.3, and Fig. 3.4 show the various configurations as the measurement planes and Fields of Views (FoV) varied during the different experimental investigations. In all cases, the laser beam is brought into an optical trail, designed during this Ph.D. course, through a laser arm (LA). The optical trail consists of the first block of three spherical plane lenses (LS): the first is the concave plane (LS1) and the following two convex planes (LS2,3). The focal length of these lenses and their relative distance are vary from measure to measure to obtain the desired focal line and laser sheet thickness by varying the FoV and measurement planes. Following the spherical lenses, there is a cylindrical plane concave lens (LC1) for the laser sheet generation. Again, many cylindrical lenses with different focal lengths were used based on the desired laser sheet width. Finally, a silver mirror (M), mounted on an adjustment system, allows projecting and aligning the laser sheet inside the test rig. The thickness of the laser sheet is variable between 0.5 and 1mm through the LS lens block regulation. On the XZ and XY planes, the thickness has been adjusted to about 0.5mm while for the ZY plane to 1mm. This is because the ZY plane, being perpendicular to the preferential direction of the flow, is more subject to the seeding drop out from the measurement plane. In this sense, an increase in the thickness of the laser sheet brings benefits to the measurement. To increase the Signal to Noise Ratio (SNR) of the acquired images, the test cell was painted with opaque black to reduce the effects of light reflection. Besides, the Miro camera has been equipped with a narrow bandpass filter centered on the lasers wavelengths. As is shown in Fig. 3.2, Fig. 3.3, and Fig. 3.4, the macro lens with a 60mm focal length was used for the measurements on the XY and XZ planes, while the lens with a focal length of 150mm for the ZY planes. This is to have an optimal magnification factor (ratio between CCD and "real space" distances) in all tests. In fact, the ZY measurement planes are located very far from the optical access of the camera. For what concerns the seeding system, both the main and coolant flow were seeded. Referring to Fig. 2.1, the seeding is injected into the principal air intake as regarding the main flow and the calibrated orifice upstream of the cooling air circuit for the effusion coolant flow. Thanks to the presence of the plenum, the homogeneity of

the seeding for the coolant flow is guaranteed. For the main flow, to ensure a good homogeneity, two distribution pipes were positioned on the suction intake and are characterized by the presence of dozens of micro-holes each for the distribution of the seeding. As previously mentioned, the seeding particles are made by olive oil with a diameter of about 1 μm. In accordance with this information, taking into account the density of oil and the air kinematic viscosity (at ambient temperature), it is possible to calculate, through Eq. 3.4, the cut-off frequency of the PIV setup. This turns out to be ≈12kHz, well above the higher frequency investigation limits of this work (5kHz).

As shown in Fig. 3.2, measurements were made on the XZ planes on the plane of symmetry (FoV1) and on a plane distant 18 mm ≈ $3D_{\text{eff}}$ far from the plate (FoV2). In both cases, the measurements were acquired at low frequency (5Hz) and with two camera positions to cover each FoV: FoV1 = FoV1a + FoV1b and FoV2 = FoV2a + FoV2b. An overlap of 10% between the adjacent FoVs was guaranteed, and the results of the overlapped zone were interpolated in the post-processing phase. On the XY plane, as shown in Fig. 3.3, Time-Resolved measurements were instead carried out with acquisition frequency range f = 1500 - 5000 Hz. The main flow was investigated in FoV1, while in FoV2 the coolant one. Again, two camera placements were required for the FoV2 with a 10% overlap. Finally, for the ZY plane (Fig. 3.4), both low and high-frequency measurements were made. At low frequency (5Hz) was investigated the main flow on FoV1,2, which are positioned at a distance of 0.5 and 1.5 D_{SW} respectively from the swirler. High-frequency investigations (1.5KHz) were made to the 4 different FoV1-4, positioned at the leading edge of the 1st, 3rd, 5th, and 7th holes rows. In conclusion, Table 3.1 is reported summarizing, for each FoV survey, the acquisition frequency, the number of samples acquired, and the IA adopted.

Data Reduction

The data reduction for each set of image pairs is carried out using an adaptive grid iterative method approach. The Adaptive PIV method is an

	Plane XZ	Plane XY		Plane ZY	
	Main FoV1,2	Main FoV1	Coolant FoV2	Main FoV1,2	Coolant FoV1-5
freq.	5Hz	2-5kHz	1.5kHz	5Hz	1.5kHz
N samples	500	1000 - 3000	1000	500	1000
IA size	64x64	32x32	32x32	64x64	32x32

Table 3.1: Principal information of the PIV measurements by varying the FoVs

automatic and adaptive method for calculating velocity vectors based on particle images. The method iteratively adjusts the size and shape of the individual interrogation areas(IA) in order to adapt to local flow gradients [52]. During the iterative phase, the obtained movement vector calculated through the first standard cross-correlation is used as a new estimate for the second iteration window shift. From the previous iterative process results, a new run is made, but this time with a refinement of the size and shape of the interrogation area. The correlation method used by the software is a standard cross-correlation (SCC) type, based on the correlation analysis in the frequency domain [53]. An adaptive method for calculating velocity represents the most suitable choice to avoid the" in-plane drop-out" loss of particles. In fact, as will be shown next, the seeding particles in the time delay between the laser pulses can leave the interrogation area. Loss of these particle images is known as the "in-plane drop-out", and this inconvenience reduces signal strength and, as a result, the number of valid vectors that can be processed because the high of the first peak of the cross-correlation is compromised. The maximum and minimum IA chosen vary from measure to measure, according to the plan taken into consideration, and the image crop applied to the camera sensor. IA smaller than 32x32 pixels have never been set. Furthermore, validation is used to prevent outliers from disturbing the iterations and thus the velocity measurements. The validation is done by first applying peak validation on the image cross-correlation and secondly by comparing each vector to its neighbors using the Universal outlier detection algorithm. The peak validation schemes applied in order to invalidate vectors based on the image correlation peaks works as follow:

- Peak Height Ratio: for each IA and iteration, the ratio between the two highest correlation peaks is calculated. During the post-process a lower Peak Height Ratio limit equal to 1.5 has been introduced in order to validate the calculated displacement.
- If either Peak validation fails, the corresponding vector will be rejected and substituted thanks to the "Universal Outlier Detection" by which the rejected vector is replaced with the median of the neighbor vectors.

Subsequently, the raw data obtained with the $Dantec - FlowManager©$ were then post processed in terms of average, statistical analysis (turbulence and root mean square), uncertainty, frequency, vorticity, and others post-process, which will be shown in the results, with programs developed in MatLab© environment.

3.2 Adiabatic Effectiveness Measurement: Fast Response Pressure Sensitive Paint.

Pressure sensitive paint (PSP) is an organic substance, composed by oxygen sensitive molecules embedded in the paint solution using a polymer binder permeable to oxygen. Through the exploitation of the luminescence behavior of these molecules, PSP can be used to measure the oxygen concentration of the atmosphere surrounding the paints, which in turn can be linked to the partial pressure of air. The oxygen sensitive molecules are excited by the absorption of a photon, to higher energy levels by an incidence light of a certain frequency (UV light). From the excited state the molecule has several competing relaxation paths. The path of interest for PSP involves a forbidden transition to an excited triplet state from which the molecule may simply emit a photon. However, if oxygen is present, the molecule may interact with it, transmitting its energy into a vibrational mode of the oxygen (Fig. 3.5[1]). This radiationless deactivation at lower frequency results in a system where the luminescent intensity from the molecule is a function of

[1]http://www.psp-tsp.com/

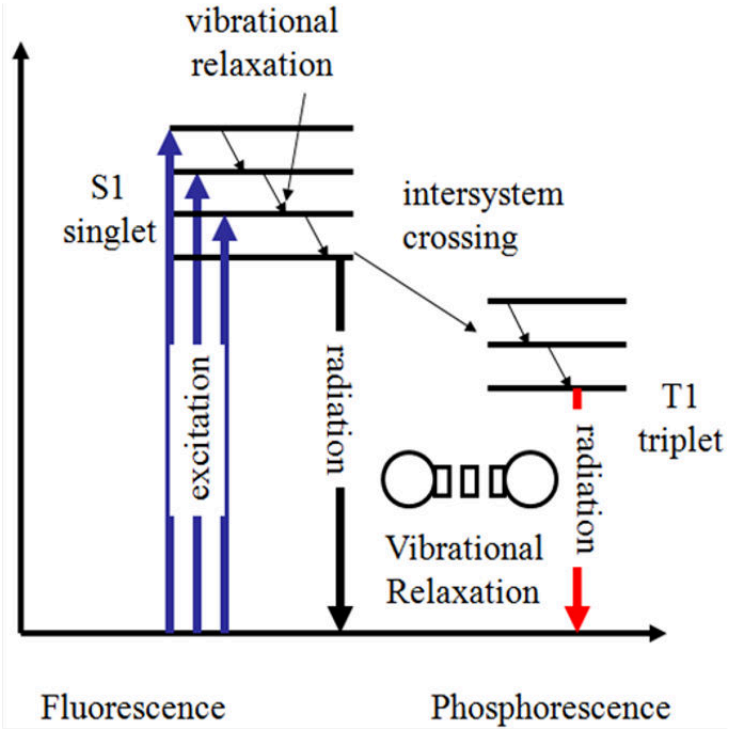

Figure 3.5: Oxygen Quenching

the partial pressure of oxygen to which the molecule is exposed; the intensity of the light increases as the oxygen concentration in the ambient around the sensitive molecules is decreased. This well known phenomenon is called *oxygen quenching* [54]. PSP is sprayed on the surface of the test article where the oxygen concentration has to be measured.

One of the limits that emerged for this measurement technique is that conventional formulation for the PSP paint typically uses a polymer as a blend material that strongly slows down the paints response time. This produces a slower response time, which is strongly governed by the gas diffusion rate, and therefore oxygen, in the binder. Usually, the response time is about seconds. As is known, in the turbo-machinery field, however, many of the aerodynamic phenomena are strongly of unsteady type. These traditional paints would therefore not allow a complete characterization of the flows ex-

cept that in average terms. For this reason, there has recently been an effort to develop paints with reduced response times. A detailed review about the development of PSP for unsteady testing was done by Gregory et al. [55]. The main parameters useful to characterize the Fast Pressure Sensitive Paint (FPSP) are the response time and the signal-to-noise ratio (SNR):

$$\tau_{diff} \propto \frac{h^2}{D_c} \tag{3.6}$$

From this formulation, it is possible to understand as the response time, which is a function of the oxygen diffusion time (3.6) of the paint, is governed by two constants: the paint thickness (h) and the diffusion coefficient (D_c). The diffusion time increases with the square of the paint thickness (h) and decreases with the diffusion coefficient (D_c). However, as the paint thickness decreases, the paint luminescence also decreases, degrading the SNR. For this reason, acting on parameter h, one of the strategies used was to find the best trade-off between response time and SNR value [56]. The second strategy to reduce the response time is the increasing of the diffusivity rate of gas in the paint binder using porous material. In Fig. 3.6 it is shown the difference between conventional polymer-based PSP and porous PSP. For conventional PSP, oxygen molecules need to permeate into the binder layer to produce the oxygen quenching. On the other hand, the luminophore in porous PSP is opened to the test gas so that the oxygen molecules are free to interact with the luminophore. The open porous binder creates a surface that reacts much more quickly to oxygen concentration changes. For this reason, the porous PSP are the key to achieve the goal of measuring oxygen concentration in high frequency. Furthermore, a larger effective surface area, due to the porous surface, improves luminescence intensity and, therefore, the SNR.

Measurement Theory

Since the PSP is a sensor of the oxygen concentration, this paint is suitable for gas concentration technique based on the heat and mass transfer

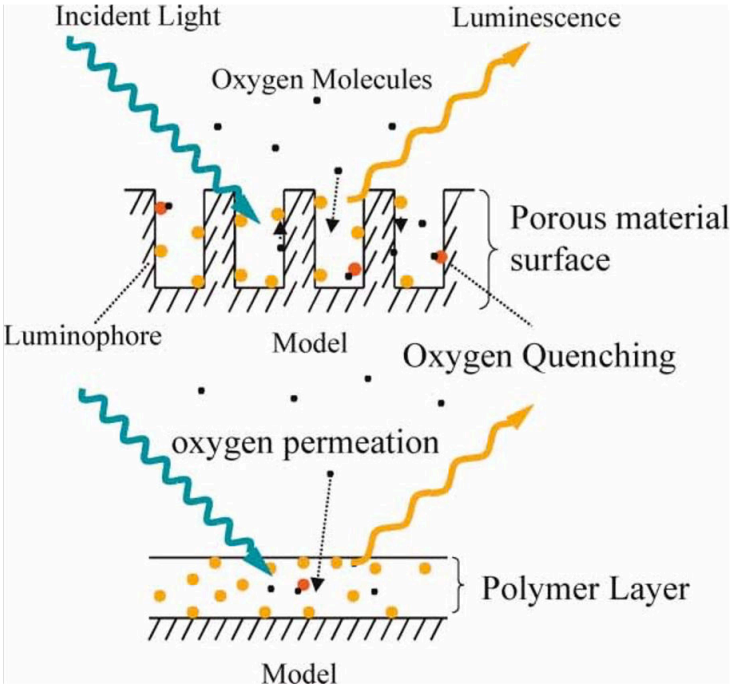

Figure 3.6: Comparison of porous and conventional PSP [57].

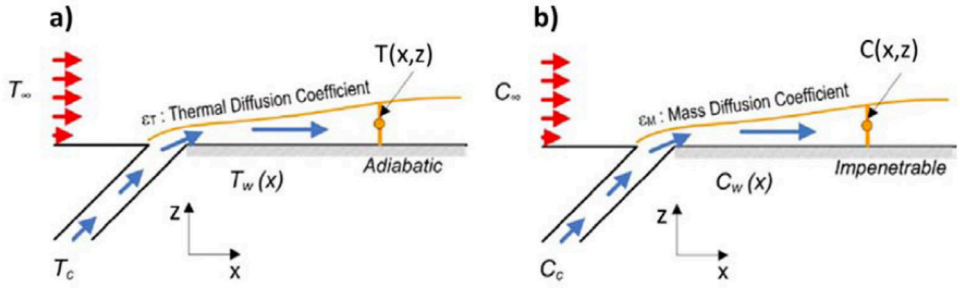

Figure 3.7: Heat and mass transfer analogy for film cooling situations: thermal (a) and mass transfer (b) boundary conditions [59]

analogy [58], with the ultimate goal of evaluating the adiabatic effectiveness.

Starting from a simple 2D film configuration reported in Fig. 3.7a, the

governing equation for the heat transfer into a turbulent boundary layer is:

$$G_x \frac{\partial T}{\partial x} + G_z \frac{\partial T}{\partial z} = \rho(\epsilon_T + \alpha) \frac{\partial^2 T}{\partial^2 x} \tag{3.7}$$

where G is the mass flux per unit of area, ϵ_T and α are respectively the turbulent and laminar diffusivity. In the case of adiabatic wall, the boundary conditions are the following:

$$T(z = 0) = T_{ad} \tag{3.8a}$$
$$\frac{\partial T}{\partial z}(z = 0) = 0 \tag{3.8b}$$
$$T(z > \delta_f) = T_\infty \tag{3.8c}$$
$$T(x = 0) = T_c \tag{3.8d}$$

For the analogous case for mass transfer situation, where the hot mainstream has a tracer element concentration of C_∞ and the coolant has a tracer concentration of C_c (Fig. 3.7b), the governing equation of tracer gas diffusivity inside the boundary layer are:

$$G_x \frac{\partial C}{\partial x} + G_z \frac{\partial C}{\partial z} = \rho(\epsilon_C + D) \frac{\partial^2 C}{\partial^2 x} \tag{3.9}$$

with ϵ_C representing the turbulent mass diffusivity. An impenetrable wall situation yelds to the following boundary conditions:

$$C(z = 0) = C_w \tag{3.10a}$$
$$\frac{\partial C}{\partial z}(z = 0) = 0 \tag{3.10b}$$
$$C(z > \delta_f) = C_\infty \tag{3.10c}$$
$$C(x = 0) = C_c \tag{3.10d}$$

Hence the set of equations for heat and mass transfer situations have same modelling expression [60]. Moreover, if the boundary conditions of the two analogous problems are the same and if the molecular and turbulent Schmidt number Sc_T are identical to molecular and turbulent Prandtl number Pr_T respectively (i.e. turbulent Lewis number Le_T, shown in Eq. 3.11, equal to one), the solutions of the heat and mass transfer phenomena are identical.

$$Le_T = \frac{Pr_T}{Sc_T} = \frac{\epsilon_T + \alpha}{\epsilon_C + D} \approx 1 \tag{3.11}$$

In turbulent flows, experimental results suggest that the coefficients of turbulent transport diffusivity, represented by the Sc_T and Pr_T numbers, have similar magnitudes [61]. Concerning the applicability of the heat and mass transfer analogy to film cooling situations with moderate Mach number, turbulent main flow and high blowing rate, the mixing process of interested generally occurs far from the wall, where turbulence effects are dominant, and therefore the analogy is generally satisfied. Even if the hypothesis of turbulent Lewis number is met ($Le_T = 1$), the similarity of molecular diffusion may not be satisfied and thus Lewis number may deviate from one: in this case, the difference between Pr and Sc influences the heat/mass transfer rate near the wall boundary layer in the thin viscous sub-layer [60]. However, only a small influence of molecular parameters is expected as a consequence of the zero temperature/concentration gradient at the adiabatic/impenetrable wall of the test plate.

Assuming the heat-mass transfer analogy valid, if a tracer gas without free oxygen is used as coolant in a film cooling system, it is straightforward to replace the temperature definition of film cooling effectiveness by mass fractions of oxygen [58]:

$$\eta_{ad} = \frac{T_{main} - T_{ad}}{T_{main} - T_{cool}} = \frac{C_{main} - C_w}{C_{main}} \tag{3.12}$$

where C_{main} is the oxygen concentration of main free stream and C_w is the oxygen concentration in proximity of the wall. In order to express Eq. 3.12

in terms of partial pressure of oxygen, as measured with PSP, the expression of adiabatic effectiveness is elaborated using the molecular weights [62]:

$$\eta_{ad} = \frac{C_{main} - C_w}{C_{main}} = 1 - \frac{1}{(1 + (\frac{P_{O_2;air}/P_{O_2;ref}}{P_{O_2;fg}/P_{O_2;ref}} - 1)\frac{W_{fg}}{W_{air}})} \tag{3.13}$$

Subscripts fg and air stand for a case with foreign gas (without free oxygen) and air injection trough cooling system respectively; moreover ref is used to identify a reference case. Therefore, in order to evaluate the adiabatic effectiveness distribution using PSP technique, four types of images are needed for each tested flow condition; the experimental apparatus must be equipped with the same illumination system and camera used for calibration test:

1. The first images set (Dark Images) is acquired with the UV illumination system switched off and it is necessary to correct the background noise of the camera CCD (I_{dark}).

2. Using a tracer gas for the cooling line and air for the mainstream, a second image set (*Tracer Images*) is acquired setting the desired flow conditions.

3. The third images set (*Air images*) is acquired imposing the same conditions of the previous one, but using air as coolant instead of tracer gas.

4. The last type of images set (*Ref Image*) is captured with no flow condition and it represents the reference intensity field of the measurements (I_{ref}).

From the ratio of the reference (I_{ref}) and tests 2 intensity images, both corrected with the dark field (test 1), the calibration curve can be used to estimate pixel by pixel the normalized partial pressure of oxygen in case of tracer gas injection through holes array ($P_{O_2;fg}/P_{O_2;ref}$). In the same way the intensity image acquired with the third test (air injection) is elaborated in order to achieve the ratio $P_{O_2;air}/P_{O_2;ref}$. Finally both the distributions of partial pressure of oxygen can be combined, as suggested by Eq. 3.13, to estimate the bi-dimensional map of adiabatic effectiveness.

An important aspect of the PSP technique is that it allows to perform tests which can be considered really adiabatic. In the case of a thermal technique such as IR, TLC or TSP thermography the adiabaticity is guaranteed when there are no thermal gradients across the test plate; this requirement can be only partially satisfied using a low-conductivity material; even in these cases, thermal conduction corrections, that can be detrimental to the measurement accuracy, must be employed. Caciolli et al. [63] carried out a comparison between PSP and TLC measurements in order to highlight pros and cons of both.

3.2.1 PSP setup and calibration

The PSP measurements for the adiabatic effectiveness estimation was performed using commercial FPSP called TurboFIB©supplied by Innovative Scientific Solutions company. This paint is a single luminophore with a fast response frequency about 1kHz. The paint presents a reduced temperature sensitivity (0.4% per °C) and guarantees a pressure sensitivity of 800 Pa. The emission spectra of TurboFIB©is reported in Fig. 3.8. In accordance with these specifications two UV 400nm LED system, able to work in continuous or pulsed mode, provides the adequate light source for paint excitation. To acquire the images was used a Phantom Miro M340 camera with a resolution of 2560x1600 pixel and 12 bit sensor depth. Further camera specifications can be found in the PIV setup section. The camera has been equipped with a macro lens: Micro NIKKOR 60mm f/2.8. A blu (410nm) narrow band filter is equipped on the led and a red one (610nm) on the camera. Two sketch respectively for the calibration and for the adiabatic measurements

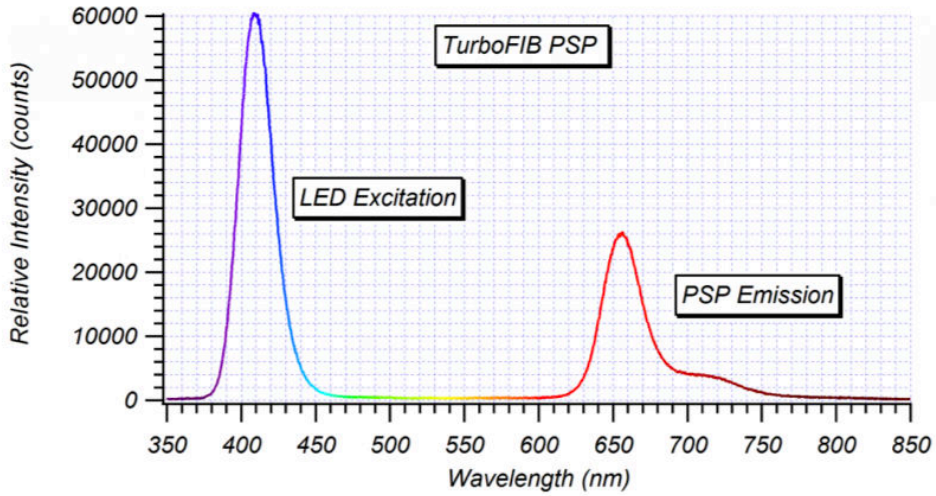

Figure 3.8: Emission Spectra of TurboFIB©PSP Excited Using an UV LED.

set-up are shown in Fig. 3.9 and Fig. 3.10 respectively. The UV LED worked with continuous light emission while the camera in high frequency mode at 1 kHz (FPSP frequency response limit), both during the calibration and test measurements. As shown in the Fig. 3.10, during the test phase, the FoV used to measure the adiabatic effectiveness includes from the 1st to the 7th row of holes with a spatial resolution about 5.6 pixel/mm. During the tests nitrogen was used as a tracer gas. The molecular weight of nitrogen, similar to that of air, allows testing with the same density ratio as the PIV measurements (DR = 1).

PSP calibration

Before their use on a test model as a oxygen partial pressure measurement device, PSP must be accurately calibrated in a dedicated hardware. The calibration apparatus, depicted in Fig. 3.9, is constituted by a vacuum/pressure chamber, housing an aluminum test plate with Pressure Sensitive Paint, where pressure on the test plate can be controlled. The calibration environment can be either put in vacuum conditions, by means of a vacuum

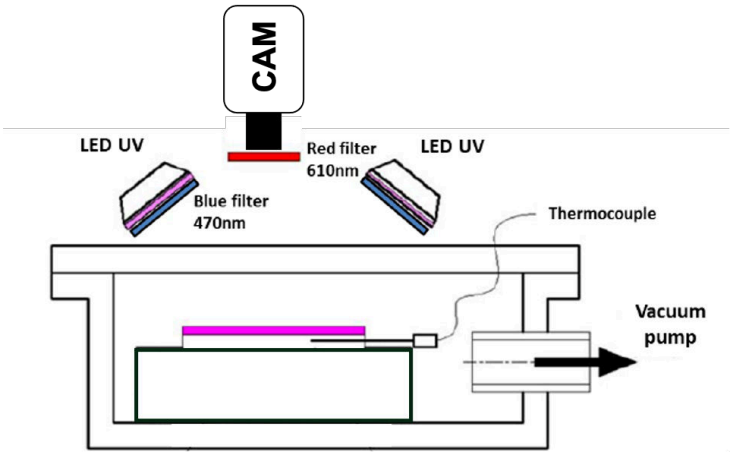

Figure 3.9: PSP calibration apparatus.

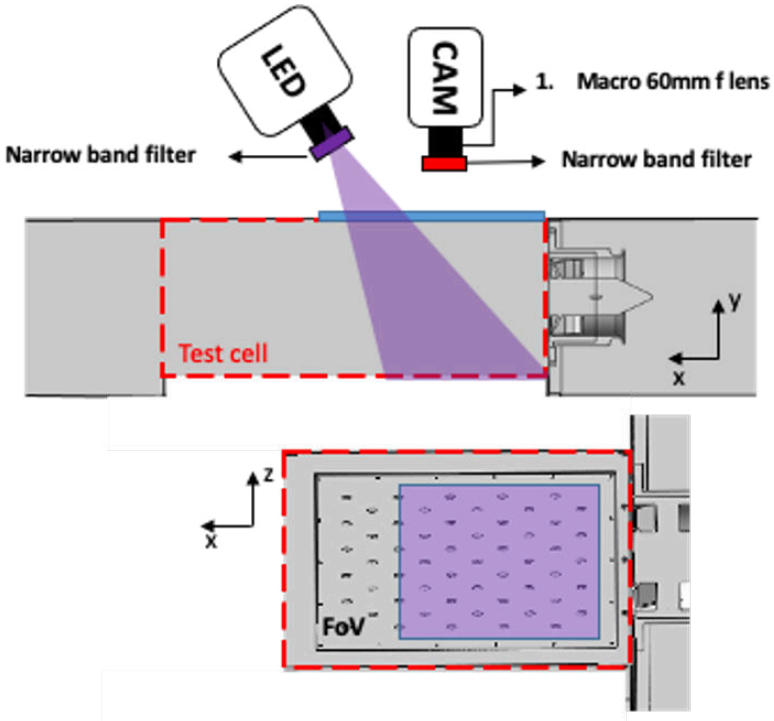

Figure 3.10: PSP measurements set-up.

pump. Only the oxygen partial pressure light intensity response of the paint has been calibrated due to the low temperature sensitivity of the TurboFIB©.

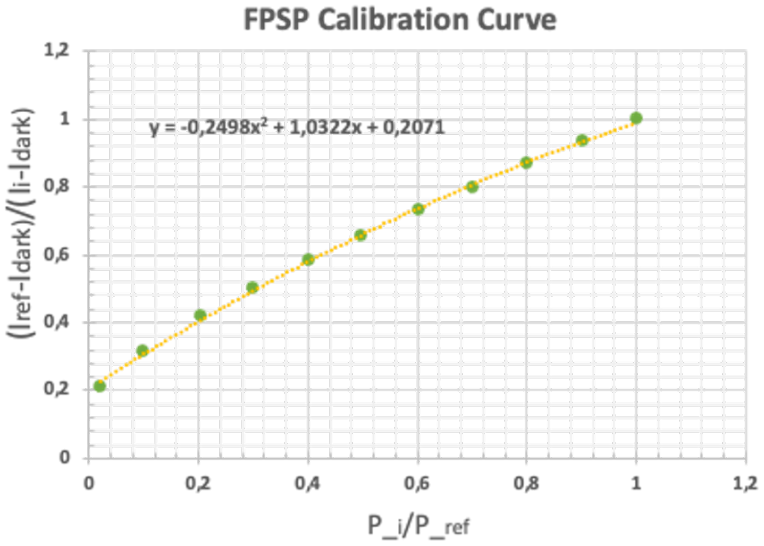

Figure 3.11: PSP calibration curve

Since, for PSP tests, a combustion chamber static pressure of 97kPa had to be imposed (Section 2.2), the maximum expected pressure on the effusion plate surface is slightly higher than this value. Therefore, the PSP calibration was carried out from 1000 Pa to the ambient pressure P_{atm}. Fig. 3.11 shows the calibration results where a second order polynomial was used to define a relation between the camera response $((I_{ref} - I_{dark})/(I - I_{dark}))$ and the measured oxygen partial pressure (P/P_{ref}).

Thanks to the linear response of paints to UV light exposure, the normalization $((I_{ref} - I_{dark})/(I - I_{dark}))$ makes it possible to use the calibration curve also during the tests to obtain the partial oxygen concentration (P/P_{ref}). Therefore, if the camera is operated in the linear range, results don't depend on the intensity of the UV light used for PSP excitation, as long as it remains the same for test image and reference image and its spectral content doesn't change (i.e. same illumination system). For this reason, an analysis of the linearity response of the CCD at low counts values is necessary to avoid systematic errors during the calibration and test phases. In fact, to I_{ref}, which is in the lower intensity light response zone of the PSP, it must correspond a CCD count number within the linearity range of the

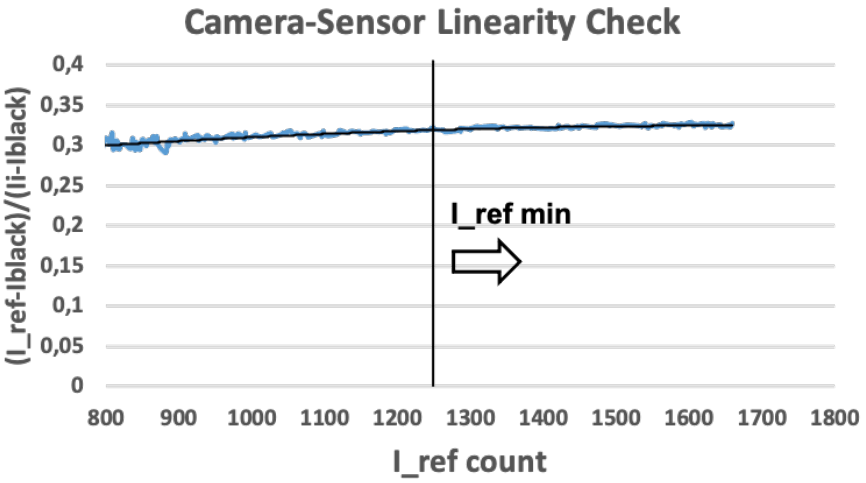

Figure 3.12: Linearity check of the camera CCD sensor.

CCD to have a useful calibration and measurement. For this reason, by varying the UV light intensity and therefore the I_{ref} (P_{atm}) in the test plate with Pressure Sensitive Paint, the calibration apparatus was put in vacuum conditions ($\approx$ 15000Pa) to see at what minimum I_{ref} CCD count value the relationship $(I_{ref} - I_{dark})/(I - I_{dark})$ was no longer constant (out of linearity range). The check was performed with an acquisition frequency of 1000 Hz equal to the calibration and test frequency. The results of the linearity check are shown in Fig. 3.12. The minimum count number from where good linearity of the sensor starts has been identified for 1250 counts. During the test phase, therefore, the UV LEDs were adjusted to guarantee I_{ref} values $>$ 1250 counts over the entire FoV (Fig. 3.10).

3.3 Uncertainty analysis and estimation

Before proceeding to the PIV and PSP uncertainty evaluation presentation, the basic formulas for the definition and propagation analysis of the uncertainty are summarized. The Kline and McClintock [42] method was used. The following equations give the propagation of independent uncer-

tainties of independent variables of a function M:

$$M = f(m_1, m_2, m_3, ...m_n) \pm \Delta M \tag{3.14}$$

$$\Delta M \approx \pm \sqrt{\sum_{i=1}^{n} \left(\frac{\partial f}{\partial M_i} \right)^2 u_i^2} \tag{3.15}$$

where m_i represents the n independent variables and u_i their uncertainty contributions.

For measurements of unsteady type M can be considered as an instant value measured in a time step t and ΔM its related instantaneous uncertainty. As regards the composition of the error on the mean value $\overline{M}$ of an unsteady quantity, constructed through the time average arithmetic of several instantaneous measurements, can be calculated as follow:

$$\overline{M} = \frac{1}{N} \sum_{t=1}^{N} M_t \tag{3.16}$$

$$\Delta \overline{M} = \pm \sqrt{\left(\frac{1}{N^2} \sum_{t=1}^{N} \Delta M_t^2 \right) + p_{\overline{M}}^2} \tag{3.17}$$

$$p_{\overline{M}} = \pm t_{C.I} \frac{\sigma_M}{\sqrt{N}} \tag{3.18}$$

Where $\overline{M}$ is the arithmetic mean of the N instantaneous M_t values and $\Delta \overline{M}$, calculated as in Eq. 3.17, the related uncertainty. Two different terms

compose $\Delta\overline{M}$; the first one is the arithmetic mean of the instantaneous uncertainty values while, in agreement with Wilson and Smith [64], Freitas [65], and Wil [66], the second one $p_{\overline{M}}$ is the precision uncertainty additional term. $t_{C.I}$ is the t-statistic describing the desired confidence interval, and σ_M is the standard deviation of the samples. The precision uncertainty term is statistically derived and requires independent measurement samples. The precision uncertainty reduces by $1/\sqrt{N}$ with the number of samples. Taking into account a confidence interval of 95%, $t_{C.I}$ must be imposed equal to 1.96 using a normal distribution. As can be seen in eq.3.18 with $N \to \infty$ so $p_{\overline{M}} \approx 0$; for the measurements (PIV ad PSP) carried out during this thesis, the number N of samples has always proved sufficient to make the second term of the Eq. 3.17 negligible with respect to the first one.

3.3.1 PIV Uncertainty

It is well known that there are dozens of error sources in a PIV measurement [67]. Errors can derive from the system calibration (CCD not perpendicular with the measurement plane and others), the physical distance of the measured plane (affect the accuracy of the magnification factor), image distortion due to the aberration of lenses, CCD noise and distortion, non-perfect alignment between the two laser source, laser power fluctuations. Moreover, due to pulse timing precision, non-uniformity of seeding, the mismatching of pair particles can occur, the exit of particles from the IA in the time between the two laser pulse ("in-plane - drop-out"), loss of particle due to "out-plane drop-out", up to the problem connected to the response time and the frequency cut-off previously analyzed given by the size and particles density. The impossibility of weighing and taking into account all these sources of error means that we move towards correlative or statistical methods to estimate PIV measurements uncertainty. In the following work, two were chosen and used. The first is the correlative method proposed by Charonko and Vlachos [68] based on the peaks ratio estimate. The second is a statistical one derived by works of Persoons [69] and Wieneke [70], in which for computing the uncertainty of a single vector inside an interrogation window, one could

in principle divide the interrogation window into smaller parts and apply a standard deviation analysis with the larger number of sub-grid vectors.

Correlation Peak Ratio Method

Charonko and Vlachos [68] presented a relationship between the cross-correlation displacement error, the resulting uncertainty, and the Correlation Peak Ratio (PR) of individual displacement measurements both for standard cross-correlation (SCC) and robust phase correlation (RPC) methods. They discovered that a well-defined relationship between the PR and the uncertainty. For the SCC method, which is used by the DynamicStudio during the images post-process, the uncertainty relationship is quantified using a three-term formulation power-law:

$$\Delta u_{pix} = \pm t_{C.I} \sqrt{\left(13.1 exp\left(\frac{1}{2}\left(\frac{PR-1}{0.317})^2\right)\right)\right)^2 + (0.226 PR^{-1})^2 + (0.08)^2} \tag{3.19}$$

$$u_{rel} = \frac{\Delta u_{pix}}{U_{pix}} \tag{3.20}$$

u_{pix} is the uncertainty expressed in pixel and PR the cross-correlation quality ratio, the ratio of the height of the first peak to the second in the spatial correlation domain. The equation works in terms of pixels velocity modulus as shown in Eq. 3.20. In fact, the peaks ratio method does not take into account the contributions of velocity on the different spatial coordinates. Eq. 3.19 applies in the range $1 < PR < 10$. In the presented work, the post-process data phase, only the vectors that presented a $PR > 1.5$ were validated, reducing the value of the final uncertainty estimate and the quality of the measurements. The standard uncertainty was then multiplied by a coverage factor of $t_{C.I} = t_{95\%} = 2.0$ to yield an estimate of the

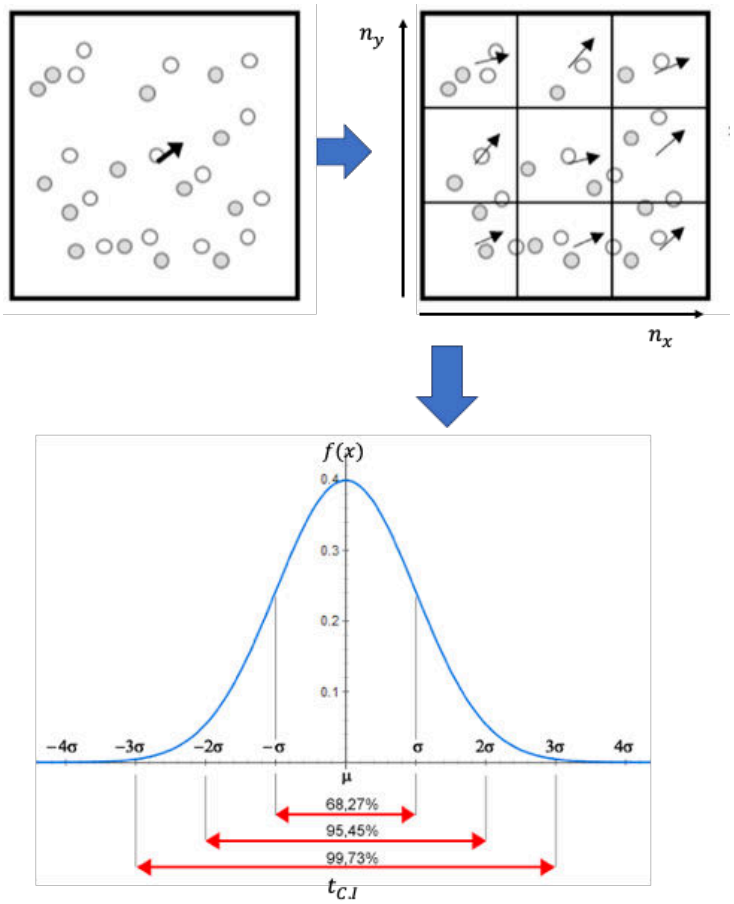

Figure 3.13: Principle of uncertainty estimation by splitting into sub-windows [70]

95% confidence interval using the large sample approximation for a normal error distribution and finally is used to calculate the relative uncertainty of the global 2D velocity value. For each velocity value of the FoV and for each instantaneous acquisition, this evaluation is then processed through the equation 3.17 previously shown and finally transformed in m/s for a global estimate of the velocity error of the mean flow field.

Statistic Method

For what concerns the statistic uncertainty evaluation method shown by Persoons [69] and Wieneke [70], the general concept is shown in Fig. 3.13. For

computing the uncertainty of a single vector inside an interrogation area, one could in principle divide the interrogation window into smaller parts where each sub-window corresponds to a displacement vector with a higher noise level due to fewer pixels and fewer particles or decide to not divided the IA grid into sub windows and use the vectors surrounding the reference one. The uncertainty estimate can be made using the following equations:

$$i = x, y.\ spatial\ coordinates \tag{3.21}$$

$$F = \sqrt{n_{x,sub-windows} \cdot n_{y,sub-windows}} \tag{3.22}$$

$$\Delta u_i = \pm \frac{t_{C.I}}{F} \sqrt{\frac{1}{n_v} \sum \left(u_i - \overline{u_i} \right)^2} \tag{3.23}$$

where the subscript i indicates the components along the 2D spatial coordinates and F is the re-fitting factor. If there is not a re-fitting of the IA into sub-windows and are used the surrounding vectors to estimate the uncertainty of the reference one, F=1. Finally the uncertainty along the two spatial coordinates (Δu_{x} and Δu_{y}) of each vector of each instantaneous acquisition can be calculated as shown in Eq. 3.23. The square root represents the standard deviation σ_{i} along the i coordinate of the $\mathrm{n_v}$ vectors used for the uncertainty calculation. In the equation, F is used to scale the effect of the higher noise level due to fewer pixels and fewer particles in the sub-windows. Usually, in case of re-fitting $\mathrm{n_v} = \mathrm{F}^{\,2}$. The instantaneous values along with the spatial coordinates thus obtained are then treated, according to the theory of error propagation through the equation 3.15, taking into consideration $M = U = \sqrt{{U_{\mathrm{x}}}^2 + {U_{\mathrm{y}}}^2}$. Next, the time average uncertainty maps are calculated through Eq. 3.17 to have the final mean flow field uncertainty evaluation.

PIV Uncertainty results

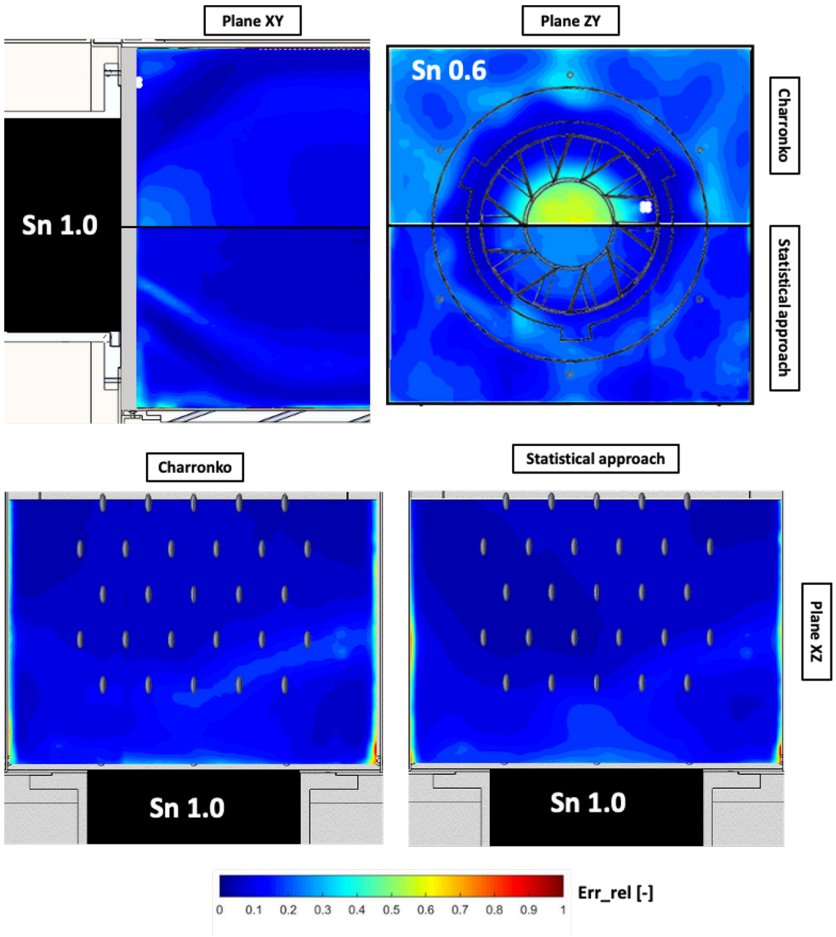

Figure 3.14: PIV uncertainty evaluation for the swirling main flow: statistical and correlative approach comparison.

The Figures 3.14 and 3.15 show the uncertainty results of the average velocity module maps, calculated with the methods previously described for the main and coolant flows along the analyzed planes. Since it is impossible to make an uncertainty analysis for all the measurements made at each test condition and for each plane and each FoV, the estimate was made for the pejorative case studies. To do this, it was taken into account how some parameters, source of error of the PIV measurements, remained unchanged during the test in the same planes: concentration of the seeding, the thickness

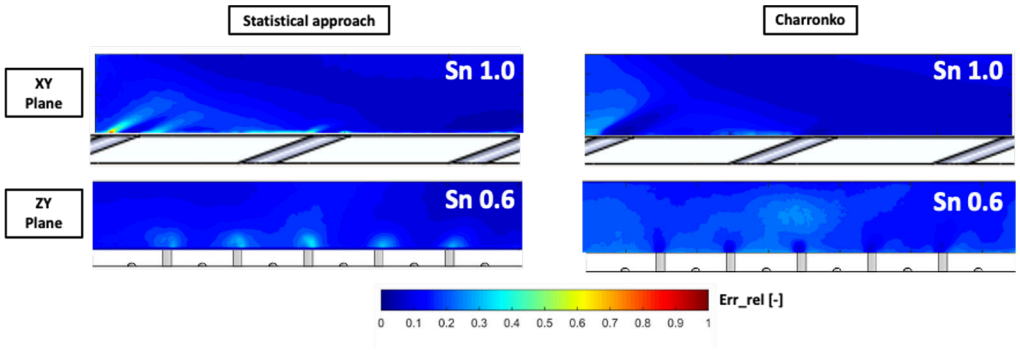

Figure 3.15: PIV uncertainty evaluation for the coolant flow: statistical and correlative approach comparison.

of the laser sheet, the intensity of the laser fluence, size of the interrogation areas and the magnification factor. While a significant parameter subject to variation is the out-plane drop-out of the seeding particles, which is certainly function of the normal velocity component on the plane of measure. For this reason, the injector with Sn = 1.0 (higher tangential velocity component) was selected along with the XZ and XY planes, while for the ZY plane, the injector with Sn = 0.6 (higher axial velocity component) one. In case of parallel FoV or FoV composition, the ones closest to the swirlers were chosen. The same criterion was applied for the coolant measurement FoVs: the test with Sn = 1.0 for the XY plane and the test with Sn = 0.6 for the ZY plane are shown. The samples used for the statistical analysis are the same ones acquired for the flow field acquisitions. The number of statistical samples, for each measurement plan, is therefore summarized in the Table 3.1. The results are shown in Figures 3.14 and 3.15. As a first consideration, it is possible to note, for all cases, a good correspondence between the two methods used for the uncertainty estimate. The correlative method presents the highest errors in the maps where smaller velocity are detected, while the statistical one shows the highest errors in the presence of strong velocity gradients. In general, the largest errors are found on the ZY plane, the one with the greatest flow out of plane velocity component. In particular in the external part of the coolant jets core. On the measurements plane close to the wall

(ZX - 18mm), it is possible to note how the uncertainty of measurement increases significantly in the impact area of the swirler jet (after the first row of holes). Along the planes of symmetry for the main flow and the coolant, it can be seen how the largest errors are reached on the shear layer of the jets (main and coolant). This is not surprising because this is where the strongest velocity gradients are and where the shear layer vortices develop in unsteady terms. In general, the average uncertainty results along the maps are quite low. On the other hand, a significant increase in areas with a strong velocity gradient, such as the shear layer of the jets and near the test cell walls, is considered normal and largely in line with other works presented in the literature [69]. Regarding the uncertainty calculated with a statistical approach for all the cases presented concerning the main flow, an F = 4 and $n_v = 16$ (IA from 64X64 up to 16x16 pixels) was used. On the other hand, for the coolant, an F = 2 and $n_v = 4$ (IA from 32x32 up to 16x16) was applied.

3.3.2 PSP Uncertainty

PSP uncertainty evaluation is a complicated task due to the number of parameters that can affect the measurement. The complexity of the relationships that link one to another makes their combination not straightforward. The contribution to the uncertainty considered within this treatment are the following:

1. CCD non-linearity
2. CCD noise
3. Paint thickness
4. UV LED lighting conditions
5. PSP temperature sensitivity
6. PSP pressure sensitivity
7. Uncertainty of the pressure transducer used in the calibration process

The 1. point represents a systematic source of error that was avoided. As explained in the subsection 3.2.1, the images camera acquisition for the adiabatic effectiveness measurements and paint calibration was carried out within the CCD sensor linearity range, thanks to a linearity check made during the calibration phase (Fig. 3.12). The following three sources of error (2., 3., 4.) affect the light intensity measured by the camera contributing to the measurement noise and the SNR reduction. The sources 5. and 6., on the other hand, are linked to the paint manufacture and are provided by the seller: temperature sensitivity equal to 0.4% $P_{\text{measured}}/°\text{C}$ and pressure sensitivity of 800 Pa (95% confidence interval). A temperature range of ±3°C was applied in the uncertainty analysis. In fact this is the maximum temperature variation measured during the tests with respect the paint calibration temperature. An estimate of the measurement noise (2., 3., 4.) was made during the calibration phase by varying the I_{ref} (paint reference light emission) for each calibration point and applying the same measurement settings used during the measurements on the test rig: same paint thickness, UV LED light in continuous mode, same camera acquisition frequency (1kHz) and CCD exposure time (900 μs). For each calibration test point (P_i), 300 images sets of the test plate were acquired respectively for I_{ref}, I_i, and I_{dark}. Following the calibration curve (Fig. 3.11) was used to process the 300 sets of images obtaining, for each calibration point, 300 P_i values. The P_i signal was then analyzed to obtain the standard deviation (σ) values for each calibration test point by varying the I_{ref} (2 θ, 95% confidence interval), thus defining the measured pressure noise. Finally, all the N uncertainty contributions on the P_i estimate (pressure noise, temperature sensitivity, pressure sensitivity, pressure transducer error) were combined using the equation:

$$\Delta P_i = \pm \sqrt{\frac{1}{N} \sum_{j=1}^{N} \Delta P_{ij}^2} \tag{3.24}$$

The uncertainty was thus estimated for the two variables $P_{O_2;fg}/P_{O_2;ref}$ and $P_{O_2;air}/P_{O_2;ref}$ (taking into account the Δ P/P =3% imposed during the

test on the rig: $P_{O_2;air} = 0.97 P_{O_2;ref}$) and composed by means Eq. 3.14 and Eq. 3.15. Where M corresponds, for this case, to adiabatic effectiveness Eq. 3.13. The uncertainty evaluation results by varying the emission intensity I_{ref} (1250-1550 counts range) are shown in Fig. 3.16.

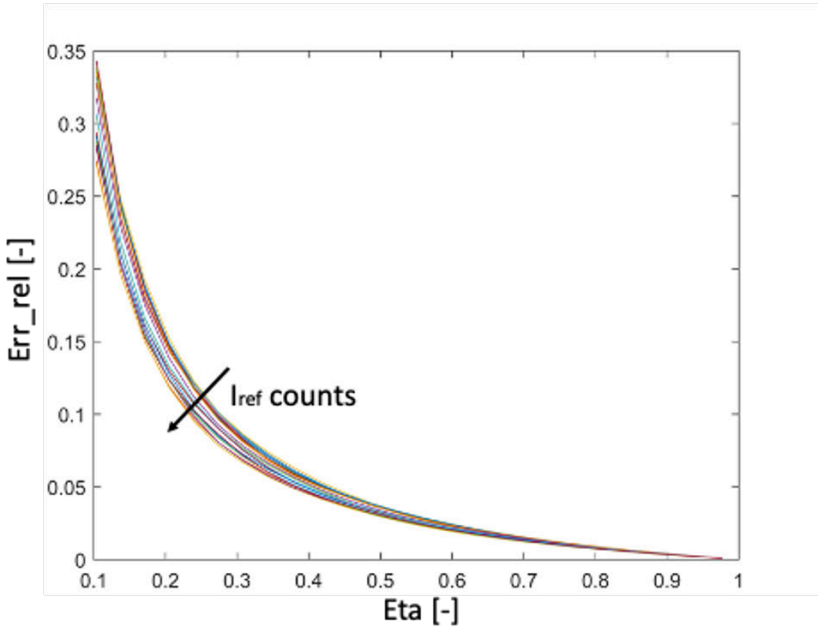

Figure 3.16: PSP uncertainty estimation by varying the I_{ref} paint emission (1250-1550 counts).

Following, using the data of Fig. 3.16, the uncertainty was calculated for each instantaneous measurement of adiabatic effectiveness on the effusion plate, being known the I_{ref} and Eta values for each pixel. The instantaneous maps of uncertainty were then combined in average terms using Eq. 3.17 and Eq. 3.18. The uncertainty analysis results of the mean adiabatic effectiveness are shown in Fig. 3.16 for the test conditions A (MFRR matching).

The uncertainty values for η mean < 0.05 were not plotted in the contours (white area). The contours are characterized by very low uncertainties, especially in correspondence with the coolant jets core trace. The calculated uncertainty increases significantly only in the outermost part of the jets structure ($\eta \approx 0.05$).

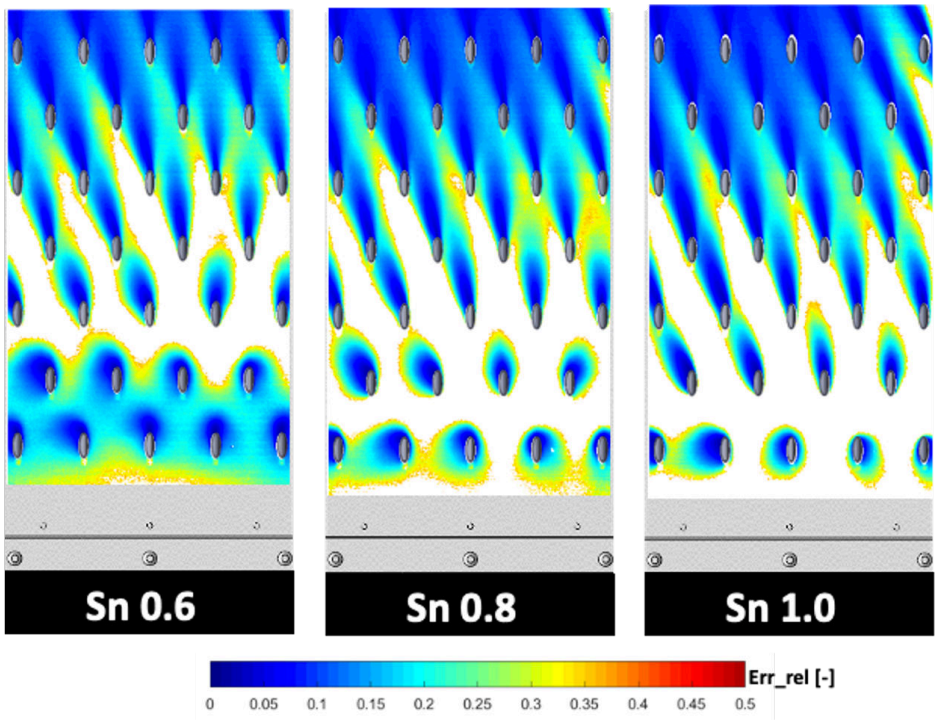

Figure 3.17: Eta uncertainty evaluation by varying the Sn, test conditions A.

Chapter 4

Flow Field Results

Contents

4.1 Main Flow

According to the final aim of this research activity, the first step of the results discussion start with the characterization of the flow field promoted by the three swirler injectors. In fact, the main flow features play a crucial role in understanding the behavior of the effusion cooling system. Initially, the results in average terms of the various survey plans (summarized in Chapter 3, Section 3.1.1) will be presented. The statistical analysis of the flow field unsteady behavior is then provided, in terms of root mean square and

turbulence values. Finally, for a complete unsteady characterization of the main flow, the Time-Resolved results are reported; these are shown in terms of instantaneous snapshots, power spectral density (PSD), and turbulence length scale (TLC) analysis. All the results concerning the main flow field were performed without coolant injection ($m_{eff} = 0$).

4.1.1 Time Average Analysis

To start, it should be remembered that all the three injectors work with the same feeding pressure drop and different mass-flow rates, due to the different discharge coefficients, as summarized in Chapter2. The reference case is the one with Sn=0.8 used to present, in a general way, the main features of the main flow field. Starting from this case, the differences promoted by the Sn variation will be highlighted through the results obtained with the injectors characterized by Sn=0.6 and Sn=1.0.

Focusing the attention to the symmetry (XY-ZX) plane, all the classical features of a swirling flow field are recognized in Fig. 4.1 and highlighted with letters for the reference case. In A, it can be observed the common shape of the annular swirler jet, characterized by high velocity and the inner shear layer (ISL) and outer shear layers (OSL). The shear layers affect very narrow regions and are therefore characterized by strong velocity gradients. All the swirlers have a Sn above the critical value (Sn=0.6) indicated by Lucca-Negro and O'Doherty [4]; as expected, all the flow field are characterized by a typical vortex breakdown with a large inner central recirculation zone (IRZ) marked with B and characterized by low-velocity values with negative direction. The vortex breakdown and the chamber wall confinement promote the onset of the outer recirculation zone (ORZ) with low velocity values, also called corner vortex, marked with the letter C in Fig. 4.1. The start of the IRZ is very close to the injector and not visible from the contour, which instead begins at $\approx 30mm$ from the dome wall. All along with the contour development, it is possible to see that the jet and the recirculation zone are sharply defined by a stagnation surface (D) characterized by velocity magnitude close to zero. Always referring to the reference case, it is possible to notice that the annular

main jet impinges the liner wall just before the third row (E), creating a stagnation zone. Moving away, the jet velocity decreases, and towards the end of the FoV, the jet tends to detach from the plate, defining the shape of the IRZ. The final part of the IRZ is downstream the 9th holes row and therefore is out of the FoV limit. The features presented so far show some changes by varying the Sn. As the Sn increases, as shown in Fig. 4.1, the opening angle of the jet increases significantly. Due to this effect, the impact point of the jet undergoes a downstream shift moving from Sn=1.0 to Sn=0.6. This involves a shortening of the outer recirculation zones (ORZ) for the case with Sn = 1.0 and an elongation for the case Sn=0.6. It is also important to observe that, as the angle of impact of the jet on the liner wall increases, the main jet undergoes a strong impact on the wall. In fact, the case with an Sn = 1.0 presents a more intense impact with an immediate reduction of the jet velocity. On the other hand, as the axial component of the jet increases (reduction of the Sn), the jet can slide better on the plate; it deflects and more easily moves parallel to the liner wall preserving its velocity magnitude.

Along with the ZY coordinates, measurements were carried out on two planes in correspondence with the leading edge of the cooling system first and fifth rows. In this way the flow field has been measured before and after the swirling jet impact on the liner. As can be seen in Fig. 4.2 only the bottom half of the test cell was analyzed. This still allows a complete characterization of the flow field due to the symmetry along the central XZ plane. The results are presented with a downstream view. Starting from the reference case (Sn=0.8), and looking at the first row plane, typical features are highlighted with the letters A, B, and C. It is possible to notice a very defined rotating annular structure (B) characterized by strong velocity components in the radial direction, highlighted by the vectors leaving the jet annulus, which promote the jet opening along the X direction. The core of the rotating structure (A) is characterized by low velocity values and corresponds with the IRZ. It is interesting to note what happens outside the OSL close to the walls. In the zone corresponding to the ORZ, also on the ZY plane, there is a rotative component in correspondence with the corners of the test

section of the corner vortex type (CV). This suggests, upstream of the swirler impact zone, a recirculation zone with a 3D complex development. Moving to the fifth row plane, it is possible to see that, once the impact has occurred, the rotating field includes all the plane available surface. By varying the Sn, the Sn = 1.0 case shows a greater opening of the jet and a reinforcement of corner vortex. In fact, they appear more defined and with higher velocity magnitude compared with the reference case. The case Sn=0.6 instead presents undefined complex corner vortex structures, characterized by lower velocity values, that less impact on the liner wall. Regarding the downstream plane, moving from the reference case to Sn=0.6, the homogeneity of the flow field increases while Sn=1.0 shows strong inhomogeneities with more intense velocity spots on the wall preceded by stagnation areas. This is justified by the increased radial component of this injector, which squashes the main flow against the wall.

The described complex 3D structures of the swirling flows have a great impact on the wall cooling flows. For this reason, measurements were also conducted in a plane parallel to the wall, 18mm ($\approx 3D_{\text{eff}}$) above the effusion plate, to evaluate the effective impact of the swirling flows on the liner wall. As can be seen in Fig. 4.3, starting from the reference Sn=0.8 case, the map shows a typical bowed recirculation region, outlined with a red dashed line in the velocity contour. Along this line, it is possible to observe the stagnation line (B) of the jet characterized by low velocity values. Downstream is the acceleration zone (C), characterized by a strong velocity gradient where the flow vectors are deflected with respect to the axial direction, in agreement with the rotating main flow clockwise direction. Further downstream, in correspondence with the jet detachment from the wall, as detected in the XY plane, the measured velocity drops significantly. Along this plane, a strong asymmetry and irregularity of the flow field are detected, and it will significantly affect the behavior of the effusion jets. Immediately downstream of the dome, the area characterized by complex recirculation structures (CV) is highlighted with letter A. The CV do not have a symmetrical pattern in this plane. The trends as the Sn changes are the same as those found in the

previous plans. There is a downstream shift of the impact and stagnation zone and an expansion of the ORZ (A) by decreasing the Sn.

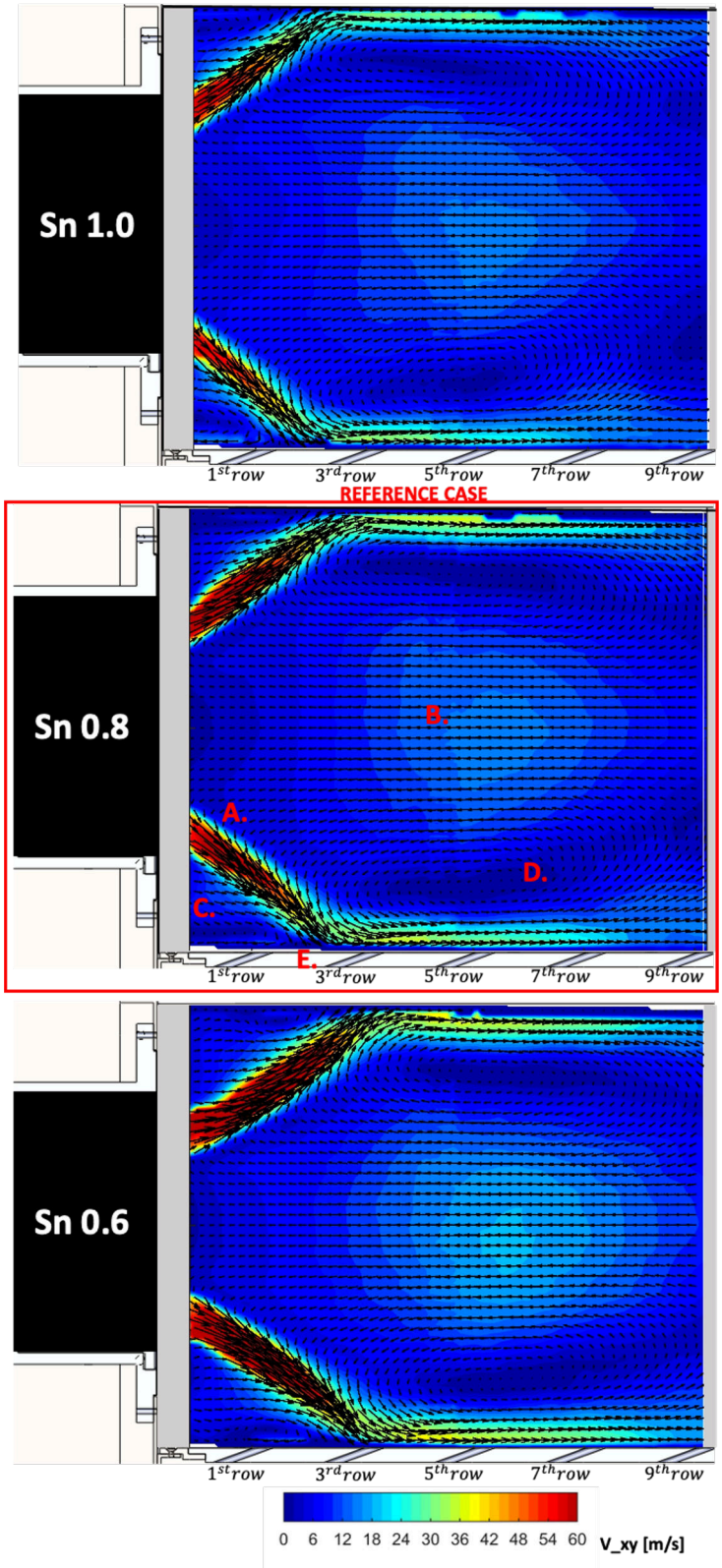

Figure 4.1: Mean Flow Field. 2D Velocity contours on symmetry plane (XY - ZX).

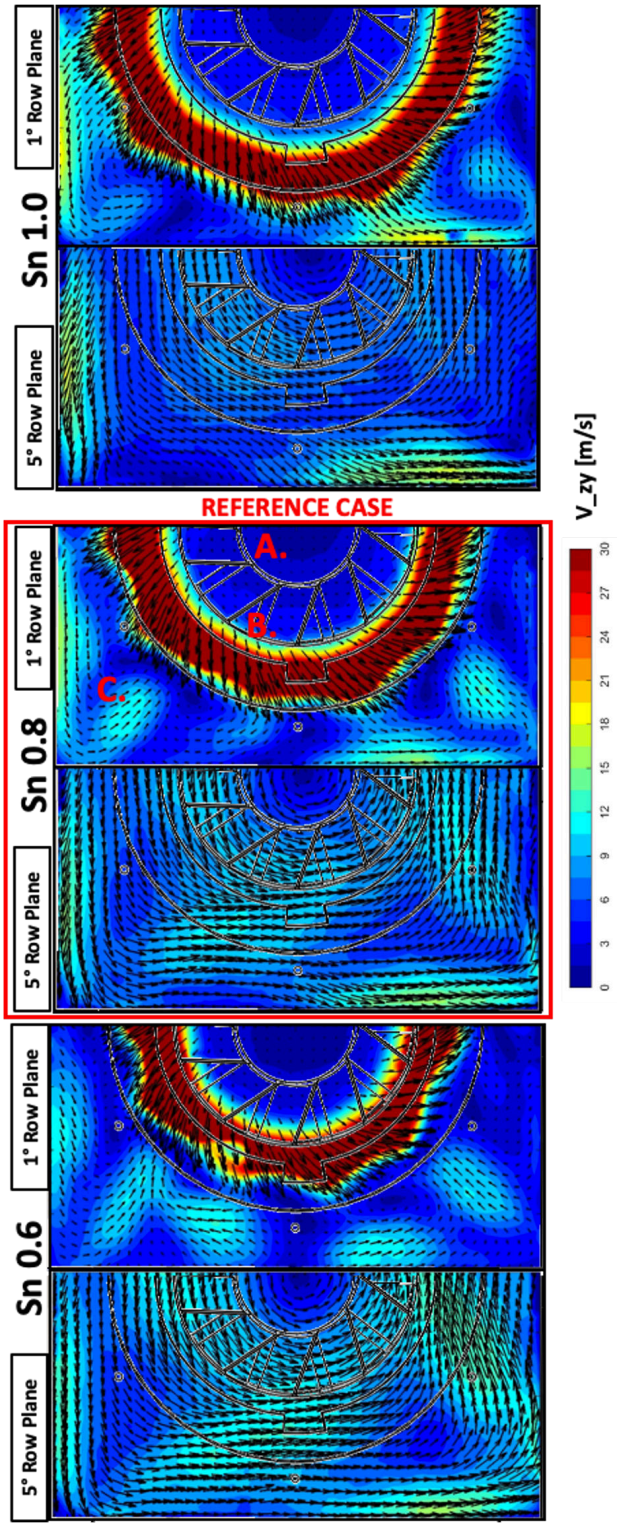

Figure 4.2: Mean Flow Field. 2D Velocity contours on ZY plane.

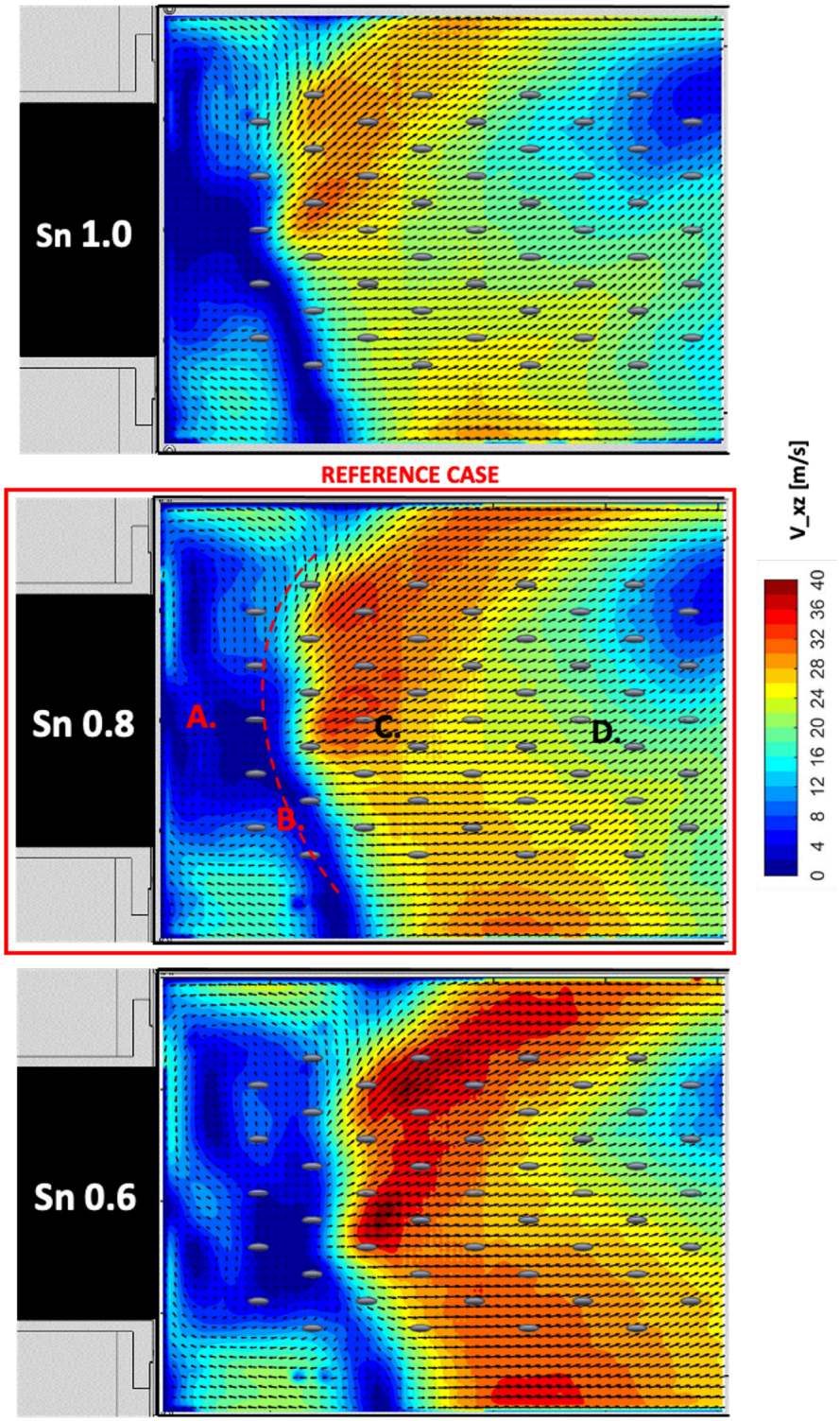

Figure 4.3: Mean Flow Field. 2D Velocity contours on XZ plane - 18mm ($\approx 3D_{\text{eff}}$) from the effusion plate.

4.1.2 Velocity Root Mean Square and Turbulence Analysis

As well known, the main flows promoted by swirler injectors are dominated by strong turbulence perturbations of many types. As a consequence, the flow mixing process is highly enhanced [71]. Turbulence acts on a large spectrum of fluctuation frequencies, and the largest turbulent scales influence the whole flow field in a way that can be strongly destabilizing for the coolant sublayer promoted by the cooling systems. For this reason a statistical characterization of the instabilities is of outstanding importance. The planes used to show the time average analysis of the mean flow are in this section studied from an unsteady point of view in statistical therms through Root Mean Square (RMS) and Turbulence intensity (Tu) 2D contours. The Root Mean Square and Turbulence values have been calculated as follow:

$$i, j = x, y, z.\ spatial\ coordinates \tag{4.1}$$

$$u_{rms} = \sqrt{\frac{1}{N}\sum_{n=1}^{N}(u' - \overline{u})^2} \tag{4.2}$$

$$RMS_{ij} = \sqrt{(u_i)^2_{rms} + (u_j)^2_{rms}} \tag{4.3}$$

$$Tu_{ij} = \frac{\sqrt{\frac{1}{2}((u_i)^2_{rms} + (u_j)^2_{rms})}}{\sqrt{(\overline{u}_i)^2 + (\overline{u}_j)^2}} \tag{4.4}$$

where $u^{'}$ and $\overline{u}$ are the instantaneous and average value of the velocity along a spatial coordinate and N the number of samples.

The statistical analyzes for the symmetry planes is reported in Fig. 4.4. The reference case shows, immediately downstream the injector, the RMS values are very high in correspondence with the inner and outer shear layer position highlighted with the words ISL and OSL. The two SL contributions are initially distinct and separated by a stable zone, representing the jet core (yellow spot), and then they merge immediately downstream. With the merging of the two SL contributions in a region called "Osc", it can be observed that the velocity oscillation values increase significantly up to a magnitude of $\approx 20m/s$. These different contributions, the two spots (ISL and OSL) connectable to the shear layers and the intense spot immediately downstream (Osc), suggest two types of instabilities that affect the swirler annular jet. The spots placed on the shear layers indicate the presence of shear layer unsteady structures (shear layer eddies) that are usually formed on the areas between a jet and the surrounding fluid domain. For what concerns the most intense spot Osc, it results form the diffusion merging of the ISL and OSL vortices contribution, and its magnified RMS values are linked to the presence of instability of the entire structure of the jet which, in this zone, begins to oscillate significantly. Downstream is possible to see how the jet impact promote a large area with RMS values of $\approx 10m/s$ characterized by strong turbulence homogeneity called in the contour homogeneous turbulence mixing zone (OTM). This zone, near the swirling jet detachment point (seventh row), as highlighted by the time-average flow field maps, finally spread over the entire height of the combustion chamber as visible in the second half of the FoV. The IRZ (in the first half of the chamber) and the ORZ, on the other hand, are characterized by low velocity oscillations. The turbulence map highlights the stagnation surface (StS) with very high turbulence values due to the velocity module, close to zero in this area. It is possible to note, observing the maps of RMS varying the Sn in Fig. 4.4, that for Sn=1.0 the ISL and OSL eddies contributions quickly merge near the swirler outlet section. This is due to a more pronounced unstable oscillatory behavior of the main jet, which is evidently triggered immediately exiting the swirler injector. On the contrary, in accordance with this trend, the contributions of the shear layer vortices for the case Sn=0.6 are more defined and

pronounced, synonymous with greater jet stability. The turbulence contours also confirm this. Both the regions near the wall, upstream and downstream the impinging region of the swirling jet, show higher turbulence values increasing the Sn. The same behavior is also recorded for the IRZ. This is in accordance with the fact that the greater is the Sn, the greater is the entity of recirculation in the combustion chamber.

Fig. 4.5 shows the statistical results for the ZY plane. A central area with low RMS values is recognized along the first row plane, corresponding to the IRZ. The core of the annular jet, characterized by large velocity oscillations, is visible moving away from the center for all the Sn cases. The shear layer vorticity contributions are not superimposed on those of the oscillation of the annulus jet only for the cases Sn=0.8 and 0.6 also on this plane, where a ring with lower RMS values is present in the core of the jet. Finally, in the proximity of the wall, in correspondence with the ORZ, the velocity fluctuations are reduced due to the lower velocity magnitude of the flow field. In general, as evidenced both by the RMS and Tu contours, the instability of the jet increases with the Sn. In this case, not only in relative terms (Tu) but also in absolute terms (RMS). Moving to the fifth row plane the RMS maps show, in this case, a good homogeneity. In fact, this plane is in correspondence with the OTMZ previously analyzed. In this case, an increase of Tu and RMS is measured as the Sn decreases. This trend is justified by what was previously verified: the effect of the impact on the liner wall is more destructive for Sn=1.0. Therefore, Sn=0.6 still retains a larger amount of turbulent kinetic energy at this distance from the injector.

Moving close to the wall in the ZX plane, Fig. 4.6 shows for the reference case a significant increase of the RMS values in correspondence with the impact zone (second row of holes). Moving instead towards down or upstream the impact zone, there is a good RMS values homogeneity for all the Sn cases. This is also confirmed by the Tu contours, which appear similar. Only the stagnation region, which presents a red spot with very high turbulence values, undergoes a longitudinal shift in agreement with the jet impact point

location, which varies with the Sn parameter.

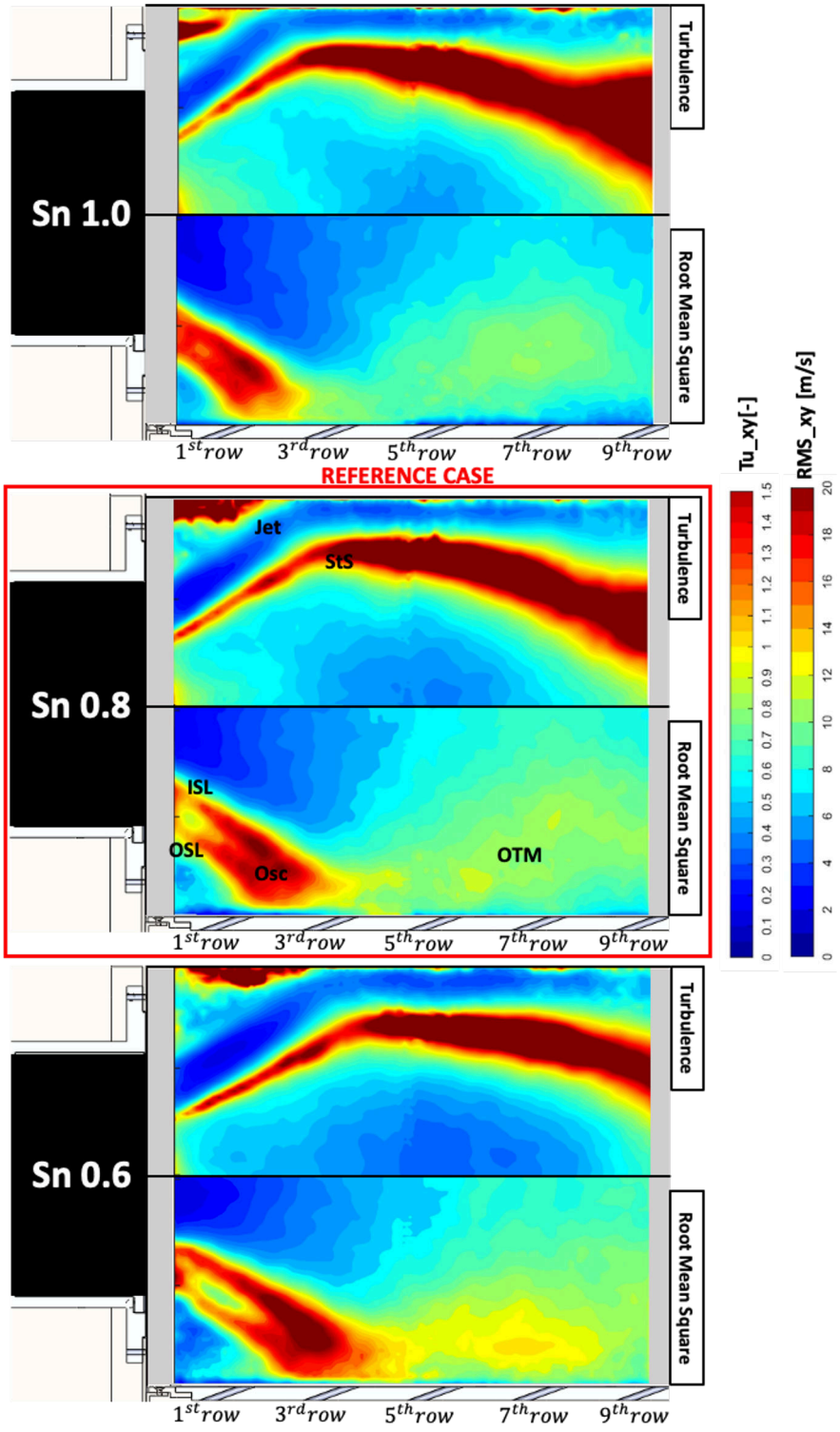

Figure 4.4: Mean Flow Field. 2D RMS and Turbulence contours on symmetry plane (XY - ZX).

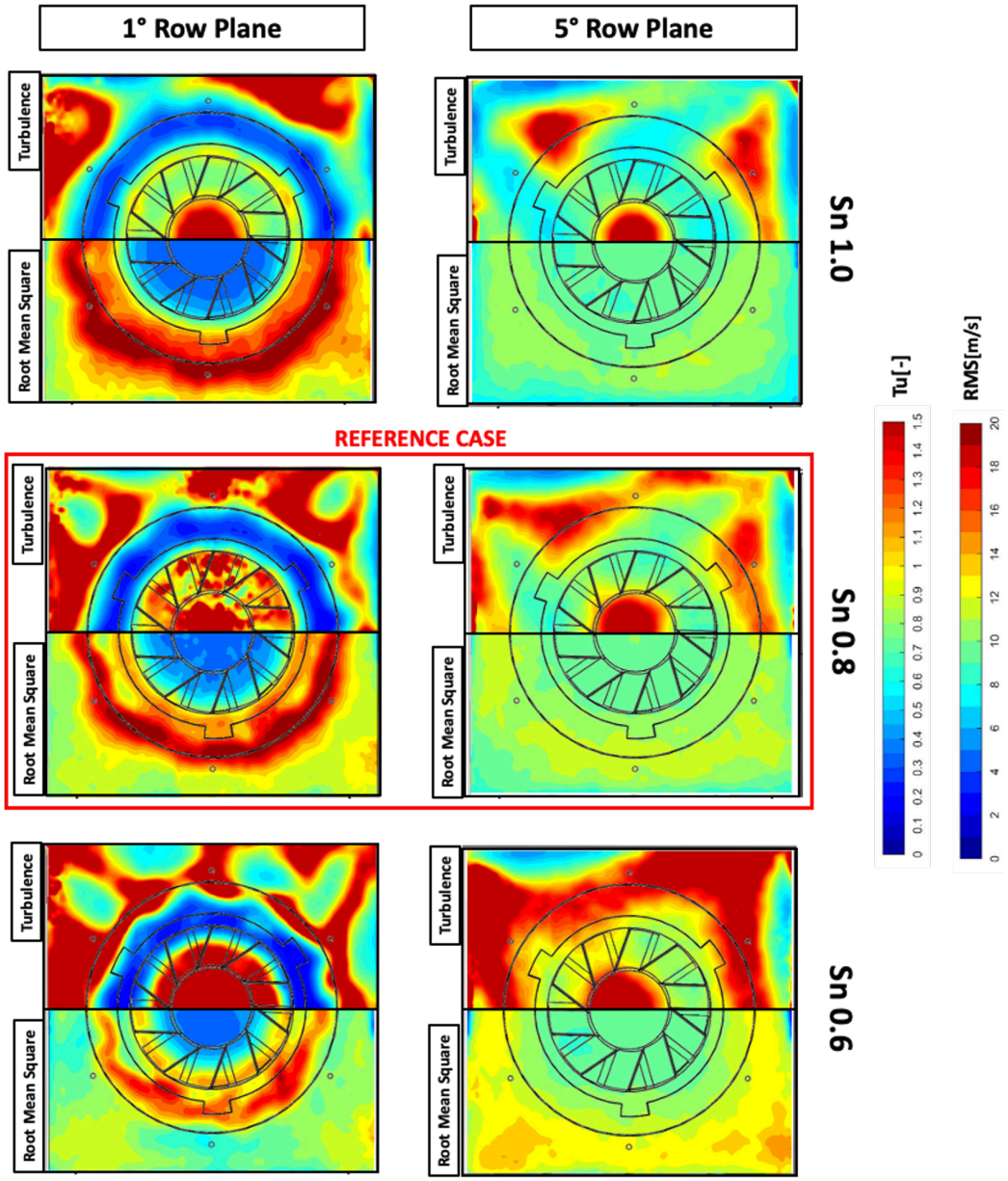

Figure 4.5: Mean Flow Field. 2D RMS and Turbulence contours on ZY plane.

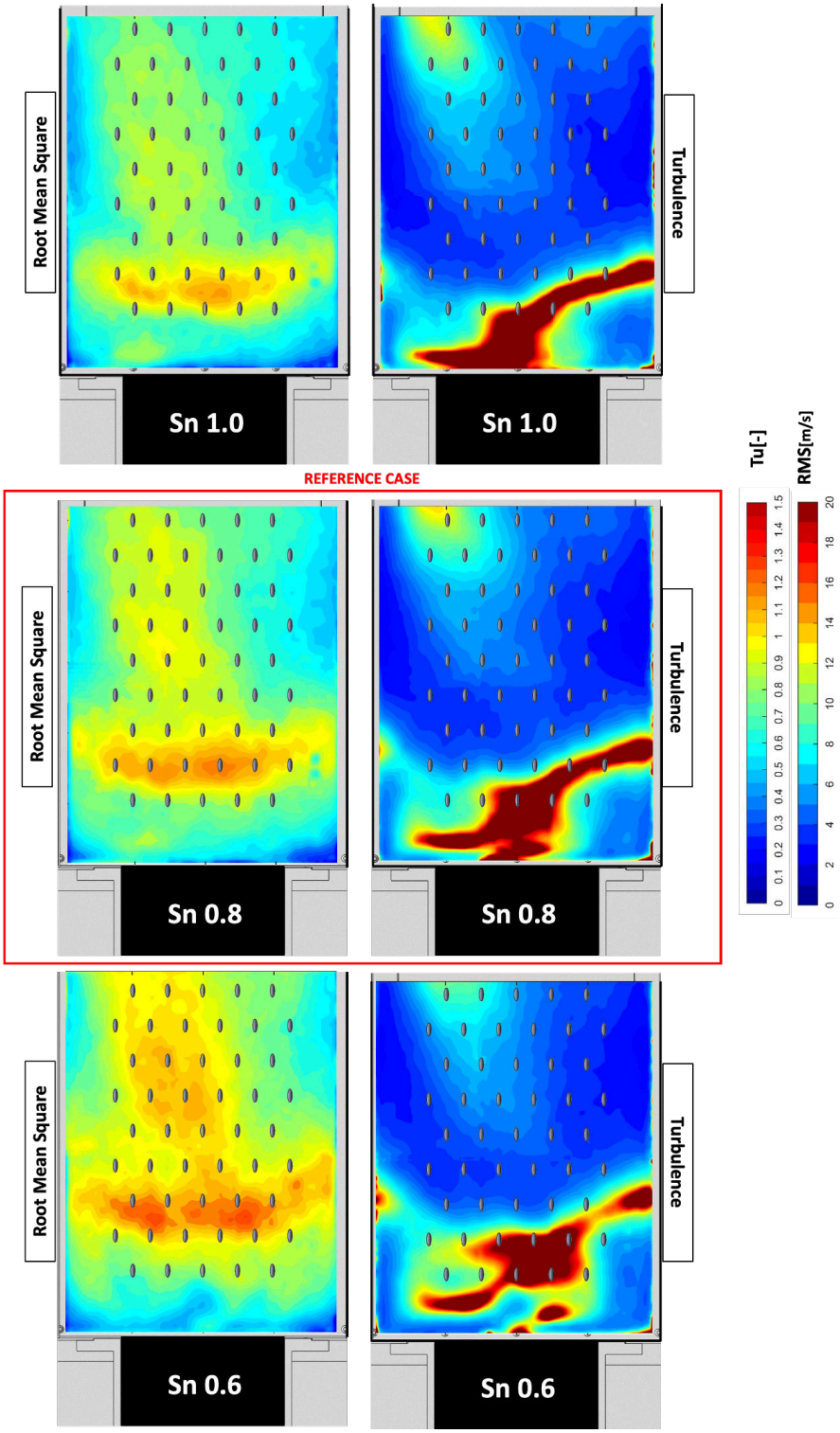

Figure 4.6: Mean Flow Field. 2D RMS and Turbulence contours on ZX plane.

4.1.3 Time-Resolved and High-Frequency Analysis

As previously stated, for a complete characterization of the main flow, a high-frequency analysis is necessary. Specifically, instantaneous snapshots of the flow field in Time-Resolved mode (2000 Hz) allowing an effective understanding of the unsteady phenomena that occur in the test model and justifing the RMS values previously shown. Following, by increasing further the acquisition frequency (5000 Hz), a power spectral density (PSD) and turbulence length scale (TLS) analysis was performed. These last measurements give a quantitative, and not just phenomenological, characterization of the unsteady structures identified with the time-resolved snapshots. Fig. 4.7 shows where these measurements were carried out. Along the XY symmetry plane, two FoVs have been identified. The first, the red one, made it possible to study a large portion of the main jet and the interaction with the liner wall for the dedicated time-resolved analysis (with a sampling frequency of 2000 Hz). For the analyzes in higher frequency (PSD and TLS), on the other hand, a sub-window (black in the figure) was used to acquire (with a sampling frequency of 5000 Hz) the PIV images. As shown in the sketch, the TLS measurements took place over the entire surface of the FoV, while the PSD measurements were made in points located in the ISL of the jets, where the shear layer instabilities occur.

Fig. 4.8 shows an instantaneous flow field vectors snapshot of the reference case Sn=0.8, but the phenomena that occur describe the behavior of the other injectors as well. It is possible to observe the onset of eddies in the ISL (red) and OSL (green) in counter-clockwise and clockwise directions, respectively. These instabilities generally appear in the external structure of the annular jets and contribute to the high RMS values analyzed and described in the previous section. In the impact zone, the swirling jet promotes a stagnation point with positive and negative direction of the velocity in the X direction. In this region, it is still possible to observe that the eddies preserve their structure and continue to slide along the liner wall surface. Those of the OSL in green, in average terms, will contribute to the formation of the ORZ. Fig. 4.9 shows the temporal evolution of the SL instabilities and the oscillatory-fluctuating behavior of the annular jet, which was previously

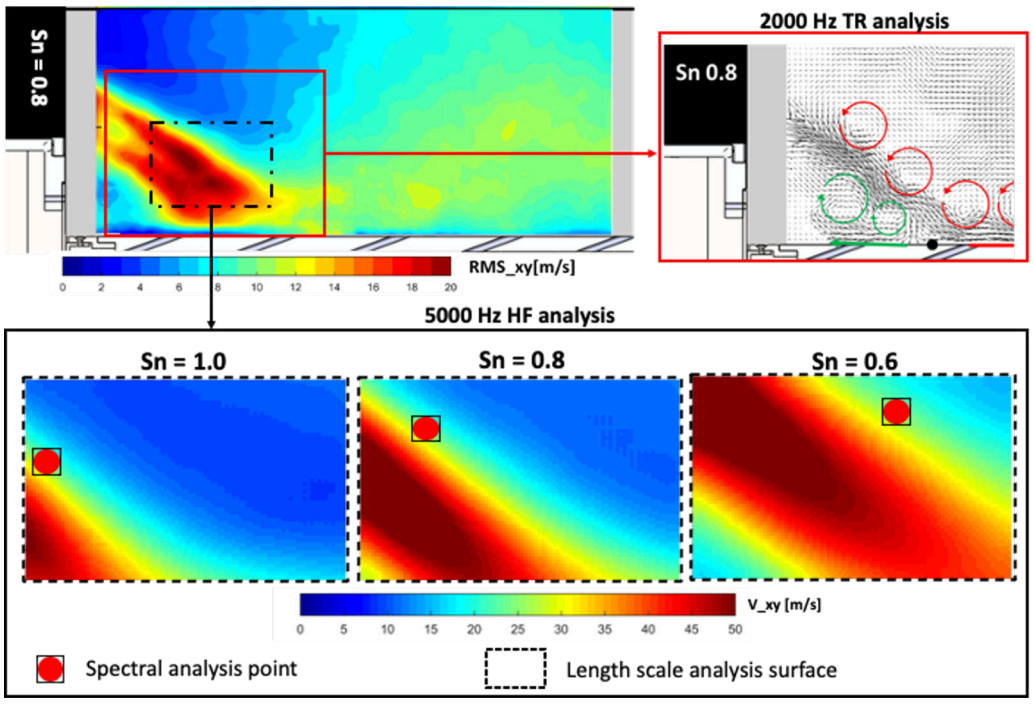

Figure 4.7: Explanatory sketch of the high frequency measurements carried out on the main flows (symmetry XY plane).

supposed during the RMS-Tu analysis.

The results are shown with a sample-rate halved compared to the acquisition frequency. In $t1$, it is possible to observe, highlighted in red and with the number 1, a first vortex arranged on the ISL. In the next snapshot, it is transported by convection by the jet while another vortex (2) appears further upstream. Following t5 = 0.004sec, it is possible to observe that when vortex 1 approaches the wall, it starts a degradation-decay process, and its structure is no longer well defined. In all the time-resolved snapshots instabilities evolution, it is possible to note for the ISL eddies a defined spatial and temporal coherence of appearance. In the meantime, starting from t = 0.002, on the OSL, anti-clockwise vortices were transported in a more disordered and less regular way. The wall confinement of the outer shear layer makes these instabilities more chaotic and less regular. Another unsteady

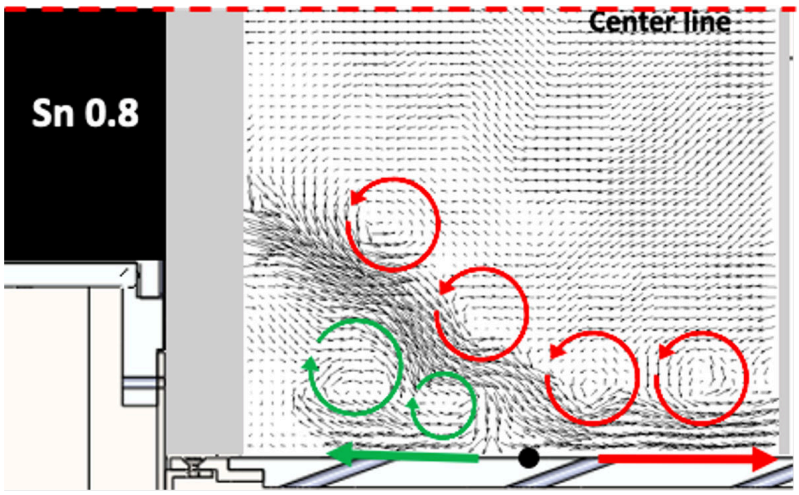

Figure 4.8: Instantaneous vector map with evidence of ISL (red) and OSL (green) instabilities.

phenomenon that occurs in the velocity vector maps is represented by the strong fluctuations of the jet, especially close to the wall. Over the entire image time series, shown in Fig. 4.9, the jet presents a not defined structure but an oscillatory wave arrangement. After a first more stable initial behavior, immediately exiting the injector, the jet undergoes ever wider fluctuations until it reaches the wall. Consequently, the impact point oscillates between the first and the third row; such a wide oscillation will have a strong influence on the film cooling. As previously seen with the RMS analysis, as the swirl number increases, the oscillatory mechanism is triggered earlier, immediately out of the injector due to the greater instability promoted by the higher swirl number.

A time-resolved analysis, like the one shown, therefore allows to connect the sources of instability to the RMS and Tu measured values; on the other hand, the evaluation of RMS and Tu intensity gives an idea of the average deviation of instantaneous velocity from its mean value and, therefore, of the mean kinetic energy per unit mass associated with the turbulent flow eddies. Besides that, it is also interesting to investigate how this energy is distributed among different time and spatial scales through PSD and TLS

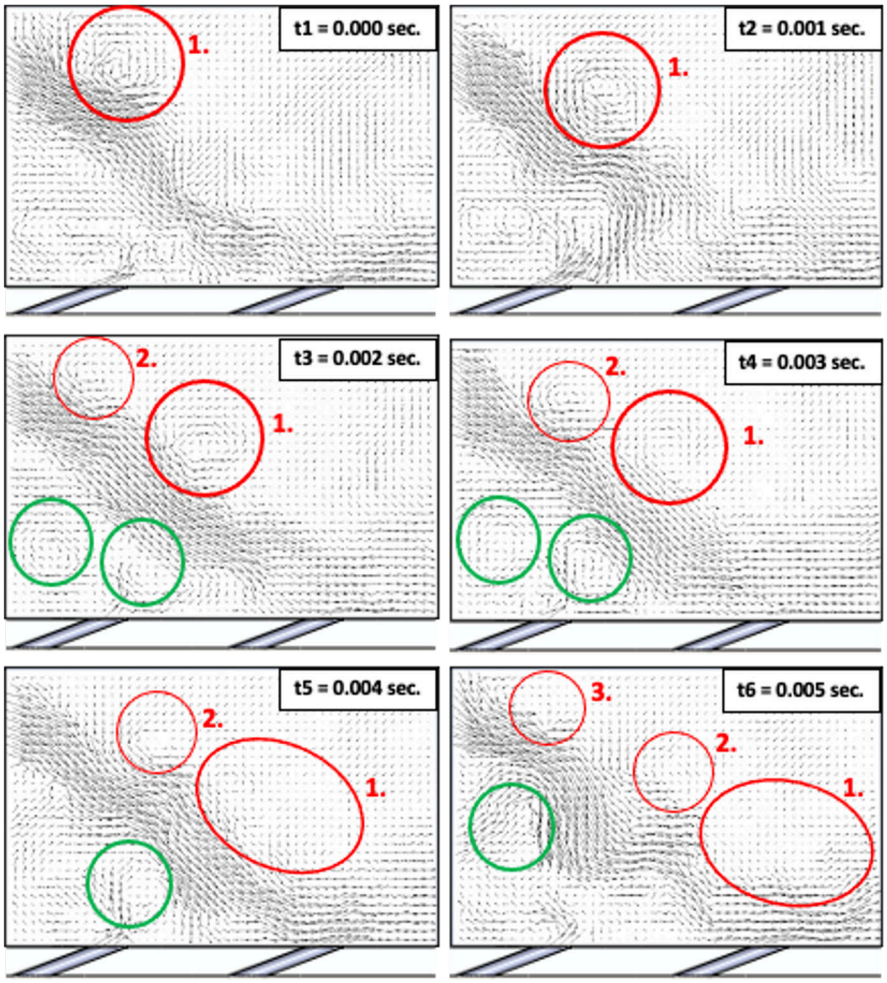

Figure 4.9: Time Resolved evolution of the SL instabilities and jet fluctuation.

analyzes. For what concern the turbulence length scale analysis, this was carried out, on the entire survey FoV, through the standard approach of signal auto-correlation [72]. The velocity values, separately along with the X and Y coordinates, were treated with the following equations:

$$i = x, y. \; spatial \; coordinates. \tag{4.5}$$

$$R(\tau) = \int_0^T u_i(t) \cdot u_i(t+\tau)\, dt \tag{4.6}$$

$$\rho(\tau) = \frac{R(\tau)}{R(0)}. \tag{4.7}$$

$$T_i = \int_0^t \rho(t)\, dt \tag{4.8}$$

$$L_i = T_i \overline{u}_i \tag{4.9}$$

These functions estimate the statistical correlation between the velocity signal and its corresponding shifted on time, as shown in Eq. 4.6, and Eq. 4.7. When the value of the autocorrelation ρ drops to zero, there is no longer any similarity between the velocity signals. This means that the values of u_i are statistically independent. To investigate how the turbulence energy is distributed among different frequency scales the Fast Fourier Transform has been applied to the two fluctuating components of velocity separately, finding their frequency spectra on a discrete number of frequencies from 0 to 2500 Hz (half of the acquisition frequency according to Nyquist-Shannon sampling theorem). Then the turbulence kinetic energy, for every frequency, has been calculated using the following relation:

$$K(f_i) = \frac{1}{2} u_i'(f_i)^2 \tag{4.10}$$

where f_i is a frequency value between 0 and 2500 Hz.

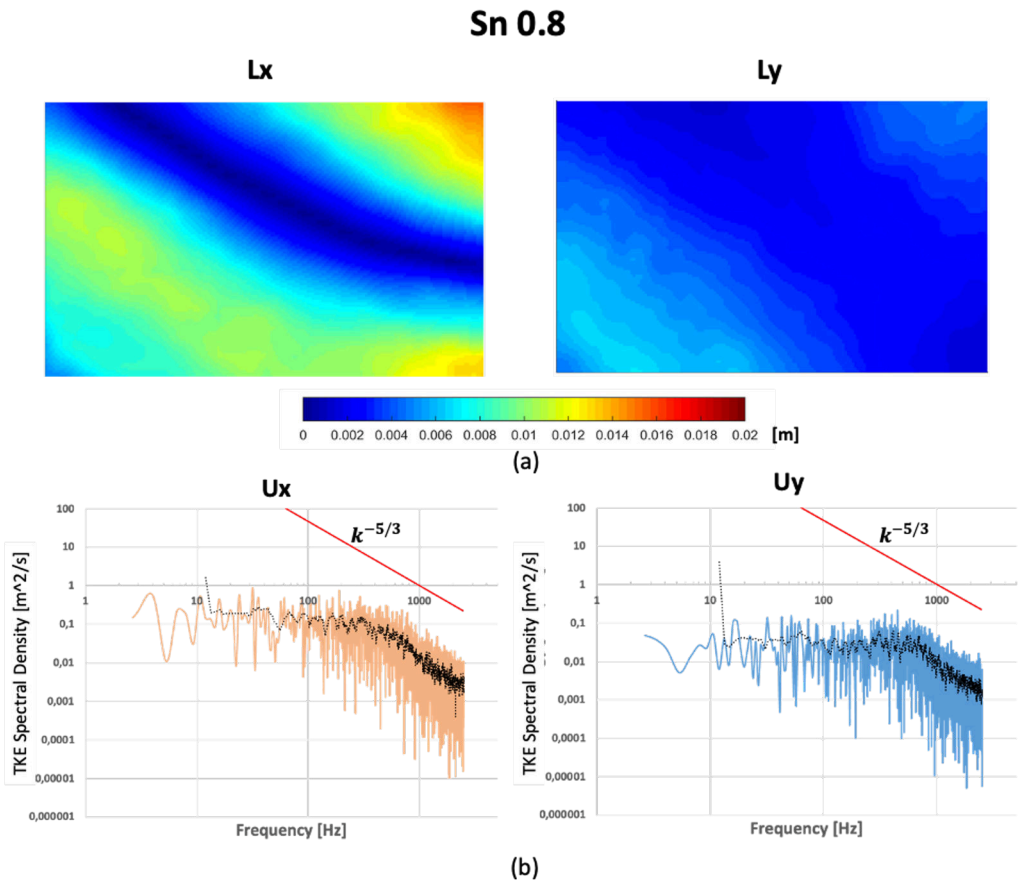

Figure 4.10: Sn = 0.8. Turbulence Length Scale (a) and Power Spectral Density (b) analyzes.

The results of these analyzes are reported in Fig. 4.10 for the reference case Sn=08. On the top of Fig. 4.10(a), the contributions of the turbulence length scale analysis are shown for the FoV taken into account (Fig. 4.7). The main jet SL is characterized by 11-12mm oscillations along the x axis and about 8mm along the y axis. The blu spot in the Lx contour, with values close to zero, corresponds to the stagnation surface where $\overline{u}$ is ≈ 0. These results are in full agreement with what can be measured by instant snapshots where the detected instabilities have about this magnitude. The frequency spectra on the bottom (b) present the results in terms of power

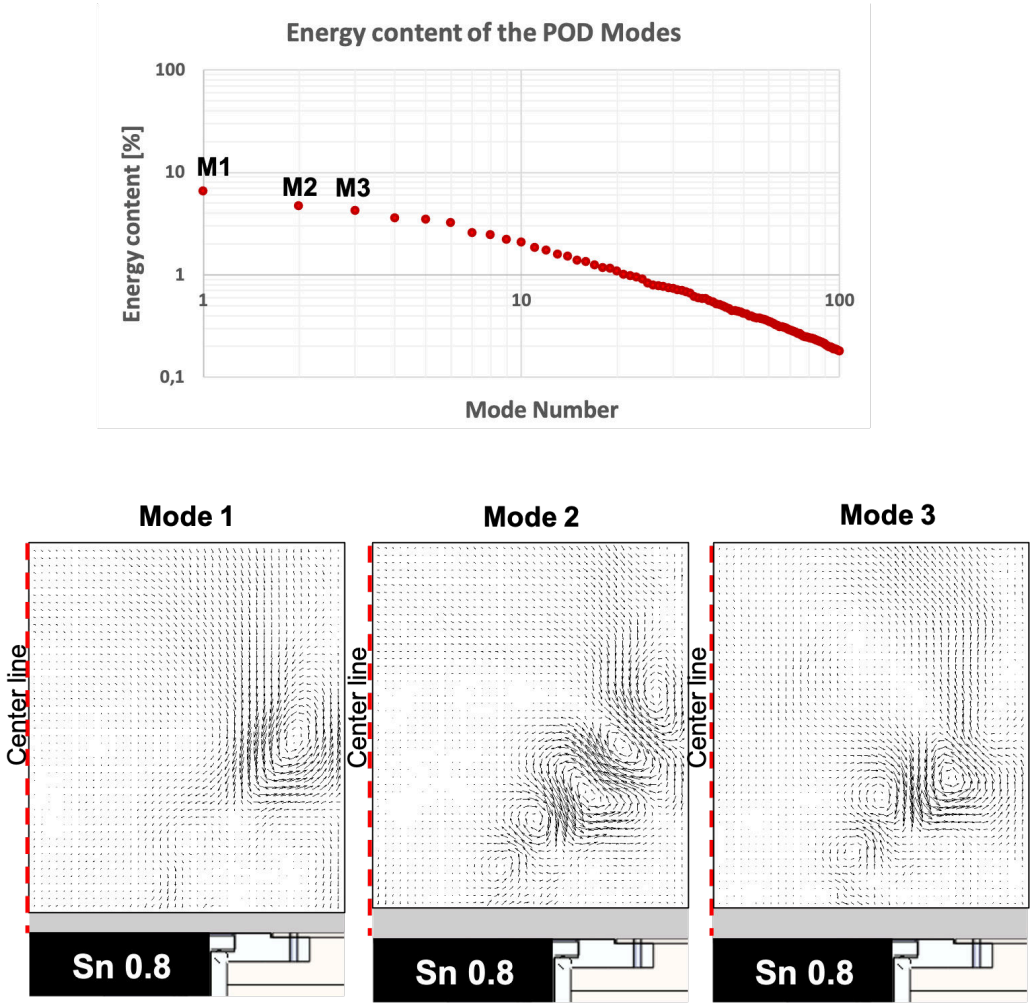

Figure 4.11: Top: relative energy of POD eigenvalues. Bottom: spatial distribution of the first three POD modes.

spectral density in the measurements point highlighted in Fig. 4.7. The raw results are in orange (x direction) and blu (y direction), while in black is a smoothed average line in steps of 10Hz in order to have a clear view of their trend. The variable on the y-axis is the spectral density $E(f_i) = K(f_i)df$, where df is the resolution step on the frequency axis. With such a visualization, the area under the curve between two frequencies f_1 and f_2 represents the turbulent kinetic energy (K) content of the flow field within

these frequencies, which are inversely proportional to the size of the turbulent eddies in the flow (i.e. to the turbulence scales) with TKE progressively decreasing as the turbulent frequency is increased (i.e. as the length scale decreases). A first energy content range is clearly visible along with both directions and represented by the first part of the spectrum, which appears quite flat. Following there is the energy decay range where the TKE is passed to ever lower turbulent scales. For both spectrums, the decay range starts approximatively between 300 - 500 Hz. A curve with a $k^{-5/3}$ slope is also reported to compare the measured trend with the one obtained from the Kolmogorov turbulence subrange theory [73]. According to the turbulence length scale analysis and the preferential direction of the flow (x direction), the energy content along the x axis, at the conservative scales, is greater than that along the y axis. Furthermore, the total part of the turbulence kinetic energy, measured in the proximity of the main jet, does not present unsteady structures with specific narrow frequency. Therefore, the eddies and the fluctuations that occur in the annular swirling jet have a coherent structure and behavior, as shown by the time-resolved analysis. However, they do not have a characteristic frequency (they are not time coherent). This is also confirmed by a Proper Orthogonal Decomposition analysis carried out for the reference case Sn = 08. The analysis was performed using the PIV snapshots acquired at 5Hz along the XY symmetry plane of the test rig (Tab. 3.1). The results are shown in Fig. 4.11 and explain that the first 3 detected modes have low energy contents. The first mode suggests the contribution of OSL vorticities, which in average terms contribute to the formation of the ORZ. The estimated energy content is about the 6.5% of total. The second and third Modes present similar energy contents and represent the ISL instabilities. The following modes are very similar to Mod3, and Mod4. However, it can be noted that their energy content is very low: Mod2 = 4.6% and Mod3 4.1%. This confirms the PSD analysis previously shown: time-coherent structures with a characteristic frequency to which a strong energy content can be associated are not detectable. The energy content of the jet, characterized by large speed oscillations, is therefore spread over the entire frequency range. It is possible to conclude that the swirler injector induces

strong broadband unsteadiness of the flow field. Fig. 4.12 show the TLS and PSD results obtained for the other two cases (Sn=1.0 on the top and Sn=0.6 on the bottom). The spectra (b) for both injectors present a total agreement with the reference case. Also for these injectors, the unsteady structures connected to the main jets did not show a characteristic frequency, and the decay range starts approximatively between 300 - 500 Hz. The most marked difference is in the amount of TKE that is contained in the spectra along with the two spatial coordinates. For Sn10, the PSDs are very similar in the two directions of space due to the greater jet inclination, which has an exit angle from the injector close to 45°. On the other hand, for the case at Sn=0.6, the TKE, in coherence with the jet direction, is contained more along the x axis which in the preferential direction of the jet. The measured TLS values show an increase in length scale as the Sn decreases. In fact, the Sn=0.6 has a larger axial velocity component that prompts larger oscillation in X direction. Sn=1.0 presents Lx=8-10mm and Ly = 6 mm while Sn06 Lx = 20mm and Ly = 10mm. The trend is justified by the higher axial component direction of the flow field promoted by lower Sn. Furthermore, it must be considered that greater mass flow rates are present with lower Sn due to the different injector effective area. For this reason, in correspondence with the analyzed FoV, Sn=0.6 is characterized by higher velocity values with respect to the other injectors.

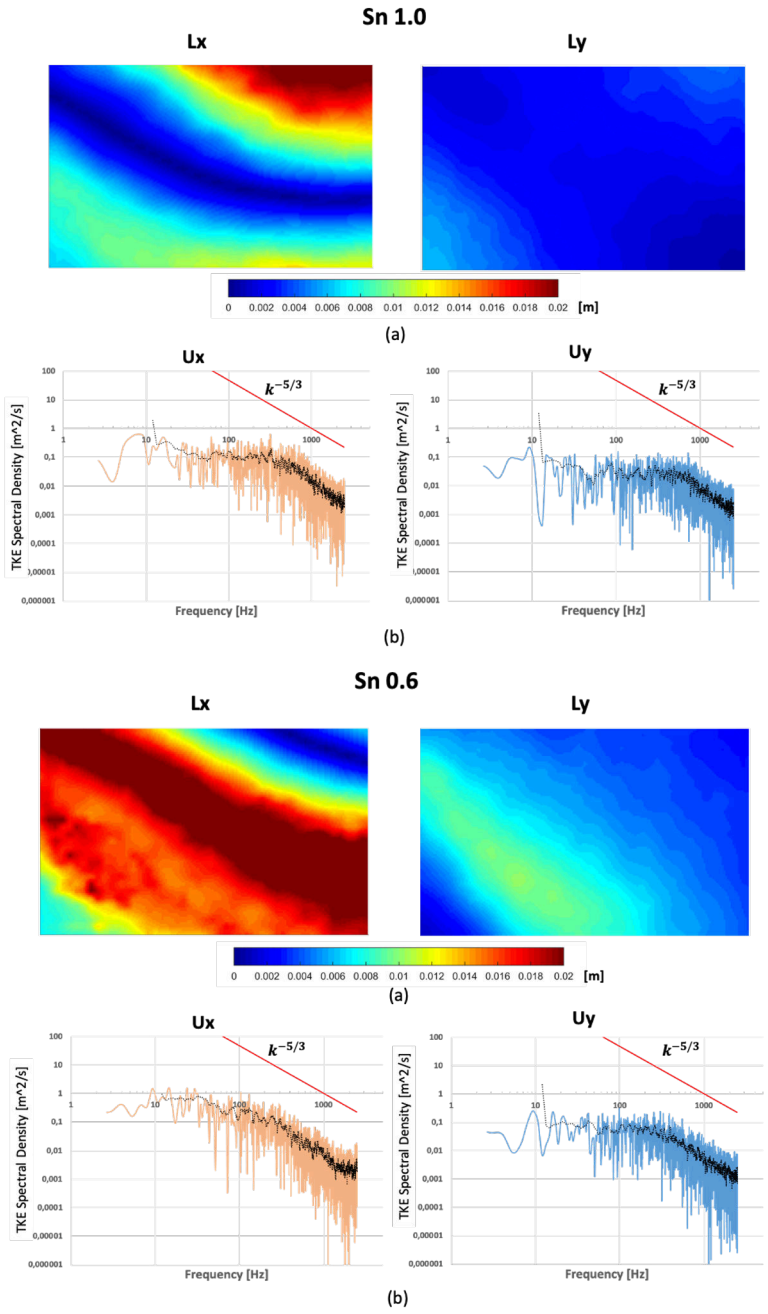

Figure 4.12: Sn=1.0 (top) and Sn = 0.6 (bottom). Turbulence Length Scale (a) and Power Spectral Density (b) analyzes.

4.2 Effusion Flow

The results of the flow field of the coolant layer are presented in this section. They are initially presented in average terms. A characterization of the principal unsteady measured phenomena follows: the jets oscillations, promoted by the main flow instabilities, and an analysis of the Khelvin-Helmholtz eddies. These unsteady mechanisms increase the mixing between main and coolant flow, and a characterization is therefore necessary. Finally, the various instability sources will be summarized in RMS and Tu contours to quantify their magnitude. The results are presented for the reference Sn=0.8 case by varying the effusion system feeding pressure drop ($\Delta p/p_{\text{eff}}$). After, the characterization move to a comparison by varying the Sn parameter (Sn=0.8, Sn=1.0, Sn=0.6) for both the proposed test condition shown in Chapter 2, Section 2.2:

- Test conditions A: matching $\text{m}_{\text{Coolant}}/\text{m}_{\text{Main}}$ by varying the Sn.
- Test conditions B: imposing $\Delta p/p_{\text{eff}} = 3\%$ by varying the Sn.

4.2.1 Time Average Analysis

Fig. 4.13 shows the flow field for the reference case: Sn=08 ($\Delta p/p_{\text{eff}}$= 3%). The measured FoV is on the XY symmetry plane of the test cell. It is possible to asses that the swirling main flow extremely influences the coolant jets behavior. The main jet hits the plate near the 3rd row with a velocity magnitude even higher than 40 m/s, influencing the coolant sub-layer structure in terms of jet trajectories deviation. Enlarged windows, with vector maps to better understand fluid dynamics, are shown in the bottom part of Fig. 4.13.

The 1st row jet is in a reverse main flow condition in the IRZ. In fact, its trajectory appears strongly deviated upwards, completely detached from the wall. Immediately downstream the trailing edge of the hole, it is possible to observe a recirculation zone where presumably the flow coming from the injector stands persistently. The jet structure is compromised, and the jet core after about one d_{eff} from the wall in the y-direction is no longer detected.

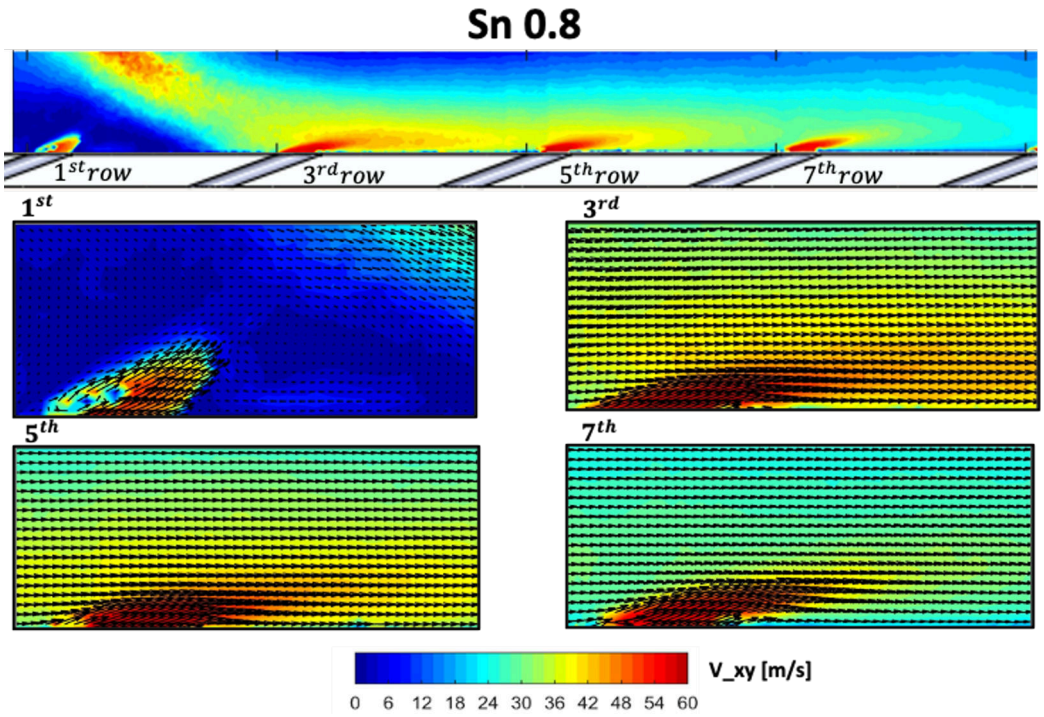

Figure 4.13: Effusion mean flow field on XY plane. Reference case: Sn=0.8, effusion $\Delta p/p = 3\%$

The 3rd jet is in correspondence with the impact and re-acceleration zone of the main flow. In correspondence with the impact and re-acceleration zone of the main flow, the jet in the 3rd row disappears in an intense velocity spot where the two contributions of the main and coolant jet to the velocity magnitude are not distinguishable and it is completely pushed against the plate.

The following jets present a behavior more similar to the classic jet in crossflow (JCF) treatment. The 5th row jet still appears with a trajectory close to the wall, while the seventh is detached from the wall, and the typical structure of the jet in crossflow is recognizable due to the high local VR value. Measurements were also carried out for $\Delta p/p_{\text{eff}} = 2{,}1\%$ to estimate the effect of the feeding pressure drop parameter. As shown in Fig. 4.14, as the $\Delta p/p_{\text{eff}}$ decreases, the effect of the swirling flow on the jets increases.

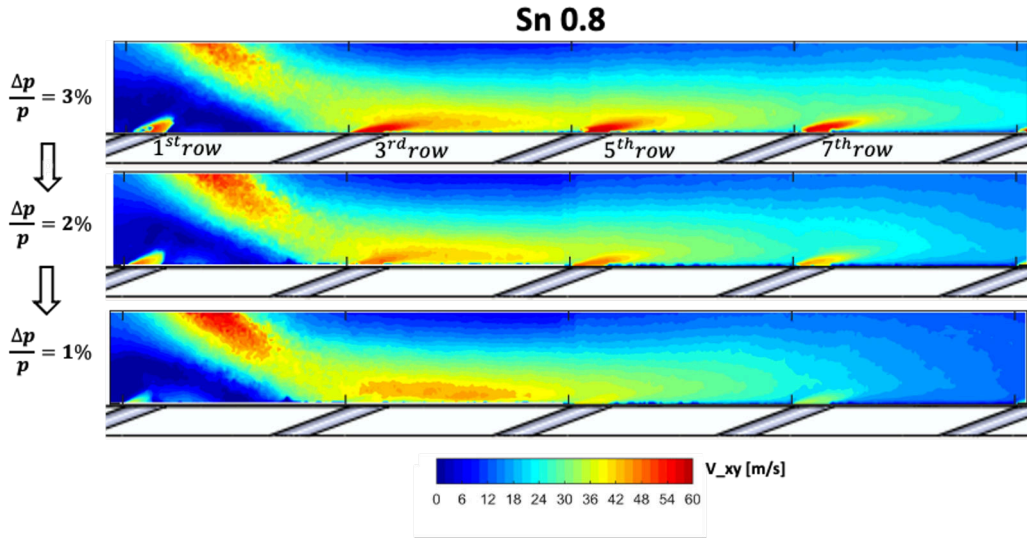

Figure 4.14: Effusion mean flow field on XY plane. Reference case: Sn=0.8, effusion $\Delta p/p$ = 3,2,1%)

The peculiar behavior, previously shown, of each hole is thus amplified. This depends on a global decreasing of the jet momentum (and VR): the jets lose their kinetic energy, and more easily, they are arranged according to the main flow streamlines. In fact, reducing the pressure drop to 2%, the first hole has an even more compromised structure, and all the others show a trajectory deflection to the wall promoted by the swirling main flow. Only the 5th and 7th jets still have a coherent structure. For the test $\Delta p/p_{\text{eff}}$=1%, the jets momentum is not sufficient to preserve their structure. For this test case, due to the lower VR values, the holes appear in addition mass flow rate regime. Fig. 4.13 shows the effusion flow field results by varying the Sn for both the test conditions. It can be observed, for the test conditions A that, as the Sn increases (Sn=1.0), the coolant jets undergo mainly the trajectory deflection effect of the swirling main flow. In particular, the core of the 1st row jet is brought out of the symmetry plane, and it is barely visible in the contour. The 3rd row jet appears more compressed to the wall respect the reference case. From the fifth row, however, the behavior of the jets appears

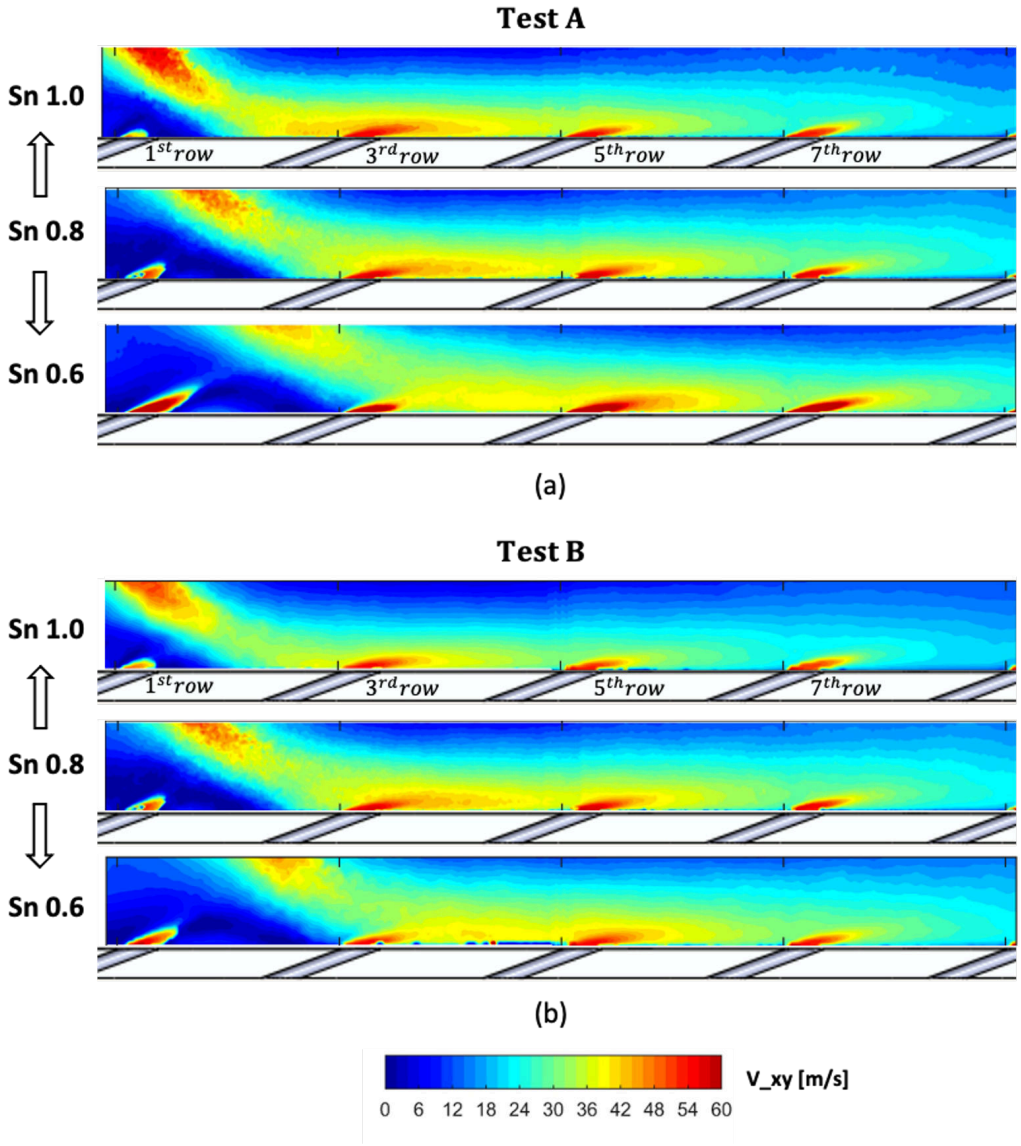

Figure 4.15: Effusion mean flow field on XY plane. Sn effect for Test Conditions A and B.

similar to the reference case. The independence of the jets trajectory on the coolant sub-layer increase in the Sn=0.6 test. The first hole has a defined structure, and the others have greater penetration capacity. The results of the test conditions B show more similar velocity coolant sub-layer patterns

by varying the Sn. Each jet appears similar in velocity magnitude and shape terms by varying the Sn. The 7th row jet appears practically identical in terms of velocity and trajectory for each Sn case. Therefore it is possible to conclude that, matching the effusion feeding pressure drop, the benefits in terms of jets stability that a lower Sn produced are canceled due to the mass flow rate ratio ($m_{Coolant}/m_{Main}$) variation. In fact, as shown in Table 2.2 (Section2.2), the mass flow rate ratio increases with the swirl number for test conditions B.

The time-averaged measurements were also carried out along the ZY planes in correspondence with the trailing edge of the following holes rows: 1^{st}, 3^{rd}, 5^{th}, 7^{th}. Only the measurements functional to the characterization of the main-coolant interaction are reported to summarize the results obtained. The velocity contours of the main flow field previously reported in Fig. 4.2 and Fig. 4.3 are particularly useful for understanding the jets behavior along these planes.

Fig. 4.16 illustrates the flow field measured along with the 1st, 3rd, and 5th row for the Sn=08 $\Delta p/p_{eff3\%}$ reference case. In the figure, for a better understanding, there are zooms to capture the fluid dynamic structure of each jet using vector maps. As previously shown, the 1st row is in the IRZ, the 3rd one immediately downstream the swirling jet impact zone, and the fifth one in the main jet deceleration zone. In fact, the measurements present different velocity patterns and hole structures by varying the rows and the position of the holes. The jets core appears in the contours as a higher velocity spot near the holes outlet. As highlighted by the red arrows, all the jets in the 1st row undergo an upward rise and an outward dragging in the z direction. The outward dragging is more intense for the holes Sz+1 and Sz+2 positions compared to Sz-1 and Sz-2. This is in accordance with the previously shown velocity maps of the mainstream in figure4.2.

In fact, in correspondence with this plane, the annulus jet has not yet impacted the liner, and the recirculation zone presents two velocity spots that move externally from the centerline of the plate and create the Corner Vortex zone. The one on the right is more intense, and the jets core show a stronger drag in this area. Another peculiarity is the absence, as visible

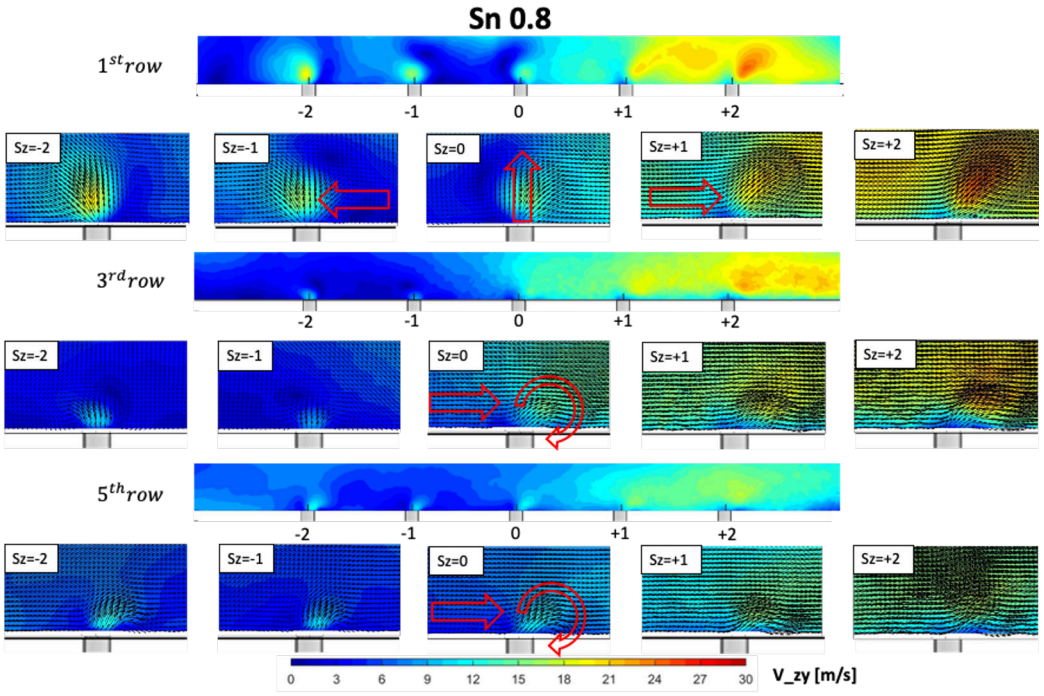

Figure 4.16: Effusion mean flow field on ZY planes. Reference case: Sn=0.8, effusion $\Delta p/p$=3%

on the zoomed vector maps, of the Counter-Rotating Vortex Pair structures. In the vector maps shown, only the hole of the 3$^{\text{rd}}$row Sz-1 has a clearly identifiable one. In the presence of aggressive swirling main flow, the CRVP structures are not clearly identifiable at the hole exit for the examined rows. As can be seen, the absence of CRVP is replaced by a single structure rotating in the counterclockwise direction in accordance with the positive direction of the x-axis (the view of the contour is from downstream to upstream) and highlighted with a circular red arrow. As highlighted by the straight red arrows, from the 3rd row, after the main flow impact, all the holes are deflected in accordance with the main flow rotating direction.

Fig. 4.17 shows the $\Delta p/p_{\text{eff}}$ effect on the behavior of the jets for the first and fifth row of holes. Also in this case, the loss of the jet momentum promoted by the $\Delta p/p_{\text{eff}}$ reduction increases the influence of the rotating

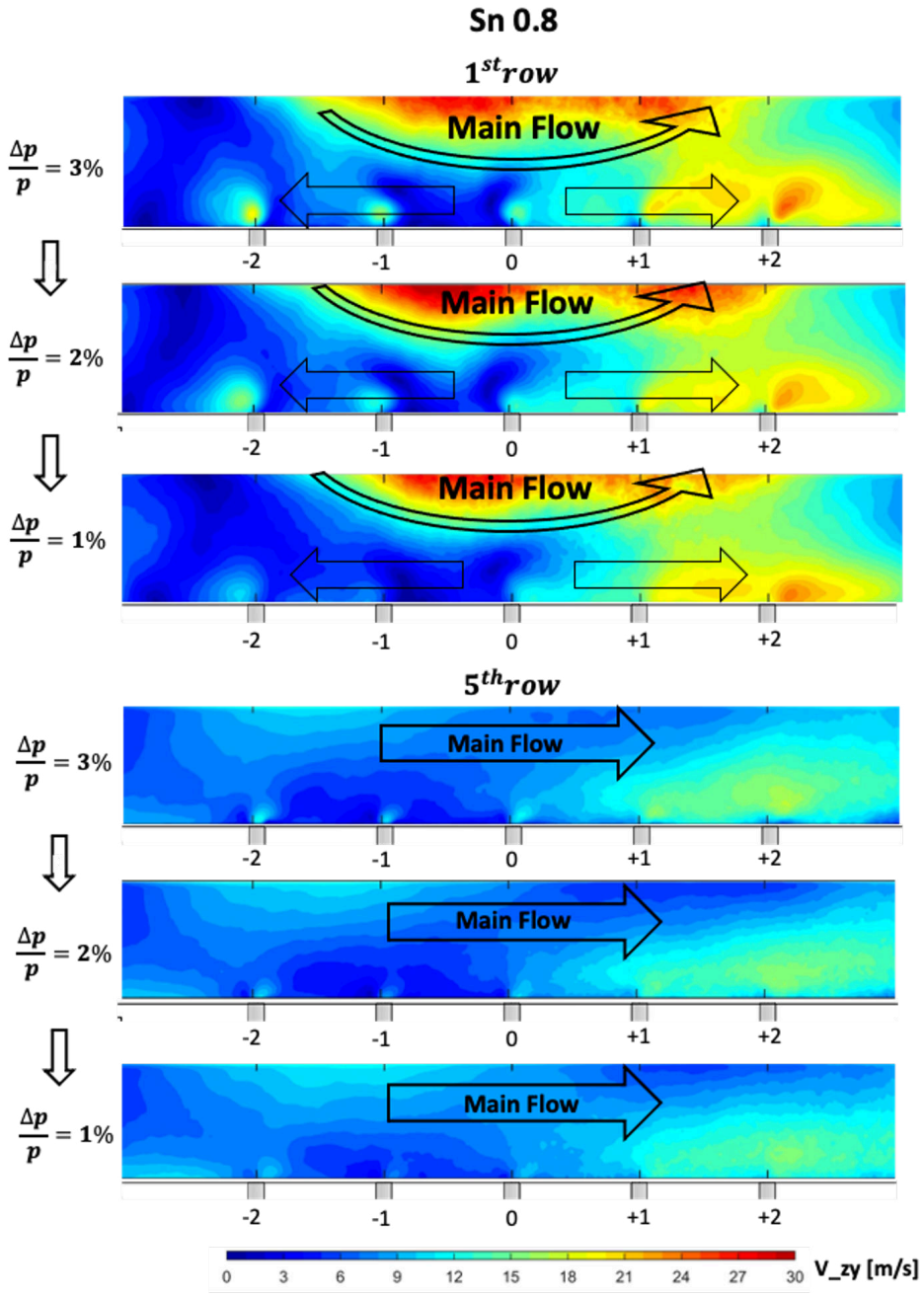

Figure 4.17: Effusion mean flow field on ZY planes. Reference case: Sn=0.8, effusion $\Delta p/p$=3,2,1%)

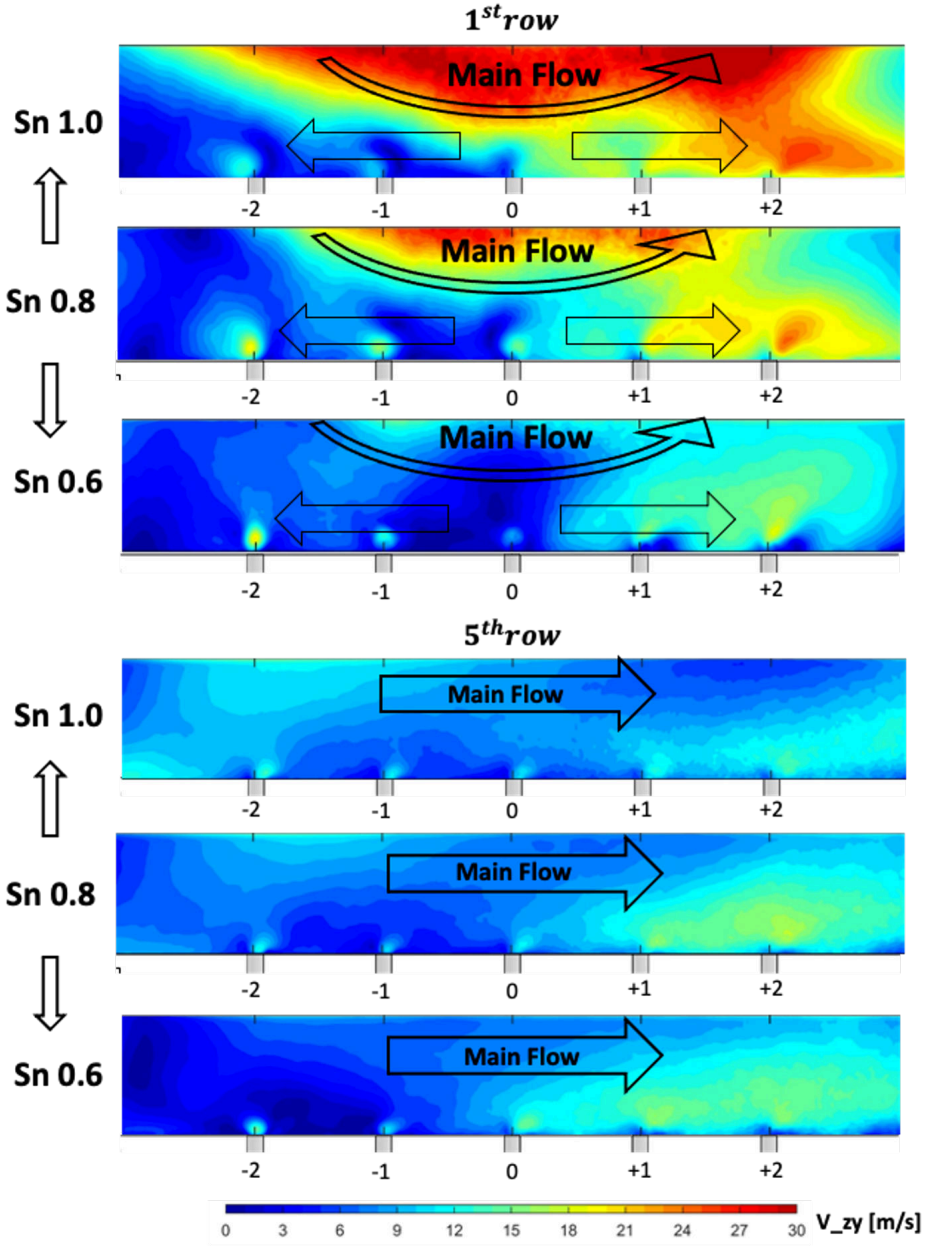

Figure 4.18: Effusion mean flow field on ZY plane. Sn effect, Test Conditions A.

main flow on the coolant jets. Specifically, it is possible to observe that, as the $\Delta p/p_{\text{eff}}$ decreases, the jets undergo a greater dragging from the geometric

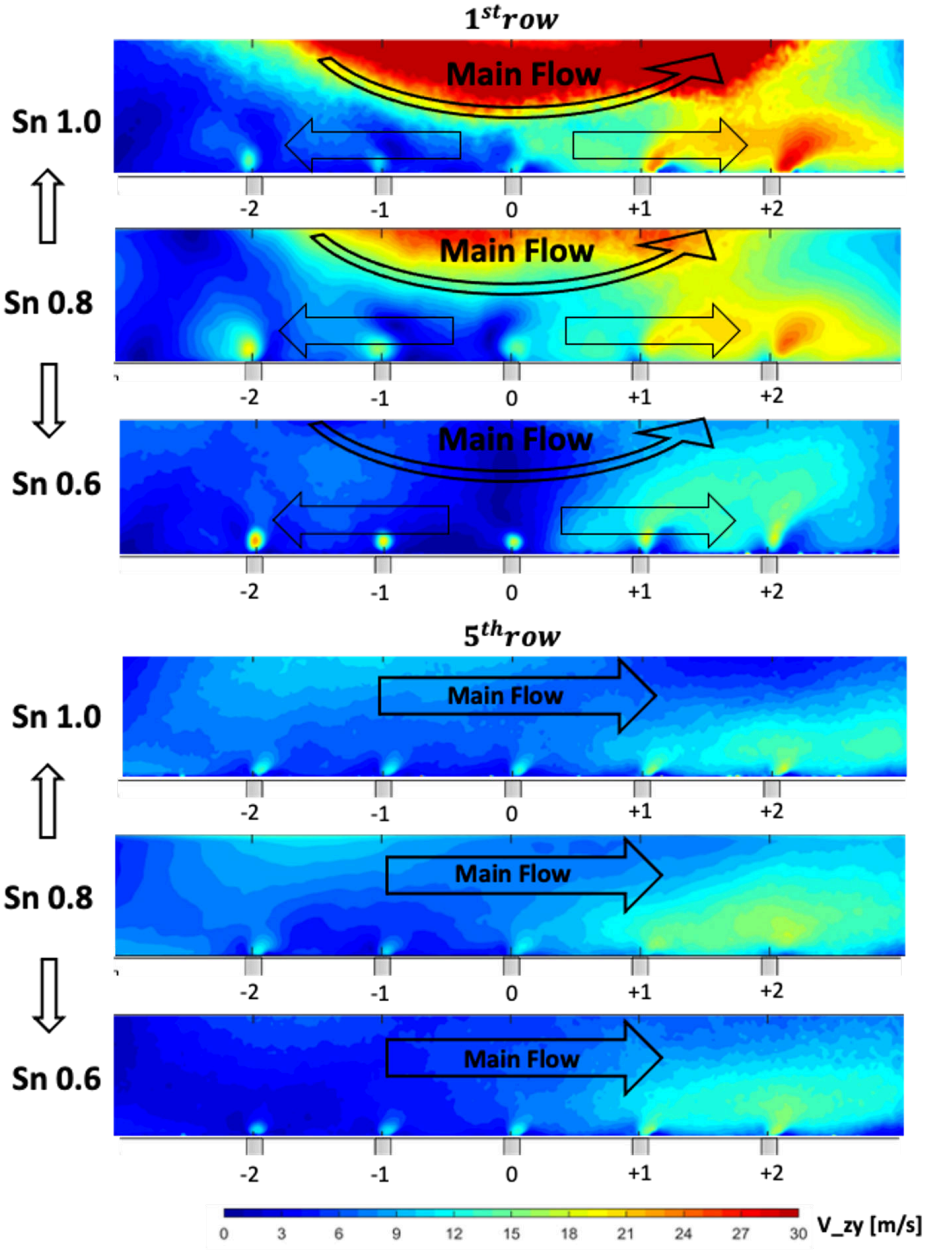

Figure 4.19: Effusion mean flow field on XY plane. Sn effect, Test Conditions B.

holes exit direction. For the $\Delta p/p_{\text{eff}}$=1% case, the jets core on both planes is outside the projection of the hole perforation, a sign of a lateral cross flow

direction. The analysis carried out by varying the Sn, both for test conditions A and B are shown in Fig. 4.18 and Fig. 4.19. In accordance with what is seen in the XY plane for $\Delta p/p_{\text{effM}}$, the increase in the swirl number produces greater deflection on the jets for all the examined rows. The gain obtained, in terms of stability as the swirl number decreases, is lost for $\Delta p/p_{\text{eff3\%}}$ case, due to the increase of the mass flow rate ratio ($\text{m}_{\text{Coolant}}/\text{m}_{\text{Main}}$) that occurs reducing the Sn during the test conditions B.

4.2.2 Unsteady Characterization

Coolant Jets Oscillations

The oscillation of the coolant jets is one of the instability flow mechanisms measured for the effusion flow. These oscillations are triggered by the instabilities of the main jet discussed in previous sections. This subsection shows how these main flow instabilities affect the behavior of the coolant sub-layer. To better understand the dynamics of main-coolant interaction, the three Figures 4.20, 4.21, and 4.22 present a time-resolved evolution of the unsteady structures of the swirling flow that interact differently with the effusion rows. The analysis is shown for the 1st, 3rd, and 7th row for the reference case (Sn=0.8 $\Delta p/p_{\text{eff}}$=3%) test conditions. The images are shown with a time step doubled compared to the acquisition sampling rate. The three temporal analyzes show different types of interaction moving through successive rows.

Looking at the 1st row hole in Fig. 4.20, it is possible to observe in the first snapshot (t=0.000sec.) a turbulent velocity spot of the main flow (highlighted in black) that moves in the direction of the effusion jet and crush it against the plate (red arrows). In t = 0.002sec, the fluctuation of the main jet allows the coolant jet to return to its stable position. Afterward, the counterclockwise vortices of the OSL interact with the coolant jet in reverse flow condition. The coolant is dragged upwards (red arrows), preserving its structure (t = 0.004, 0.006sec.). Following, the inverse phase of the mainstream fluctuation pushes the coolant again on the liner wall (t=0.008, t=0.010 sec.). This jet oscillation phenomenon, triggered by the main flow,

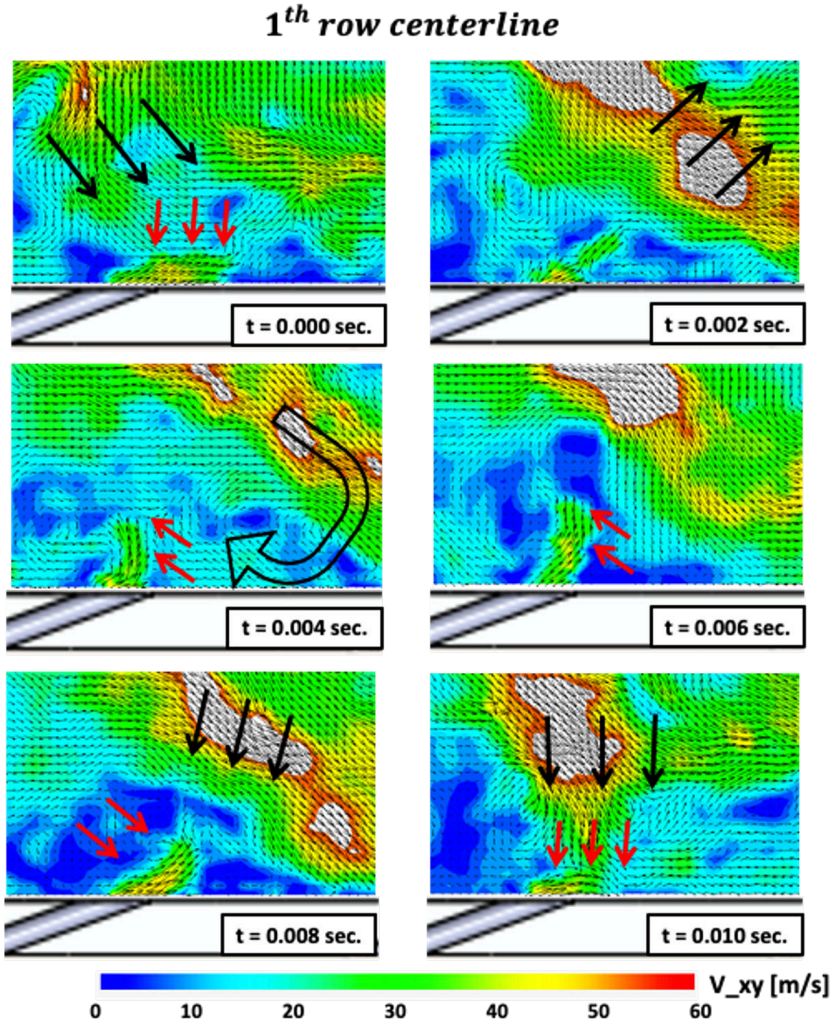

Figure 4.20: 1st row: Time-Resolved analysis of the main - coolant flows interaction.

occurs periodically and continuously over the entire measured time period. Also the behavior of the hole located in the 3rd row, close to the impact point of the main flow, is anomalous. The time-resolved analysis in Fig. 4.21 shows the coolant jet constantly pushed against the wall. It is highlighted by red arrows (t=0.004 sec. and t=0.006sec) that the jet cannot counteract the effect of the turbulence of the main flow and starts small up-down oscillations remaining close to the wall. This suggests jet stability, which remains constantly attached to the liner. The 7th row analysis presents a third type

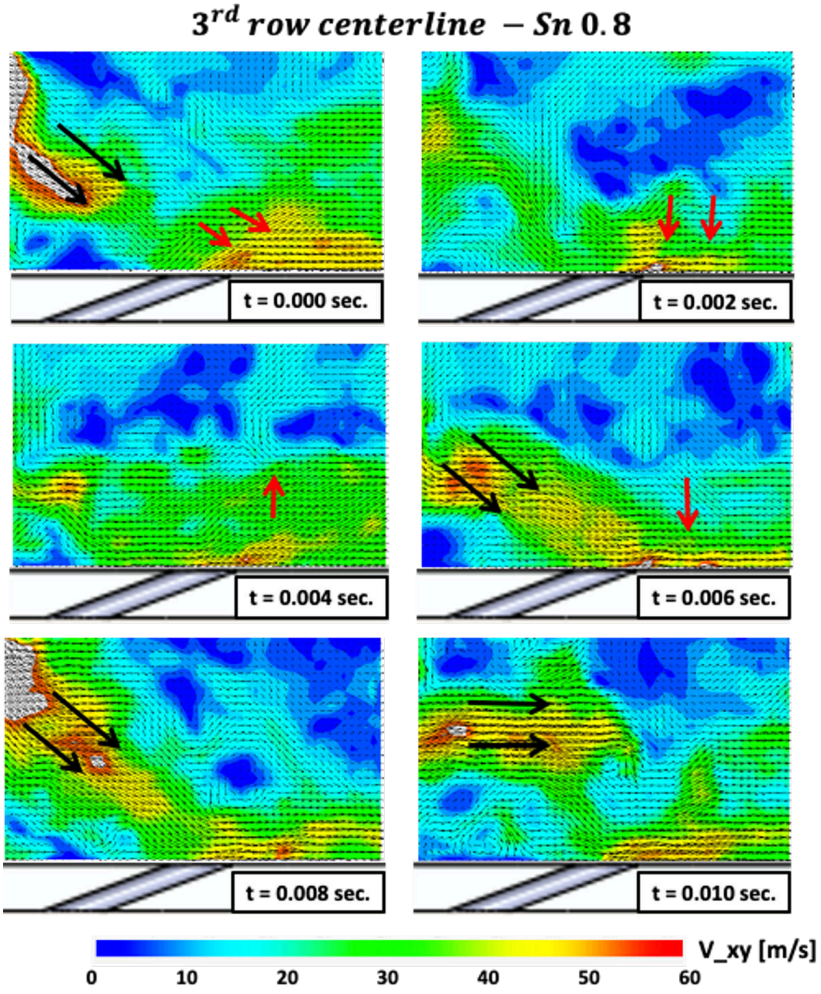

Figure 4.21: 3rd row: Time-Resolved analysis of the main - coolant flows interaction.

of jet fluctuation behavior, more similar to what can be expected for a classic jet in crossflow. In fact, the 7th row is in the area of the test cell less influenced by the swirling flow. Here the main flow is parallel to the plate and in the deceleration phase. However, its turbulent contribution is sufficient to trigger fluctuations on the coolant jets. In Fig. 4.22, at $t = 0.0006\ s$ and $t = 0.002\ s$, a main flow turbulent spot starts to strike the cooling jet which has a direction alligned with that of the exit angle of hole perforation. The fourth snapshot ($t = 0.0033\ s$) shows the cooling jet still well structured

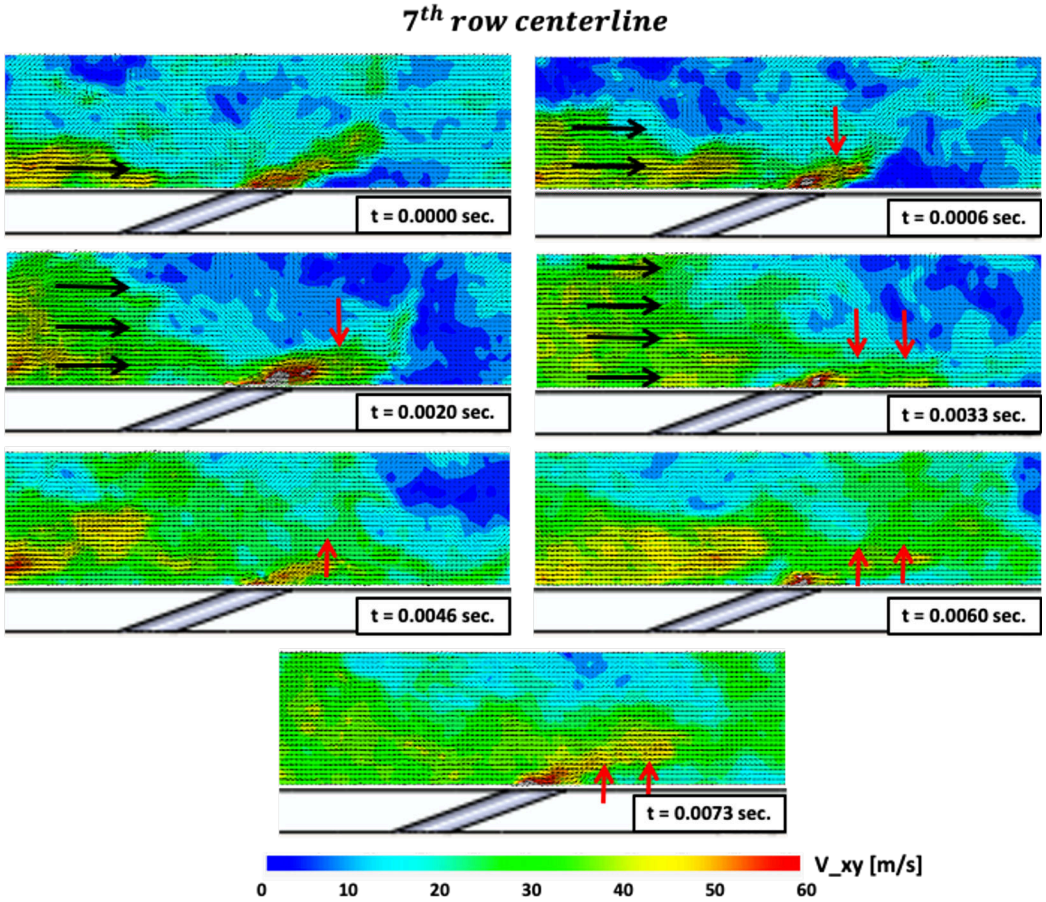

Figure 4.22: 7th row: Time-Resolved analysis of the main - coolant flows interaction.

and defined but completely attached in its length to the plate, crushed by the main flow. Continuing the analysis with the following snapshots, the jet realigns with a trajectory in agreement with the hole inclination. This dynamic occurs whenever turbulent spots of the main flow interact with the jets, and also in this case, the oscillations are constant throughout the entire time samples and triggered by the main flow.

For a better quantitative analysis of the oscillations by varying the feeding pressure drop, Fig. 4.23 shows instantaneous streamlines for the first fourth holes of the centerline (1st, 3rd, 5th, and 7th rows) for the reference Sn=0.8

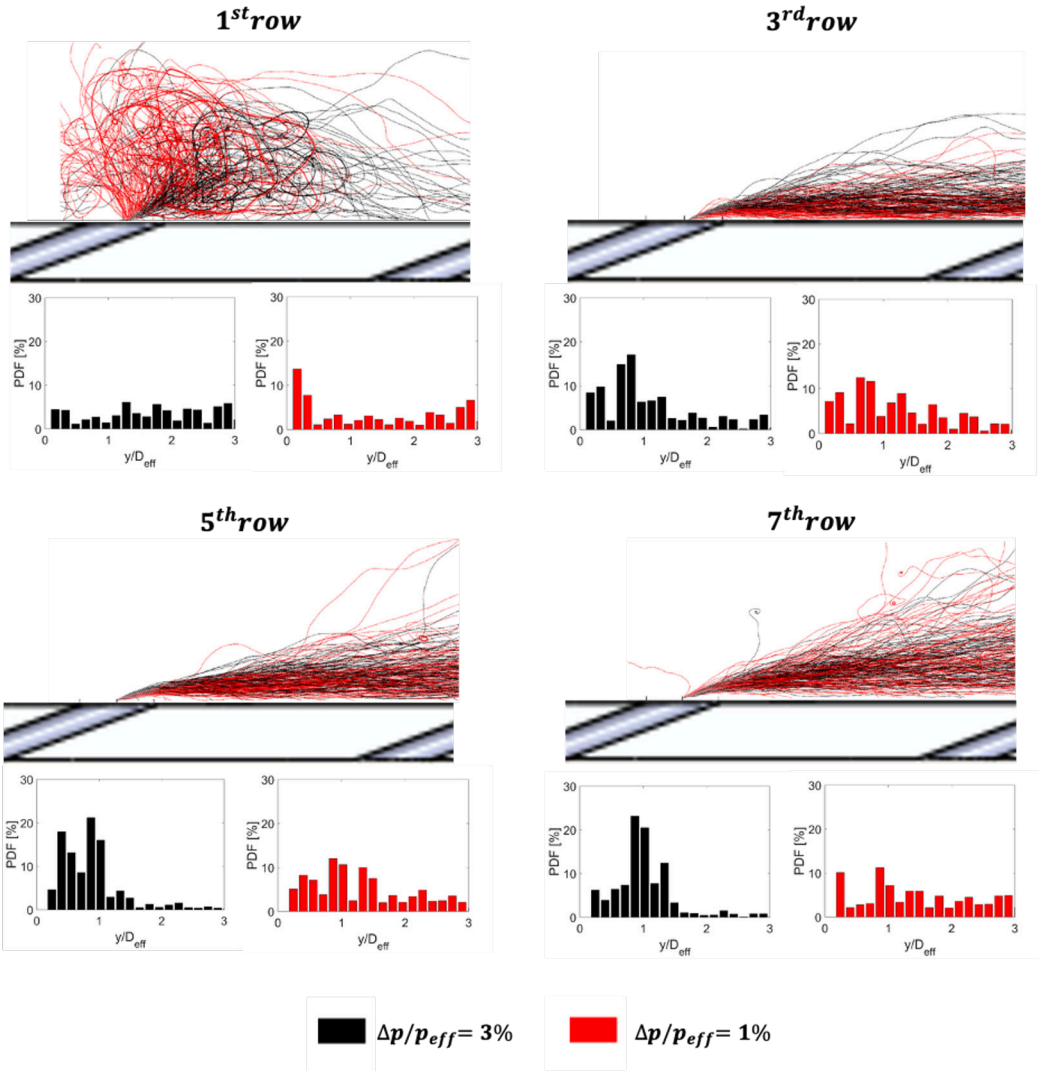

Figure 4.23: Instantaneous velocity streamlines by varying the pressure drop. Bottom: PDF of the velocity maximum y position measured at 2 D_{eff} distance from the holes trailing edge. Black line = $\Delta P/P = 3\%$; red line= $\Delta P/P = 1\%$

case. For the calculation of the streamlines, the approach proposed by [74] has been used. For each image, the streamlines are calculated starting from the center of the holes using the "streamline" Matlab function: every streamline, therefore, visualizes the flow condition of one single snapshot, which, however, well represents the fluctuation of the cooling jet trajectory. In each

plot, 100 streamlines are drawn using black lines for $\Delta p/p_{\text{eff}}$=3% and red lines for the $\Delta p/p_{\text{eff}}$=1% case. The results underline an extremely different behavior between the different holes, confirming the time-resolved visualization. A less stable jets evolution occurs as evidenced by the increased spreading of the streamlines reducing the feeding pressure drop. With a $\Delta P/P = 1\%$, the behavior is more unstable with the instantaneous streamlines, which present a spread and chaotic distribution mostly in the first row, in agreement with what is detected in Fig. 4.23. Reducing the plate feeding pressure drop, the oscillatory phenomena, and the crushing of the jets to the wall increase due to the reduction of the jet momentum. The jets of the third and fifth row are constantly pushed downwards; this creates a phenomenon of greater stability, with a reduction of the diffusion of the streamlines. Symmetrical oscillations and a reduced crushing to the wall occur only from the seventh row, a sign of less dependence on the swirling flow. This type of analysis is summarized, taking into account the entire statistical sample (1500 instantaneous snapshots for case), in the probability density functions (PDF) reported on the bottom part of Fig. 4.23. The histograms are made tracking the y position of the velocity maximum values, conceivable as the core of the coolant jet, measured at 2 D_{eff} distance from the holes trailing edge. It is possible to see that for higher pressure drop values, there are preferential positions of the jet core, synonymous with greater stability. In particular, for the 5th and 7th rows for $\Delta p/p_{\text{eff}}$=3%, a Gaussian trend is recognizable in PDF, and the core of the jets stay mainly $\approx y/D_{\text{eff}}$ 0.75 (5th row) and 1 y/D_{eff}(7th row) at this point of the plate. To conclude the analysis, the statistical results of the jet fluctuations obtained by varying the Sn for both test conditions A ($\Delta p/p_{\text{effM}}$) and B ($\Delta p/p_{\text{eff3\%}}$) are reported in Fig. 4.24. Starting from the test conditions A (black plot), a jet more stable behavior with a gaussian shape was recorded in the first row for Sn=0.6. On the other hand, the 3rd row is located exactly in the region with the higher interaction with the swirling jet. As a consequence, the jet is lifted up and squashed down continuously by the swirling jet oscillation, and the PDF does not have a clear peak value. Considering the Sn=1.0 case, the oscillations increase for the row in the IRZ. Nevertheless, the subsequent rows show good stability, moving away from the dome.

Probably, the high tangential velocity and the radial trust induced by the Sn=1.0 geometry reduce the oscillatory phenomena pushing the downstream jets against the wall. This creates good stability in terms of jets oscillation, with the 3rd, 5th, and 7th rows, which present more stability with respect to the Sn=0.6 case. Test conditions B (green plot) shows, in line with all the results observed so far, a reduction on the jets stability for Sn=0.6 and an increase for Sn=1.0. This phenomenon is always referable to the imbalance of the mass flow rate ratio. In this case, the changes in stability that occur due to the respective increase (Sn=1.0) or reduction (Sn=0.6) of the cooling feeding pressure drop are the same as detected in Fig. 4.23.

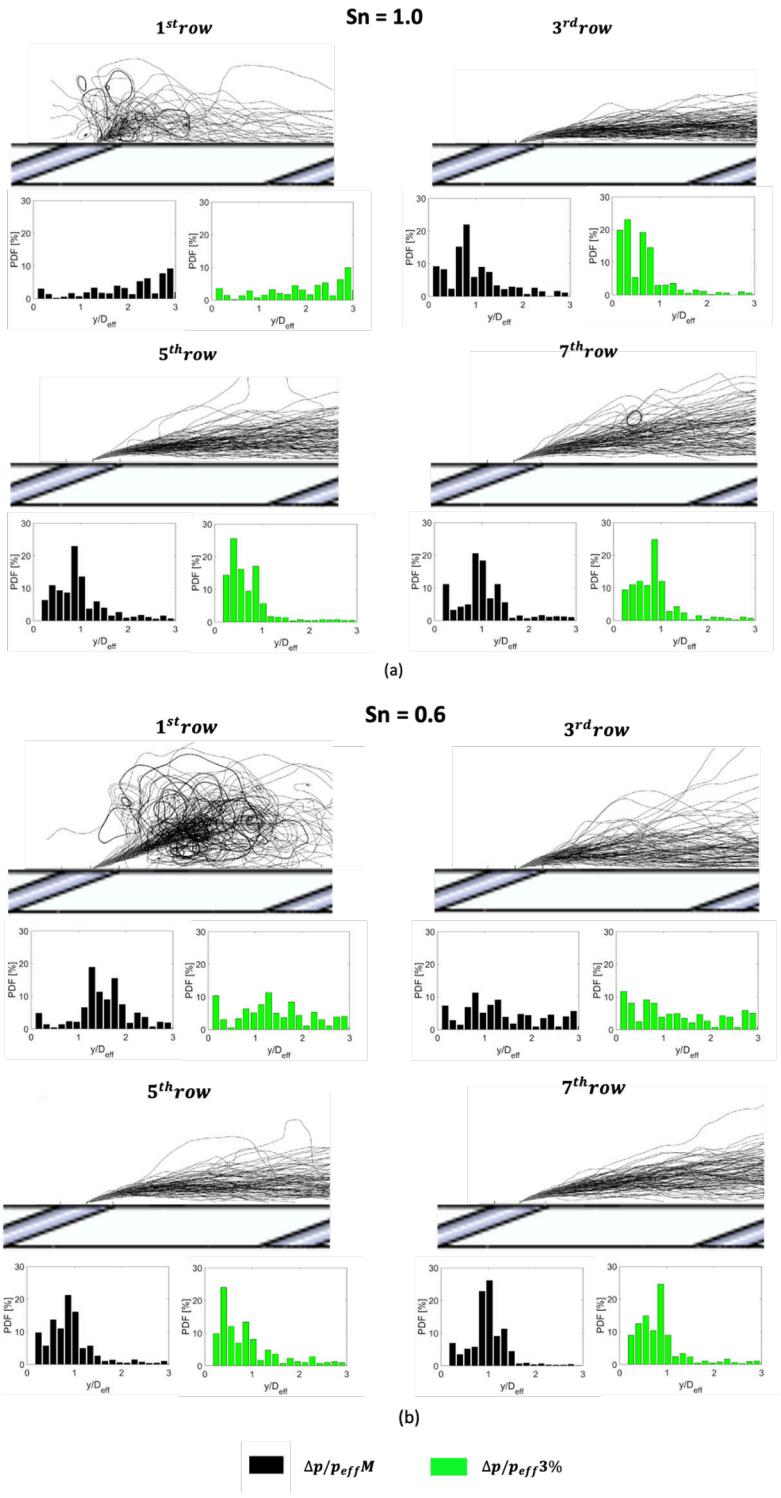

Figure 4.24: Instantaneous velocity streamlines for Test Conditions A. Bottom: PDF of the velocity maximum y position measured at 2 D_{eff} distance from the holes trailing edge. Black = Test c. A; Green = Test c. B.

Kelvin Helmholtz Instabilities

An analysis of the Kelvin Helmholtz (KH) instabilities that characterize the effusion cooling jets has been carried out in correspondence with the effusion plate centerline (XY symmetry plane). In the following, the vorticity values w have been scaled by the exit jet velocity $U_{\Delta p/peff}$ promoted by the $\Delta p/p_{\text{eff}}$ used to fed the effusion plate. To better understand the unsteady phenomena occurring within the shear layer of the cooling jets, instantaneous flow structures of the first and second row holes, obtained through a CFD SBES (stress-blended eddy simulation) analysis carried out for this test rig [75] with an effusion pressure drop equal to 3.5%, are shown in Fig. 4.25. The 3D KH structures are recognizable thanks to a transported scalar applied to the coolant flow rate in the inlet boundary conditions to track the coolant flow. On the 3D iso-surfaces are plotted the vorticity values: the K-H anti-clockwise vortices (red) and the K-H clockwise one (blue) that are the result of the interaction between the shear layer of the jet and the surrounding flow. Regarding the anti-clockwise vortices, they are positioned on the outer shear layer of the jet and evolve from the leading upstream edge of the film cooling hole as highlighted with the letter A. K-H clockwise vortices instead come from the downstream edge of the hole, as highlighted with the letter B. On the top left side of Fig. 4.25 a spectra of the fluctuating values of the transported scalar concentration (TSC') is shown. The concentration was detected near the leading edge of the hole. It is possible to see in the spectrum a strong anomaly with a central peak around 5000 Hz. This is the average frequency of detachment of anti-clockwise vortices, which, however, have a relatively wide distribution between 4000 and 6000 Hz, due to the turbulent nature of the main flow field that translates in instantaneous pressure drop and so frequency detachment fluctuations. Once the detachment frequency has been measured numerically, it is concluded that the PIV carried out can provide important information about the KH eddies in instantaneous and average terms, without, however, allowing a TR analysis. In fact, the utilized acquisition rate (PIV: 1500 Hz) is far below that of eddies detachment of the jets shear layer.

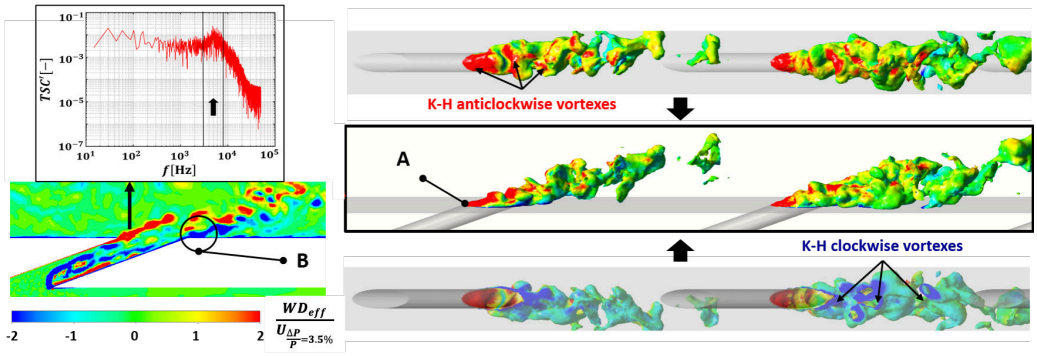

Figure 4.25: Contour of transported scalar concentration in the effusion region (left-up), contour of vorticity field inside the perforation (left-down) and iso-surface of transported scalar equal to 0.4 colored by vorticity

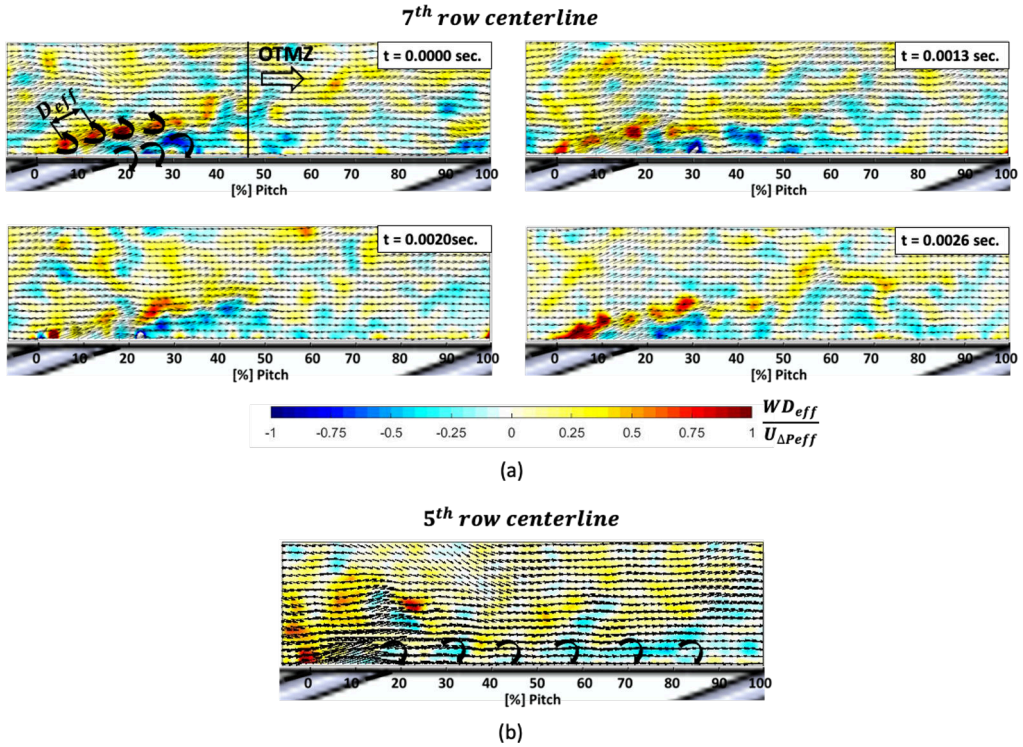

Figure 4.26: Instantaneous vorticity snapshots. Sn = 0.8, effusion $\Delta p/p$=3%.

Fig. 4.26 (a) and (b) report instant snapshots of the K-H instabilities measured on the 7th (a) and 5th (b) rows (Sn08 case). The counter-clockwise positive structures are marked in red, and the clockwise negative eddies are marked in blue on the contour. The K-H instabilities are also visible thanks to the overlap of vector maps that show the deflections of the velocity field on the jet shear layer. Referring to $t = 0.0000sec.$ they are highlighted with rotating black arrows. In (a), the instabilities have a coherent and well-defined structure with a defined length-scale of the eddies of about one hole diameter. Looking at the whole time series in (a), moving away from the holes, these vortices are convected downstream with the cooling jet flow, and the vorticity structures progressively decay to a homogeneous turbulent mixing zone (OTMZ) highlighted in the first contour. In fact, in the shown contours after $\approx 50\%$ of the pitch it is impossible to identify coherent eddies structures. The snapshot in (b), 5th row, presents a different behavior, which appears when the cooling jets are very flattened towards the liner wall by the swirling main flow. It is possible to see that the classical KH instabilities are not detected. Instead, clockwise vorticity (highlighted with black rotating arrows in the contour) moves along the wall, appearing like weak span-wise vorticity. This phenomenon is more pronounced for the holes near the main jet impact point, which are more squashed to the wall by the swirling flow. The vorticity results, in average terms, are illustrated in Fig. 4.27 for the reference Sn=0.8 case. The contours shown the average of the instantaneous values of vorticity. In the top of Fig. 4.27, there is a global view of the coolant sub-layer, while at the bottom, there are enlargements of the holes. The red-blue spots that propagate on the shear layers from the edges of the holes are the average contributions of the counter-clockwise and clockwise vortices. Due to their different positions with respect to the injector, the holes show different behaviors in terms of vorticity, confirming the non-uniformity of the flow field even in unsteady terms.

The first hole presents the highest vorticity values. Its more upright position allows the development of stable KH structures over the entire annular shear layer of the cooling jet. Instead, the KH instabilities appear compromised for the 3rd row hole, which is located in the impact zone and the main

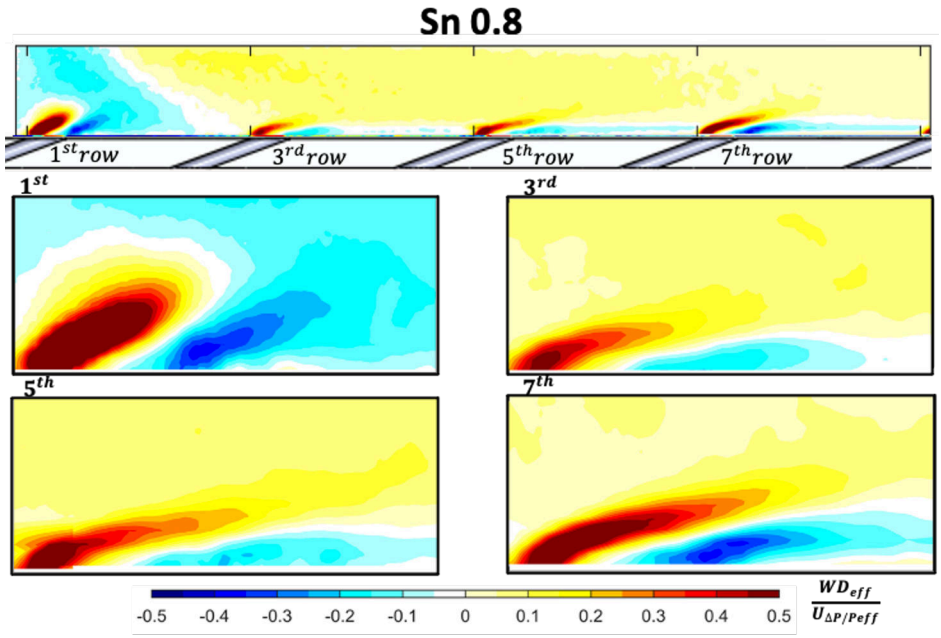

Figure 4.27: Vorticity time-average contribution on XY plane. Sn = 0.8, effusion $\Delta p/p$=3%.

flow and squashed against the liner. The measured clockwise negative vorticity is lower for all the holes due to the absence of direct interaction with the free stream due to the low inclination of the jets (20 °) that promote the continuous interaction with the wall. This occurrence increases close to the impact zone. In fact, the swirling flow crushes the jets to the wall avoiding the development of vorticity. For all the holes, after about 30% of the pitch, the OTMZ appears and close to the liner wall the trace left by the span-wise vortices, described above in Fig. 4.26 (b), is present.

The decreasing of the feeding pressure drop causes a progressive weakening of the structures on the coolant jet shear layers. This trend is visible in Fig. 4.28, where the vorticity magnitude characterization of the coolant sub-layer is shown by varying the $\Delta p/p_{\text{eff}}$. The reduction of the jets velocity reduces the intensity of the instabilities. Besides, the increased impact of swirling flow on the cooling jets further worsens their structure, starting a

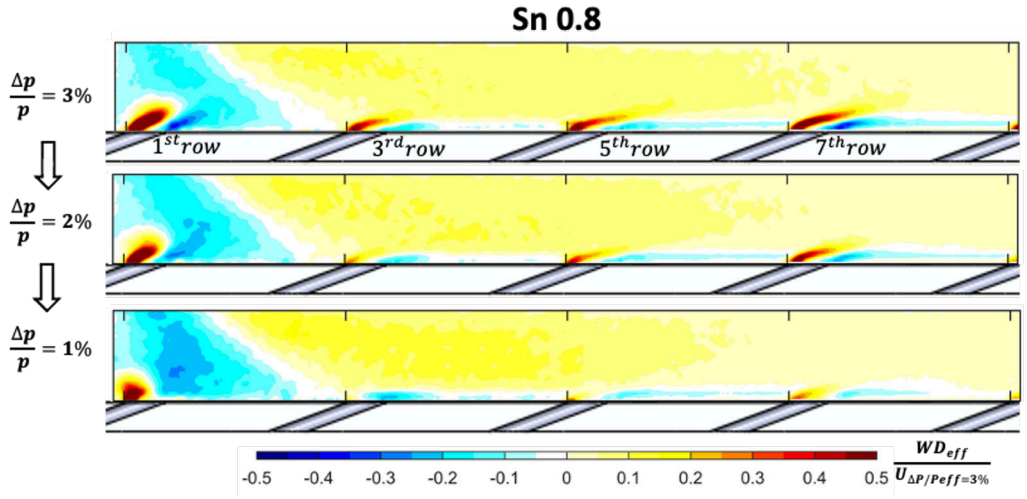

Figure 4.28: Vorticity time-average contribution on XY plane. Sn = 0.8, effusion $\Delta p/p$=3, 2, 1%.

faster turbulent decay process. In fact, vorticity spots are barely visible for $\Delta p/p_{\text{eff}}$=2%. Instead, they are absent in $\Delta p/p_{\text{eff}}$=1% case. Only weak traces of span-wise eddies remain along the plate wall. Fig. 4.29 shows the vorticity values measured by varying the Sn for both test conditions A and B. The Sn=1.0 case, in the test conditions A, presents a low clockwise vortex contribution due to the greater flattening of the jets to the wall. The anti-clockwise contribution is also reduced by the interaction with a more aggressive swirling flow. In line with all the trends discussed so far, as the Sn decreases, the jets have a behavior less affected by the swirler, especially for the 5th and 7th rows, where higher vorticity values were measured. The contours appear similar by varying the Sn matching the effusion feeding pressure drop (test conditions B, $\Delta p/p_{\text{eff3\%}}$), in line with what was previously analyzed.

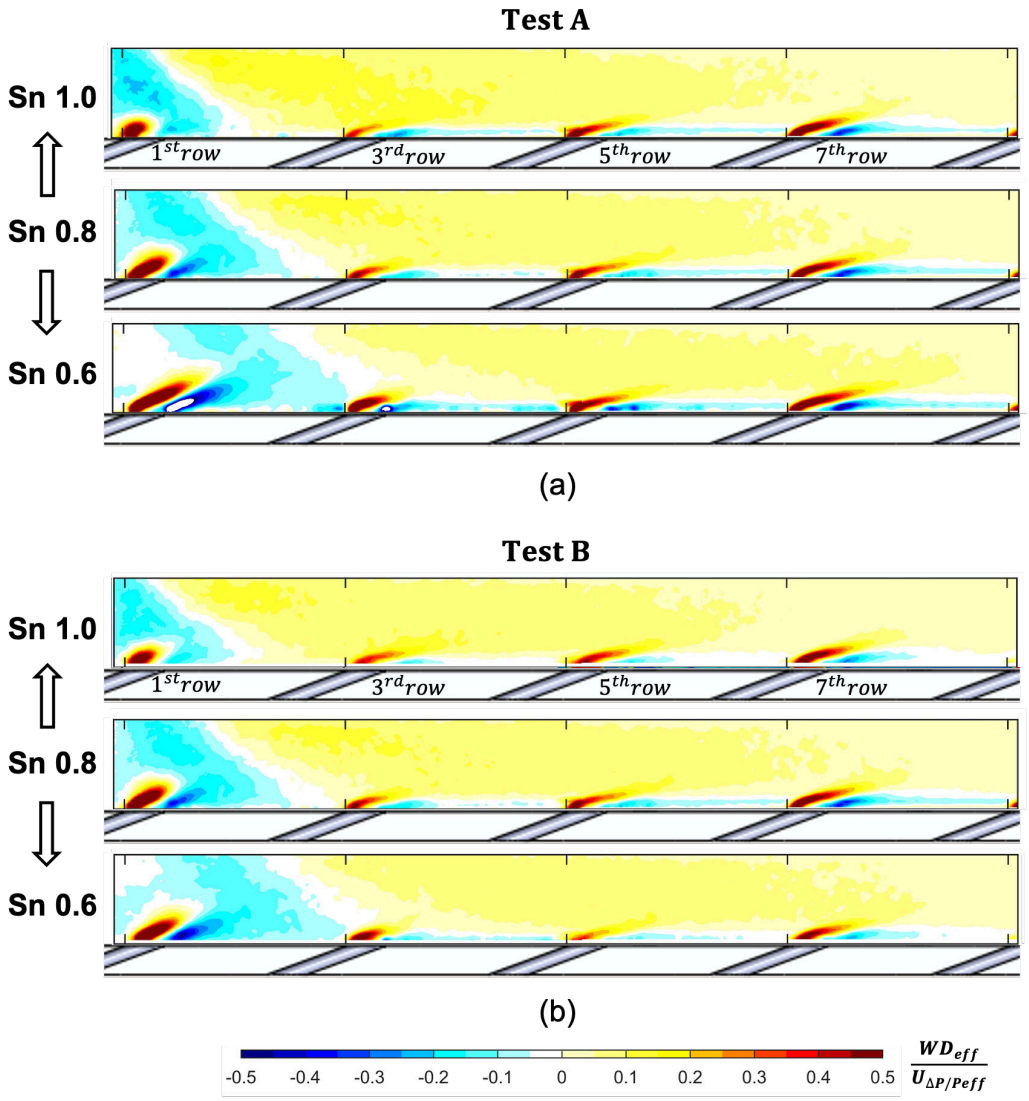

Figure 4.29: Vorticity time-average contribution on XY plane. Sn effect for Test Conditions A and B.

4.2.3 Velocity Root Mean Square and Turbulence Analysis

The characterization of the unsteady phenomena carried out so far is quantified in this section in terms of RMS and Tu. The equations used for

the post-process of the data are Eq. 4.3 and Eq. 4.4. Maps of RMS velocity values on XY and ZY planes are shown in Fig. 4.30 at reference conditions. The contribution of Kelvin Helmholtz instabilities is marked with the letter A; C is used for the homogeneous turbulence decay in correspondence with the OTMZ. B is used for the fluctuations induced by the main flow, D for the intermittent attachment and detachment of the jets to the wall, and G for the rotating vortex contribution (CRVP and single rotating vortex).

Looking at the first plane XY (Fig. 4.30(a)), in accordance with the vorticity analysis on the meridian plane in Fig. 4.27, strong values of RMS are achieved on the shear layer of the jets (A) starting from both the leading and the trailing edge of the holes where the K-H instabilities are formed and convected downstream. The contribution of KH instabilities is greater on the first and seventh rows as previously justified (reduced effect of swirling flow on the jets development). On the other hand, the KH contributions for the 3rd row are not distinguishable. Here, in line with the vorticity analysis, the continuous crushing of the jet against the wall prevents the regular formation of KH vortices. K-H contributions merge in the region (B) for the 1st and 7th rows due to oscillatory behaviors that compromise the shear layer stability. Downstream the holes, a turbulence decay (C) starts, and the RMS maps appear more homogeneous. The continuous attachment and detachment of cooling jets at the wall promote a more homogeneous pattern downstream of the 3rd row (D). Jets oscillations contribute to high turbulence levels, also in ZY planes visible in Fig. 4.30(b). Especially in the first row, due to the oscillatory phenomena in the Z direction, the spots of RMS values at the core of the jets are very high. In addition to this phenomenon, the turbulent vorticities produced in the the holes perforation must also be considered. Finally, looking at the ZY plane, it is also possible to recognize the contribution of unsteady terms of the rotating vortex (G), which replace the CRVP, shown in the time-average analysis. Spot F is given by the turbulent contribution of the main flow, which is added to that of the jets. Fig. 4.31 shows the RMS and Tu contours by varying the effusion plate pressure drop for the reference case Sn=0.8. The progressive reduction of pressure drop shows that the RMS contributions (Fig. 4.31 (a)) that can be

connected to the KH instabilities decrease in accordance with the vorticity analysis. The turbulent decay begins closer to the holes perforation, and only the stable core of the jet (in blue) is visible in the map in correspondence with the edges of the holes. For the $\Delta p/p_{\text{eff}}$=1% case, the RMS contribution connected to the jets oscillations is not detected due to the strong reduction of the jet momentum. In fact, the jets are constantly pressed against the wall without showing large oscillations, as shown in the oscillation analysis for this pressure drop value. Observing the turbulence contours (b), it is possible to see that the coolant sub-layer becomes more unstable under the stronger effect of the swirling flow, with higher turbulence values as the $\Delta p/p$ decreases. This means that the low momentum of the jets is not able to hinder the main flow and to create a stable cold sub-layer.

Fig. 4.32 shows the Tu values measured by varying the test conditions. Looking at the test conditions A (Fig. 4.32 (a)), as confirmed by the previous analysis, the KH instabilities contribution is greater as the Sn increases. In fact, observing the exit of the jets, turbulence spots located at the edge of the holes are more intense for Sn=0.6. The coolant sub-layer loses stability for Sn=0.6. In fact, the jets, less crushed to the wall, are in penetration regime as visible in figure for the 5th and 7th rows. Reducing the swirl number, the impact point moves further downstream increasing the instabilities of the third row. Instead, reducing the Sn, the stability of the 1st increases, according to the main flow field analysis (Fig. 4.6), which shows that the ORZ becomes more stable, reducing the Sn. It can also be concluded that as Sn increases (Sn=0.8 and Sn=1.0), the rows immediately after the main jet impact zone (3rd and 5th) benefit from the flattening to the wall in terms of stability. In fact, the tangential velocity of the swirling main flow reduces the cooling jets oscillatory phenomena pushing the jets against the wall. Small changes to the turbulence values are visible for the test conditions B (Fig. 4.32 (b)). For Sn=1.0, in accordance with the oscillation analysis (Fig. 4.24), an increase in the effusion plate feeding pressure drop creates greater stability of the jets and, therefore, lower turbulence values in the coolant sub-layer. On the contrary, by reducing the pressure drop for Sn=0.6, an increase in oscillations leads to greater instability, with higher turbulence

values on the coolant sub-layer. For Sn=06, the turbulence values on the edges of the holes are also reduced, due to the decrease of the KH vorticity contribution promoted by a jets velocity reduction, in agreement with the vorticity analysis (Fig. 4.29).

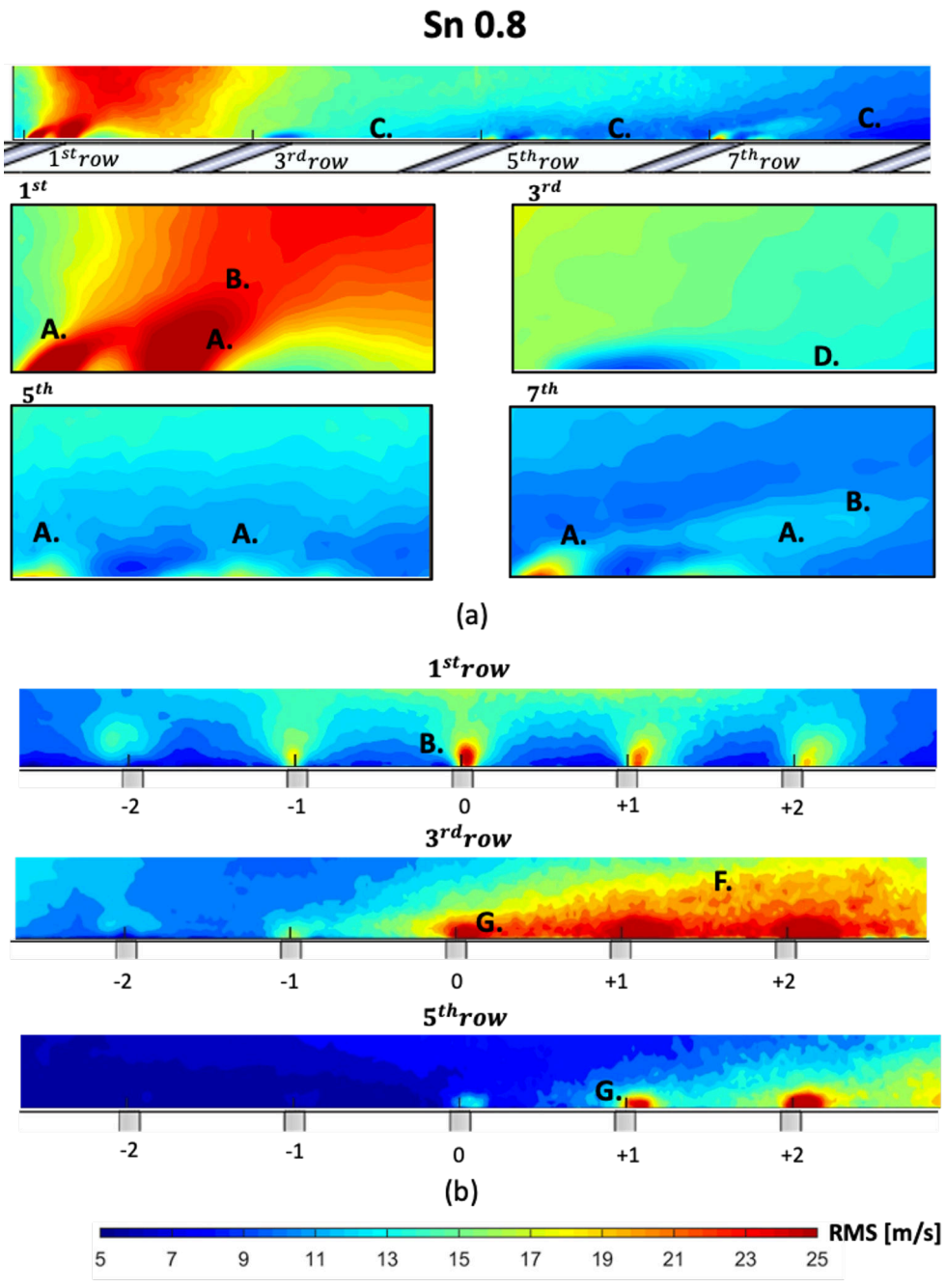

Figure 4.30: RMS values on XY plane (a) and ZY plane (b). Sn = 0.8, effusion $\Delta p/p$=3%.

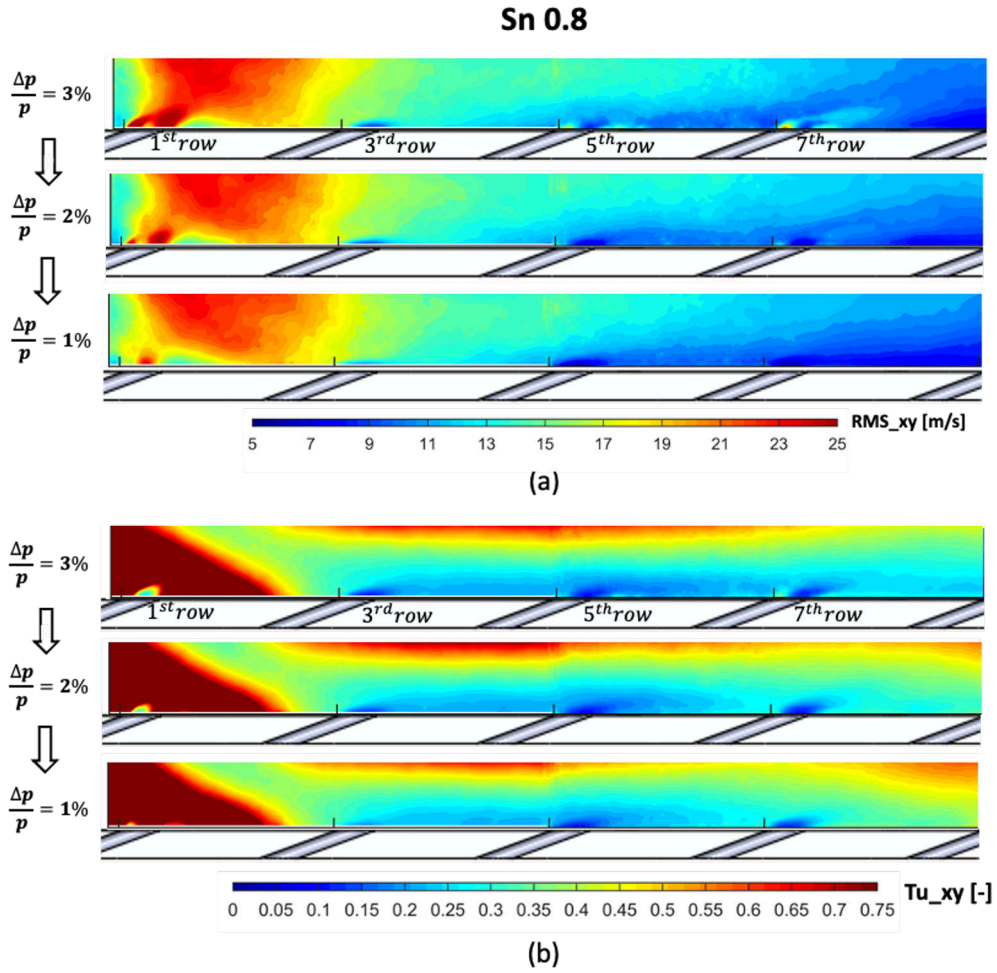

Figure 4.31: RMS (a) and TU (b) measured values on XY plane. Sn = 0.8, effusion $\Delta p/p$=3, 2, 1%.

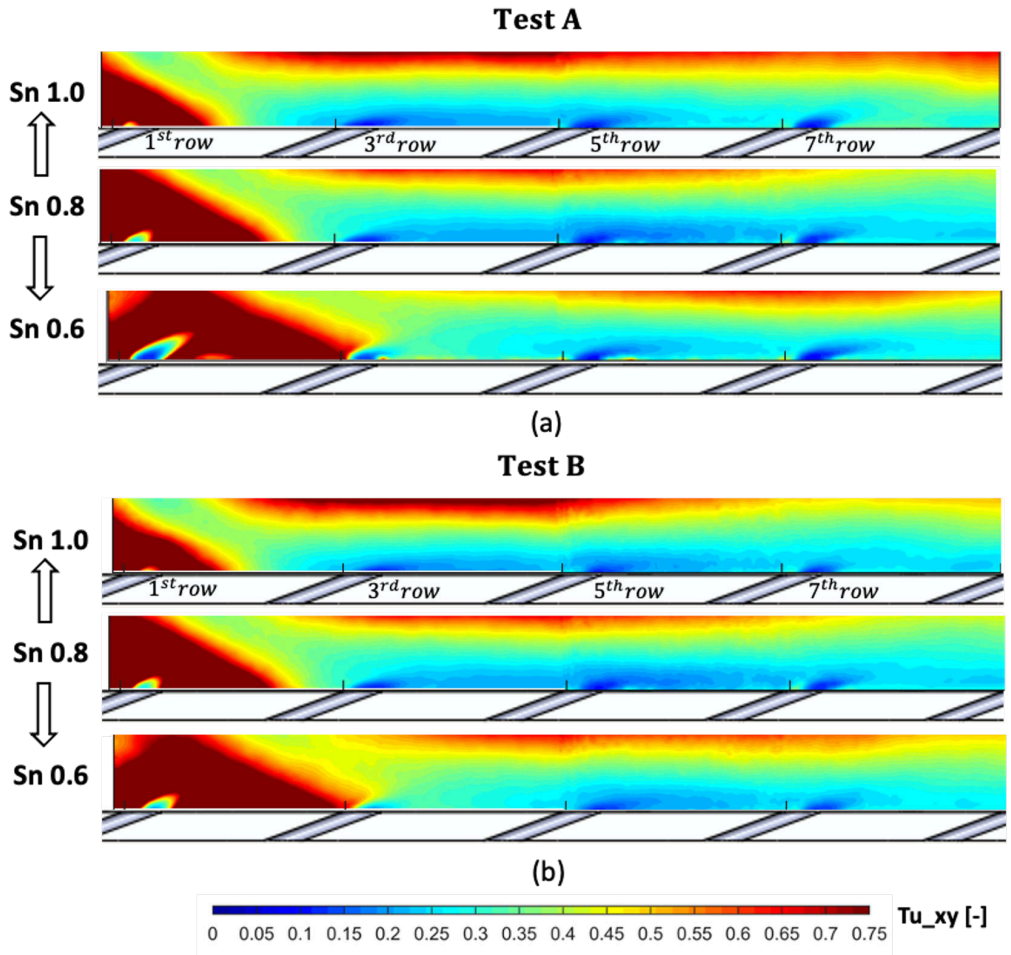

Figure 4.32: Tu measured values on XY plane. Sn effect for Test Conditions A and B.

Chapter 5

Adiabatic Effectiveness Results

Contents

This chapter reports the adiabatic effectiveness results measured on the effusion test plate using the FPSP technique. The results are presented for the reference Sn=0.8 case by varying the effusion system feeding pressure drop ($\Delta p/p_{\text{eff}}$). After, the characterization moves to a comparison between the injectors (Sn=08, Sn=1.0, Sn=0.6) for both the proposed test conditions shown in Chapter 2, Section 2.2.

5.1 Time Average Analysis

The results of the mean adiabatic effectiveness were obtained by averaging the single snapshots (N samples = 1000) acquired with a sample rate = 1000Hz. Fig. 5.1 shows the results of adiabatic effectiveness for Sn=08 by varying the $\Delta P/P_{eff}$. Starting from the reference case ($\Delta P/P_{eff}$=3%), the effectiveness distribution in the contour is strongly influenced by the presence of the swirling main flow. The holes of the 1st row, in correspondence with the ORZ, promote a homogeneous film in the direction of the dome (reverse condition).The impact zone is characterized by effectiveness values close to zero, and there are no developed traces of the jets, unless local spread

protection around the holes. Following, the distribution is characterized by a non-symmetric area. In fact, the traces of the jets appear deflected in accordance with the direction of rotation of the swirling flow, and with the flow field measured close to the wall (Ch. 4, Fig. 4.3). Furthermore, the traces of the jets appear very diffuse. This occurrence depends on two main factors: the squashing of the jets against the wall promoted by the swirling main flow, as previously verified with PIV measurements, and the unsteady behavior of the main flow, which creates lateral oscillations of the jets. From the fourth row, in correspondence with the deceleration zone of the main flow, the superposition effect of the jets occurs with beneficial results on the effectiveness values and their homogeneity, as also shown by the plot whit the laterally averaged 1D result measured on the test plate (Fig. 5.1 bottom). The reduction of $\Delta P/P_{eff}$ significantly increases the impact of the main flow on the effectiveness values as shown on the contours (Fig. 5.1 top) and in the 1D plot (Fig. 5.1 bottom). In general, a reduction in the effectiveness values is measured. In the ORZ and in the main flow impact zone, the film is absent, and regular jets development is further limited. In particular, for $\Delta P/P_{eff} = 1\%$, the surface with effectiveness values equal to zero reaches the 5th row. Furthermore, the reduction of the jets momentum produces a greater lateral deflection of the jets trajectory than in the $\Delta P/P_{eff} = 3\%$ case. The 1D plot well describes this trend showing a consistent reduction in effectiveness values. On the other hand, a beneficial effect, obtained by reducing the feeding pressure drop, is represented by the greater flattening of the jets to the wall. In fact, as can be seen from the contours, the peak values of adiabatic increase immediately downstream the holes leading edge, reducing the $\Delta P/P_{eff}$. This is also revealed by the 1D plot, where peak values remain high despite the lateral average. The 1D plot also shows that a homogeneous distribution (absence of peaks) and a superposition of the effects is more difficult to achieve by decreasing the $\Delta P/P_{eff}$.

Fig. 5.2 shows the measurements of adiabatic effectiveness by varying the Sn for test conditions A. Looking at the contour (Fig. 5.2, top), it is possible to observe that the influence of Sn is extremely relevant. In the ORZ and the swirler impact zone for Sn=1.0 the effectiveness values are low,

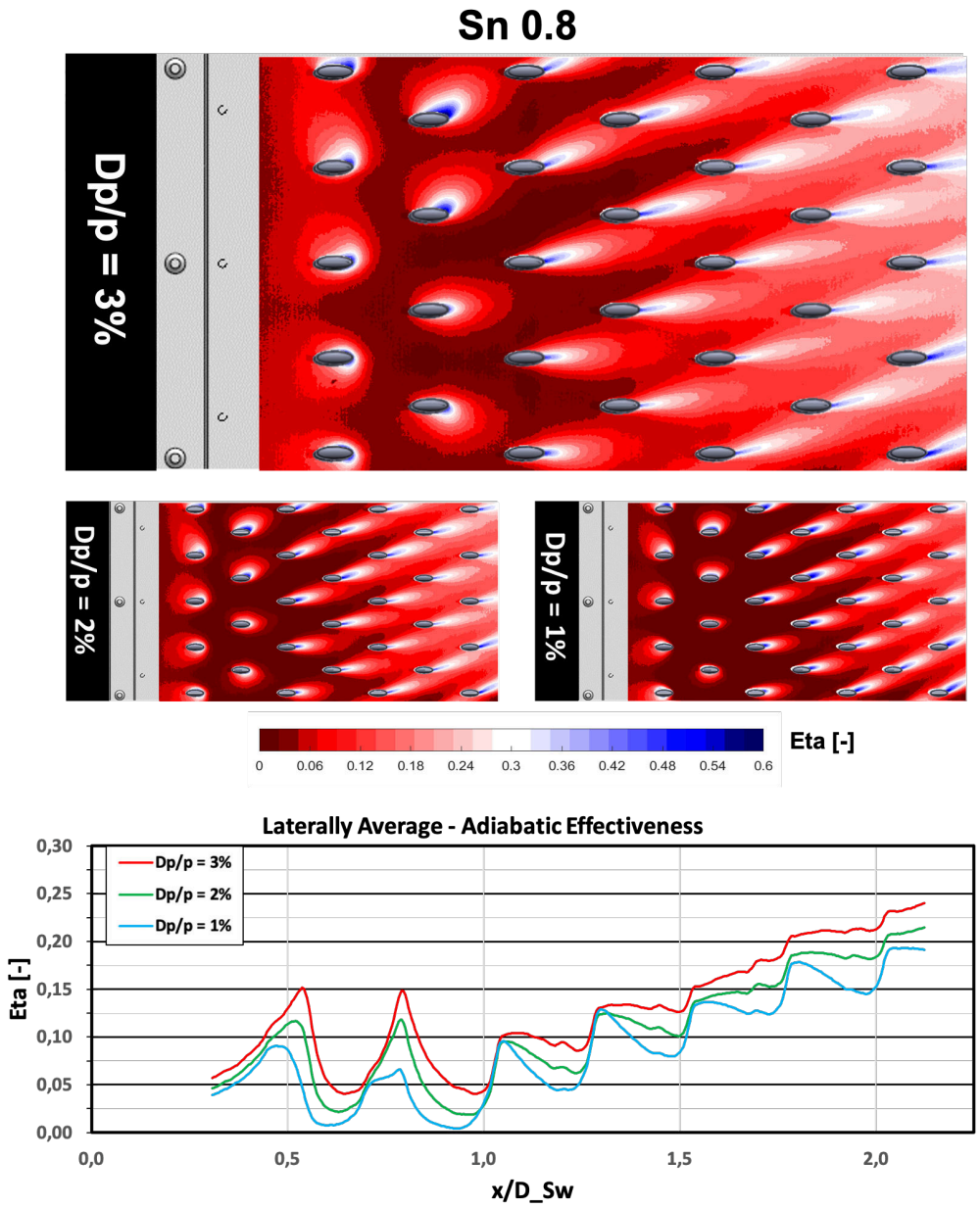

Figure 5.1: Top: adiabatic effectiveness contours: Sn=0.8 case effect of $\Delta P/P_{eff}$. Bottom: laterally averaged adiabatic effectiveness distribution.

and the cooling system does not promote a coolant sub-layer up to the 4th row of holes. Conversely, for Sn=0.6, very homogeneous effectiveness values

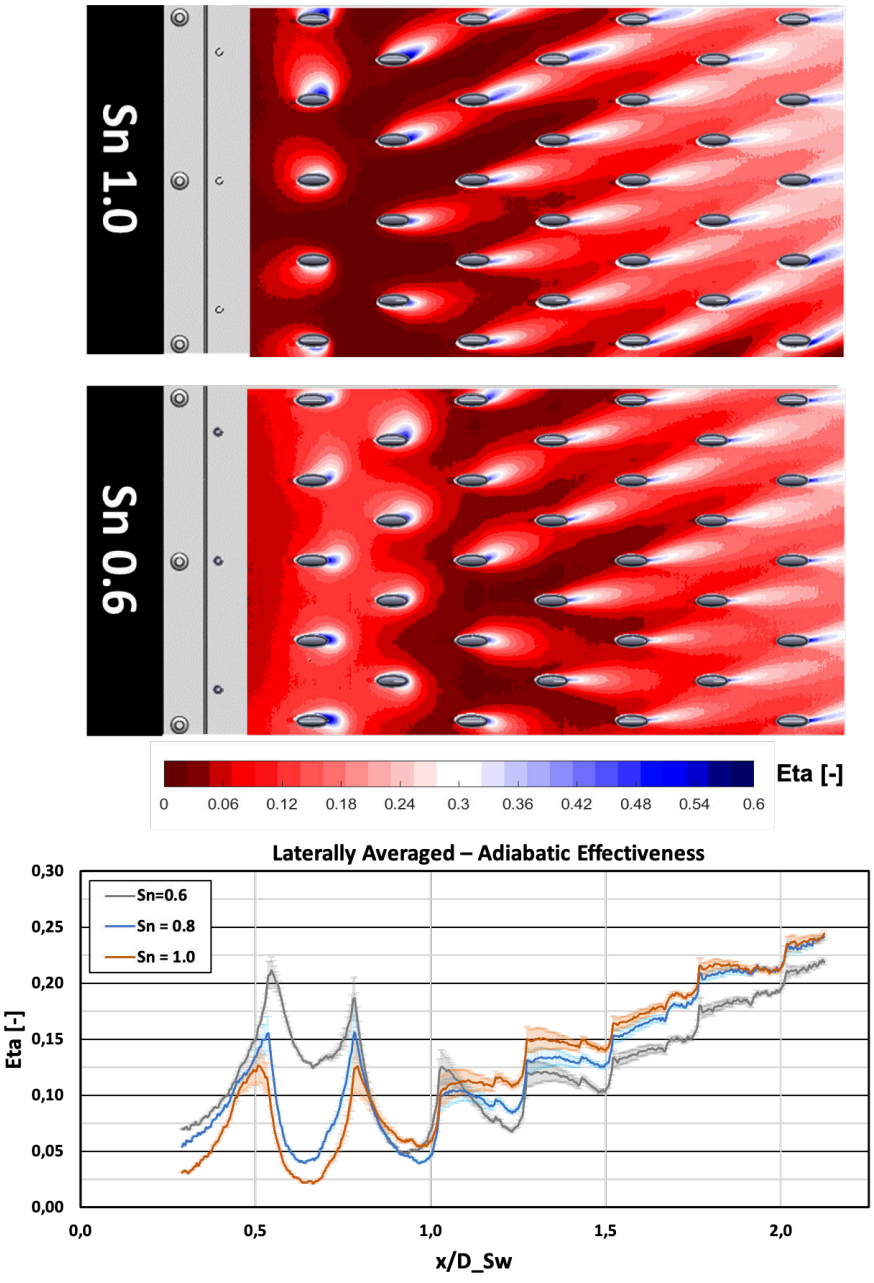

Figure 5.2: Top: adiabatic effectiveness contours: effect of Sn, test conditions A. Bottom: laterally averaged adiabatic effectiveness distribution.

and good wall coverage are measured in the ORZ. This is promoted by a continuous mixing between main and coolant flows that stationed in the ORZ.

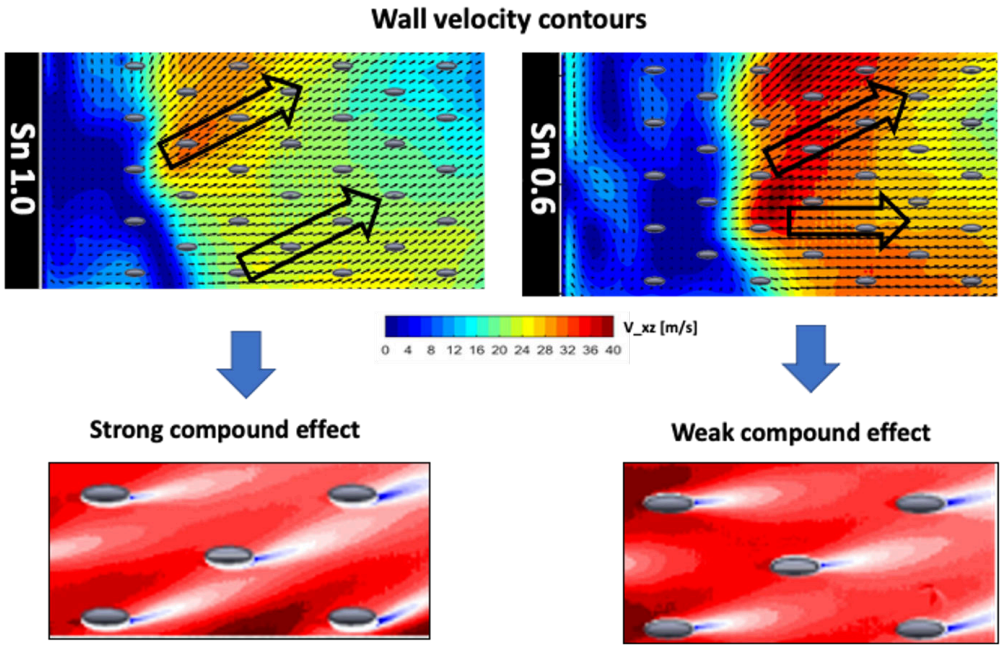

Figure 5.3: Compound effect: influence of Sn

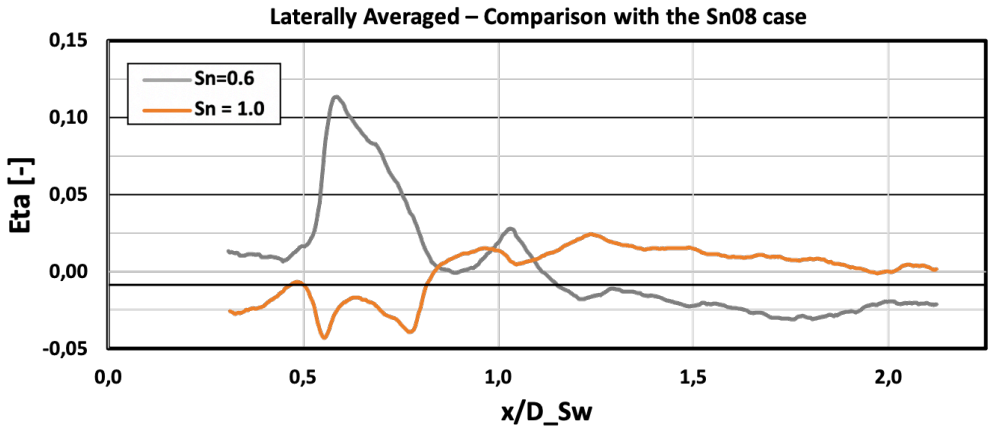

Figure 5.4: Laterally averaged adiabatic effectiveness distribution: deviation from the reference case Sn08.

The impact zone for Sn=06 is characterized by higher effectiveness values with respect to the Sn=10 case and represents a restricted surface. Moreover, as visible in the contours, the deflection of the jet tracks increases with the Sn. For both cases, in line with the reference case, the jets have very widespread traces due to the oscillations promoted by the main flow unsteadiness. The plot in the bottom part of Fig. 5.2 shown a direct comparison of the laterally averaged results by varying the Sn. Lateral mean variance bars are added along the curves. This parameter gives a measure of the homogeneity of the coolant sub-layer promoted by the cooling system. It can be seen that the coolant homogeneity increases as the Sn decreases. From $D_{sw} = 1.25$, on the other hand, the variance values start to appear similar for all the Sn cases. Always referring to the 1D plot in Fig. 5.2, it shows a particular trend: in the recirculation and impact zone, the effectiveness values increase with the decrease of the Sn. From the 4th row onwards, however, the trend reverses, and the effectiveness grows with the Sn. This phenomenon occurs due to several factors. The first one is connected to the beneficial effect of the jets flattening to the wall. In fact, immediately downstream the hole exit, the effectiveness values are higher, increasing the Sn. This is confirmed by the PIV results in terms of the jets oscillations. The carried out analysis shown that the coolant sub-layer, after the swirling main flow impact zone, is more stable if it is squashed to the liner wall by a grater Sn. Another positive effect as Sn increases is represented by the greater deflection of the jets, which creates a compound effect. This effect is explained in Fig. 5.3 for Sn=1.0 and Sn=0.6 cases. As can be seen from the velocity contours, the main flow for the Sn=1.0 case presents a more homogeneous velocity pattern with an oblique direction across the plate. For Sn=0.6, on the other hand, the component along the z-axis is lower, and in the right part of the plate, the flow has a preferential axial direction. The greater deflection of the main flow, a function of Sn, creates a positive compound effect as shown in Fig. 5.3 with a perfect superposition effect with the tracers in a staggered configuration. This phenomenon, well known in the literature [76, 77, 78], increases the effectiveness of the effusion cooling. In addition, the PIV measurements of the effusion flow showed that the turbulent mixing increased from the 3rd

row onwards as the Sn decreases, weighing all the unsteady contributions: oscillation of the jets, KH instabilities, and interaction with the main flow unsteadiness. A final comparison is shown in Fig. 5.4. The plot quantifies the difference of effectiveness with respect to the reference case for Sn=1.0 and Sn=0.6. In the ORZ and impact area, the Sn=0.6 presents an effectiveness gain up to 0.15 with respect to the Sn=1.0 case. After the impact zone as the Sn increases, for the present cooling system, the effectiveness increases with the Sn, but the difference with the reference case tends to reduces by moving away from the swirler injector. After $1.5D_{sw}$, Sn=1.0 and Sn=0.8 present the same average values. Probably, at a greater distance (outside the survey plane), Sn=0.6 will be also equal Sn=1.0 and Sn=0.6. Fig. 5.5 shows the effect of Sn on test conditions B. The differences with respect to test conditions A are those connectable to an increase (for Sn=1.0) and reduction (for Sn=0.6) of the effusion plate pressure drop $\Delta P/P_{eff}$ previously shown for the reference Sn=0.8 case. Sn=1.0 loses the benefit of the flattening of the jets (increasing the jets penetration capacity) and a lower compound effect due to a greater moment of the jets. However, these phenomena are compensated by a greater coolant mass flow rate. Overall, the ORZ and the impact zone present higher effectiveness values. Downstream, on the other hand, there is a slight reduction of the average effectiveness and the 1D curve is paired with the Sn=0.8 case already from the fourth row. Sn=0.6 presents a gain in a reduction of the jets penetration capacity, but it is compensated with a lower coolant mass flow rate. Overall, its behavior is the same as in test case A compared to Sn=0.8 and Sn=1.0.

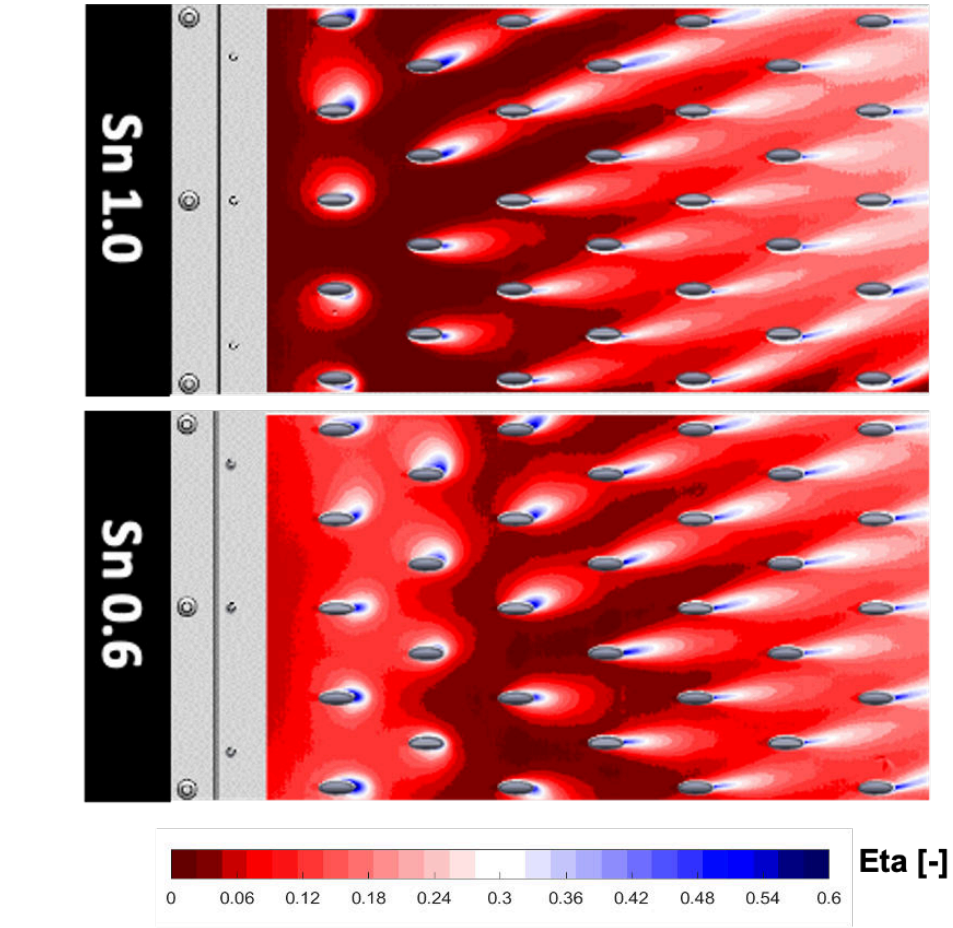

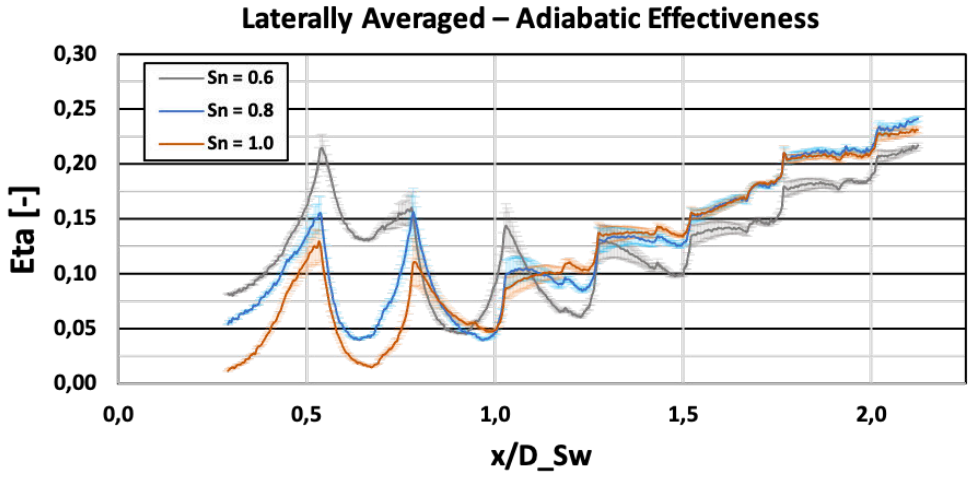

Figure 5.5: Top: adiabatic effectiveness contours: effect of Sn, test conditions B. Bottom: laterally averaged adiabatic effectiveness distribution.

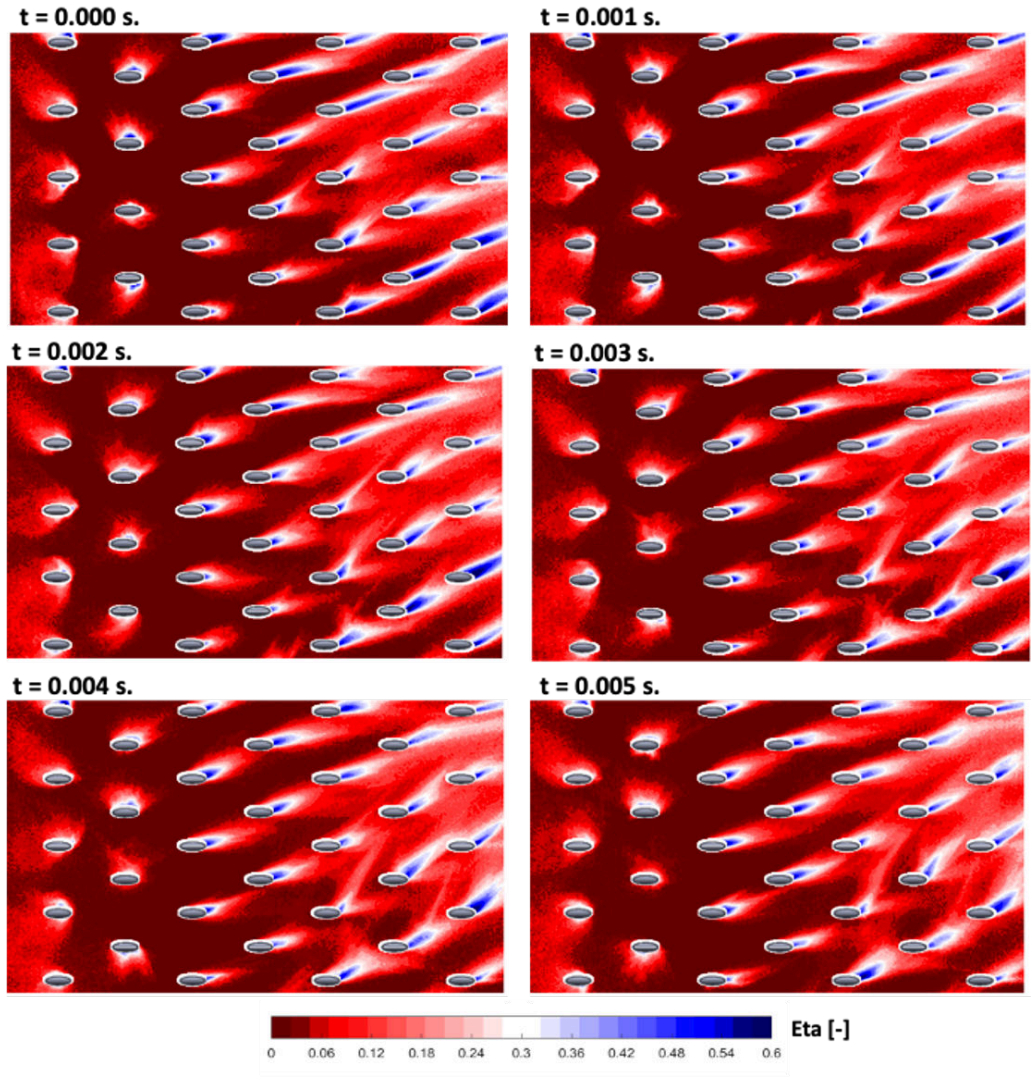

Figure 5.6: Instantaneous adiabatic effectiveness snapshots: Sn=0.8, $\Delta P/P_{eff}$=1%.

5.2 Unsteady Analysis

Fig. 5.6 shows time-resolved snapshots of the effectiveness distribution on the plate, referring to Sn=0.8, $\Delta P/P_{eff} = 1\%$ case. The contours highlight an unsteady behavior of the jets, which greatly differs from the steady-state ones shown in Fig. 5.1. For all the surveys rows, the principal remarkable

phenomena are the fluctuation of the mass flow rate ejected by the holes and the lateral oscillation of the jets trajectories. This causes frequent destruction and regeneration of the cold-layer, especially downstream of the impact zone. Furthermore, the lateral oscillations of the jets, produced by the instability of the main flow, also assume apparently chaotic and not coherent trends on the whole plate. Two descriptive statistics parameters were used to describe the unsteady behavior of the effectiveness values: the Root Mean Square and the Skewness. The equations used are the following:

$$\eta_{rms} = \sqrt{\frac{1}{N}\sum_{n=1}^{N}(\eta' - \overline{\eta})^2} \tag{5.1}$$

$$\eta_{skn} = \frac{\frac{1}{N}\sum_{n=1}^{N}(\eta' - \overline{\eta})^3}{\left(\frac{1}{N}\sum_{n=1}^{N}(\eta' - \overline{\eta})^2\right)^{3/2}} \tag{5.2}$$

where η' is the instantaneous effectiveness, $\overline{\eta}$ the time-average ones, and N the number of samples. The skewness, as shown in Fig. 5.7, is a measure of the asymmetry of the probability distribution of a real-valued random variable about its mean. The skewness value can be positive, zero, negative: negative skew commonly indicates that the tail is on the left side of the distribution, and positive skew indicates that the tail is on the right.

The RMS, quantifying the effectiveness fluctuations, is a parameter useful to detect areas and sources of turbulent mixing between the main and coolant flow. Fig. 5.8 shows the RMS values of two holes positioned in different points of the plate in the deceleration zone of the main jet. In the zoom on the left, it is possible to observe that the contribution of the counter-rotating vortex pairs, in terms of effectiveness fluctuations, is measured using the RMS analysis. Above the RMS contour, the flow field is shown in correspondence with the holes leading edge (Fig. 4.16, Ch. 5), where the structures of the CRVP can be detected. This result highlights the contribution of the counter-rotating vortices to the turbulent mixing between main and coolant flow. In

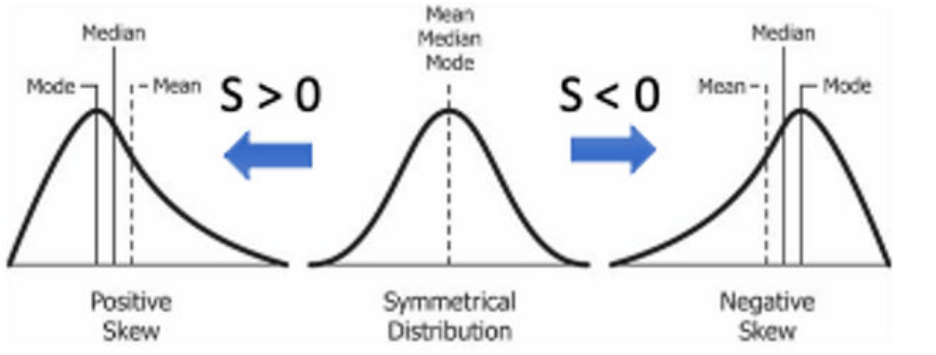

Figure 5.7: Different skewed statistical distributions.

fact, one of the main causes of reduction in effectiveness is connected to the presence of CRVP. These vortices carry air from the outer shear layer towards the core of the jet and the wall in the wake region. Moving away from the hole, the RMS values decrease and become more homogeneous in correspondence with the vorticity decay zone, where a homogeneous turbulent mixing was identified during the vorticity PIV analysis (Fig. 4.27). A different behavior is instead detected for the second analyzed hole. Also in this case, there are large effectiveness fluctuations, however, linked to the presence of a single rotating vortex. The presence of anomalous structures of this type was detected by the PIV analysis (Fig. 4.16 , Ch. 5) and is shown for the analyzed hole in the vector map on the top of the effectiveness contour. In this case, the strong deflection induced to the jet by the swirling flow limits the development of the CRVP in favor of a single rotating structure, promoting the compound effect. As can be seen from the RMS contour, the presence of this type of secondary flow structure produces intense oscillations in the wall effectiveness values. Therefore, the single rotating structure carries, from the outer jet shear-layer, air of the main flow to the wall, increasing the turbulent mixing between main and coolant flows. In addition, the oscillations of the jets, detected by the Time-Resolved analysis in Fig. 5.6, suggest a diffuse magnification of RMS values on the shown contours.

Fig. 5.1 shows the RMS results for Sn=0.8 by varying the $\Delta P/P_{eff}$. Starting from the reference case ($\Delta P/P_{eff}$=3%), the highest RMS values

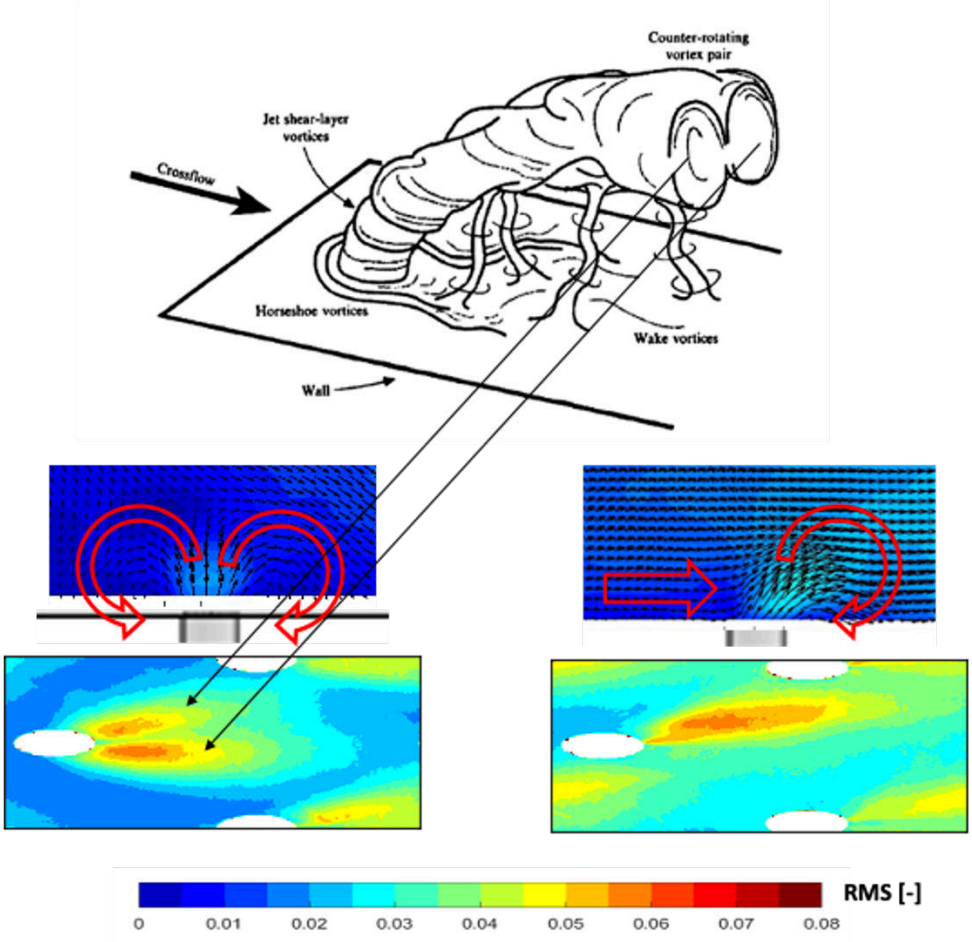

Figure 5.8: Contribution of the rotating structures of the jets to the RMS values.

are measured on the first two rows of holes. Here, in correspondence with the ORZ, the vertical oscillations of the jets cause a continuous detachment from the wall, producing large effectiveness fluctuation near the holes edges. Traces of rotating structures are not measured because the jets are in a penetration regime. Downstream of the impact zone, from the third row, the jets trajectory is closest to the wall, and the contributions of CRVP and single rotating vortices are detected. It can be noted that where the jets have a low lateral deflection, traces of CRVP are identified. In contrast, for strong lateral deflections, the formation of single rotating vortices is favored,

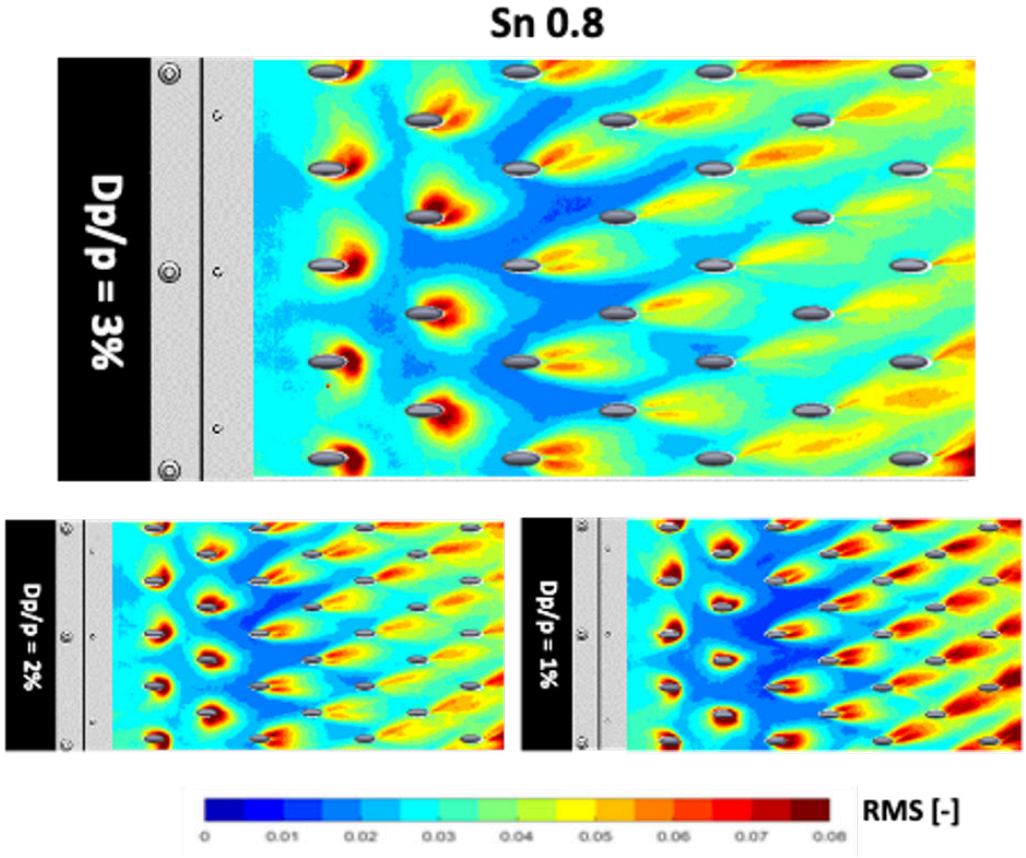

Figure 5.9: Adiabatic effectiveness RMS contours by varying the $\Delta P/P_{eff}$

due to the compound effect. Moving away from the swirler, the RMS values, and therefore the η fluctuations, become even lower. This is due to the progressive stabilization of the coolant sub-layer promoted by reducing the effect of the swirling flow and the superimposition effects of consecutive jets.

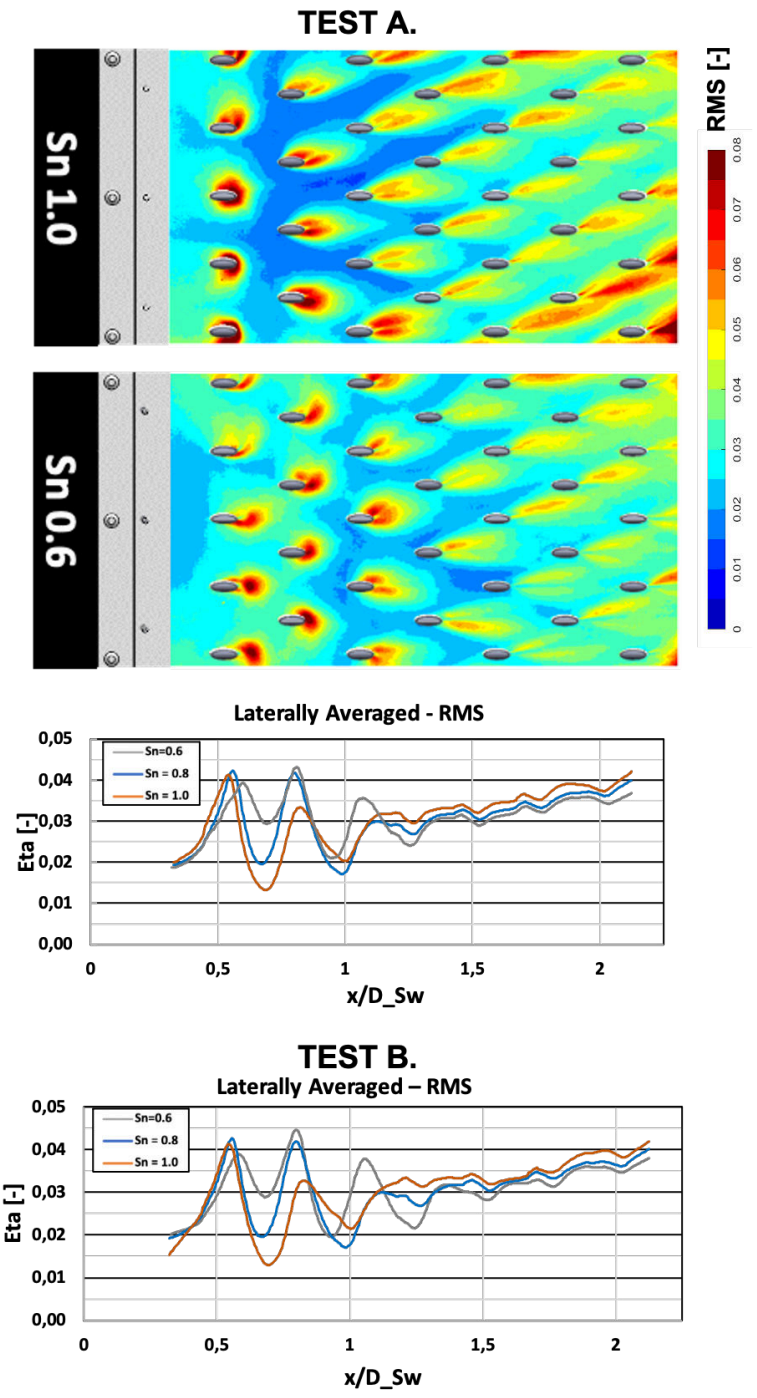

Figure 5.10: Top: adiabatic effectiveness RMS contours and laterally averaged distribution by varying the Sn; test conditions A. Bottom: laterally averaged adiabatic effectiveness distribution; test conditions B.

The reduction of $\Delta P/P_{eff}$ significantly increases the turbulent mixing between main and coolant flows with higher RMS effectiveness values, as shown in the contours (Fig. 5.1: $\Delta P/P_{eff}$=2%, $\Delta P/P_{eff}$=1%). In fact, due to the greater interaction with the main flow, the jets undergo wider lateral oscillations. Furthermore, the greater jets squash to the wall increases the CRVP and single rotating vortices interaction with the liner, creating instability: the RMS traces left by the vortices appear magnified.

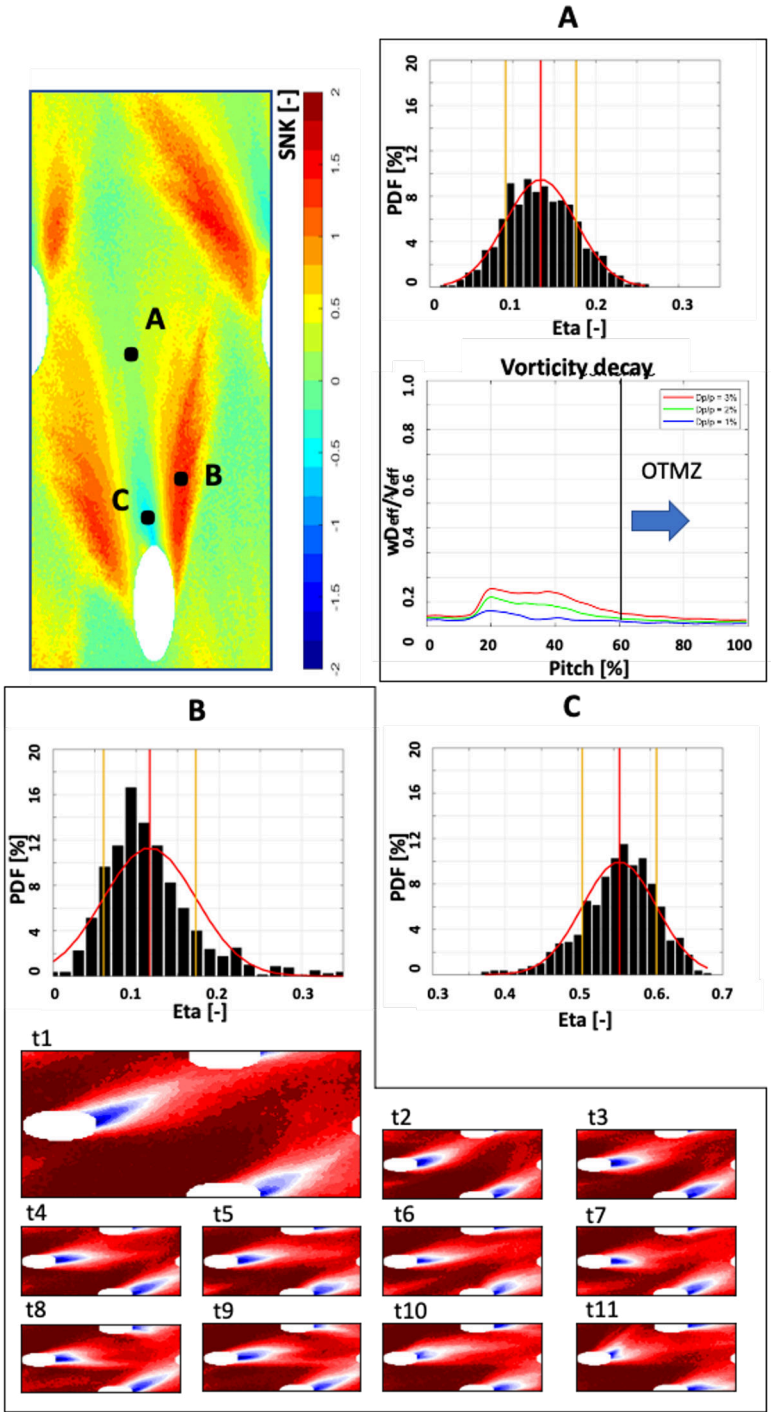

Figure 5.11: Explanation of the different skewness values in relation to the different sources of instability.

The upper part of Fig. 5.10 shows the RMS contours by varying the Sn for the test case A. Increasing the Sn, the RMS peak values increase; however, in average terms, as observed in the 1D plot in the bottom part of the figure, the overall laterally averaged results appear similar. Sn=1.0 presents a greater contribution of CRVP and single vortex due to a more intense flattening of the jets to the wall. Sn=0.6 shows a vortices traces pattern with a greater number of CRVP while Sn=1.0 with single rotating vortices; this is due to the greater deflection of the jets promoted by the greater velocity tangential component of Sn=1.0. The 1D plots, in the lower part of the figure, after the impact zone show RMS decreasing values with a lower Sn. No significant differences, in terms of the RMS contribution, are detected by varying the test conditions (Test conditions B). Fig. 5.11 shows a contour with the skewness values for the centerline hole of the 3rd row (Sn=0.8, $\Delta P/P_{eff}$=3%). Three zones, characterized by different statistical asymmetries, can be detected that well describe the unsteady behavior of the jet. To better analyze the statistical sample, the respective probability density functions (PDF) are shown for points A, B, and C of the contour. Point A is positioned on the axis of the jet trajectory, in the center of the coolant trace at about 50% of the axial pitch. Here the skewness values are close to zero, indicating a statistical symmetry of the analyzed data sample. This is also observable in the A PDF on the right. This survey point is positioned, as visible in the vorticity plot below the histogram, in the homogeneous turbulence mixing zone, where the turbulent decay of the jet vorticity is completed, and there is a diffuse mixing between the main and coolant flow. This homogeneity promotes effectiveness values arranged with a normal Gaussian distribution around the average value ($\eta = 0.14$) without showing anomalies and asymmetry in the statistical distribution. Point B is located in one of the two spots with SKN > 0 on the outer trace of the coolant jet. A positive skewness indicates that the tail of the statistical distribution is on the right. This asymmetry can be connected to the unsteady phenomenon of the jet oscillations. Below the histogram, there is a set of instant snapshots. It can be seen how large lateral oscillations characterize the coolant jet. Specifically, point B is located in a lateral area of the jet characterized by relatively low effectiveness values

but, as visible in the statistical distribution, there is a tail on the left where relatively high eta values also appear. This is due to the oscillatory nature of the jet. In fact, as can be seen from the instant snapshot, the strong lateral oscillations promote, in some instants, good coverage in this area. The more this phenomenon becomes extreme (greater oscillations of the jet) and the greater the histogram will be squeezed towards η values close to zero with a large tail to the right and therefore high skewness. Therefore, this parameter serves to identify a range of action of the jets oscillations and indicate the strong interaction between the main flow and coolant jets. These oscillations are, in fact, promoted by the instabilities of the swirling flow, as demonstrated by the PIV analysis, and suggest an increase in mixing between the main and coolant flows. In point C, immediately after the hole edge, the statistical trend shows a negative skewness. Here the η values are frequently high, with sporadic appearances of lower effectiveness. This trend suggests a relation with the phenomenon of the detachment and re-attachment of the jet to the wall due to vertical oscillations (Ch. 4, Fig. 4.23). It is also possible to hypothesize a contribution from the CRVPs or Single vortexes, which, even in this area, convey air from the main flow towards the wall. This would contribute to sporadic lower η values, linked to the unsteady behaviors of the jets, which reduce the average effectiveness.

Fig. 5.12 shows the skewness contours for Sn=0.8 by varying the $\Delta P/P_{eff}$. Starting from the reference case ($\Delta P/P_{eff}$=3%), there are different patterns of SKN values moving along the plate. Upstream of the first row of holes, the statistical distribution is symmetrical. As shown by both the average maps (Fig. 5.1) and the time-resolved snapshots (Fig. 5.6), there is a homogeneous coolant distribution both in the surface and in the time sample (low skewness). Downstream, the first two rows of holes have high and diffuse SKN values. This is connected to the strong interaction of the main flow, which generates wide oscillation and undefined jets trace on the plate. Added to this aspect, there are also significant fluctuations of the coolant mass flow rate in the swirling flow impact zone, as highlighted by the time-resolved analysis (Fig. 5.6). More downstream, from the third row, SKN distributions similar to that analyzed in Fig. 5.11 appear. There are strong SKN spots on the

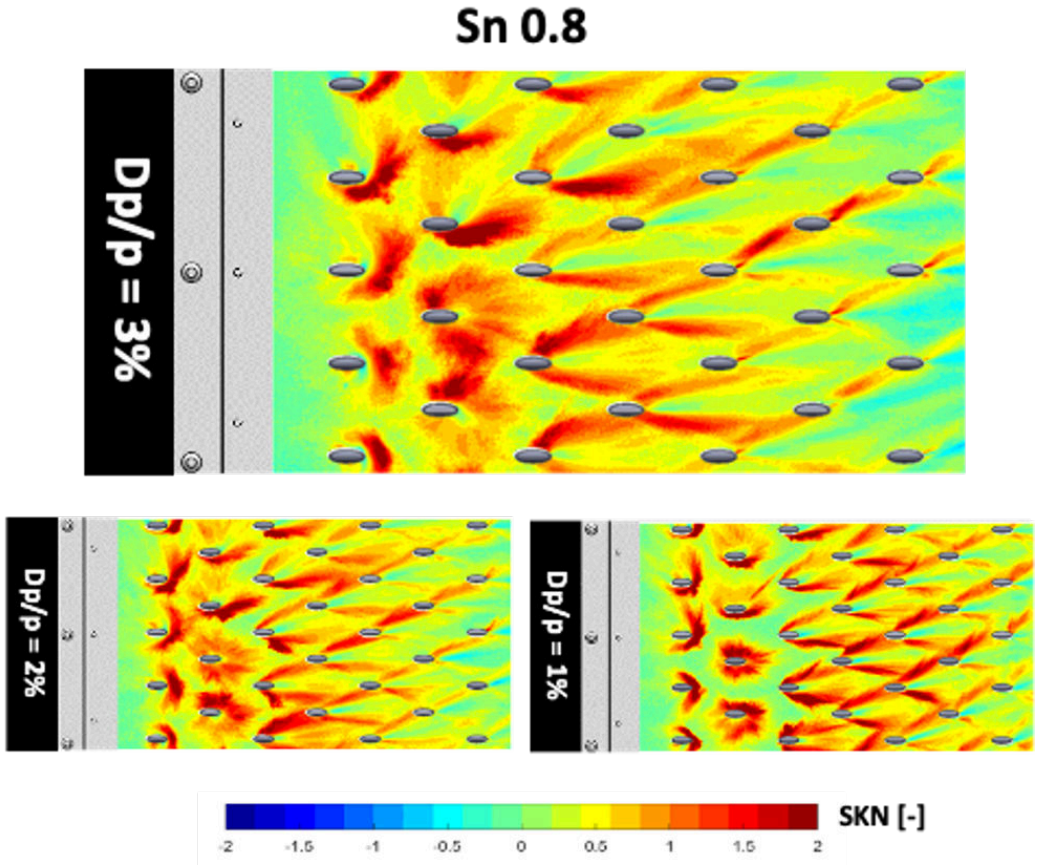

Figure 5.12: Adiabatic effectiveness SKN contours by varying the $\Delta P/P_{eff}$

outer edge of the jets traces, synonymous with strong fluctuations that suggest momentary strong increasing of coolant protection. Moving away from the swirler, the negative skewness spots decrease, thanks to a homogenization of the coolant sub-layer favored by the coolant superimposition effect. Decreasing the effusion plate feeding pressure drop (Fig. 5.12: $\Delta P/P_{eff}$=2%, $\Delta P/P_{eff}$=1%), the SKN values tend to increase. The external front of the jets is wider due to greater lateral oscillations, and the superimposition effect is reduced, showing less SKN homogeneity of the coolant sub-layer.

Fig. 5.13 shows the skewness contours by varying the Sn for test conditions A and B. Starting from case A, it can be seen that the jets have higher

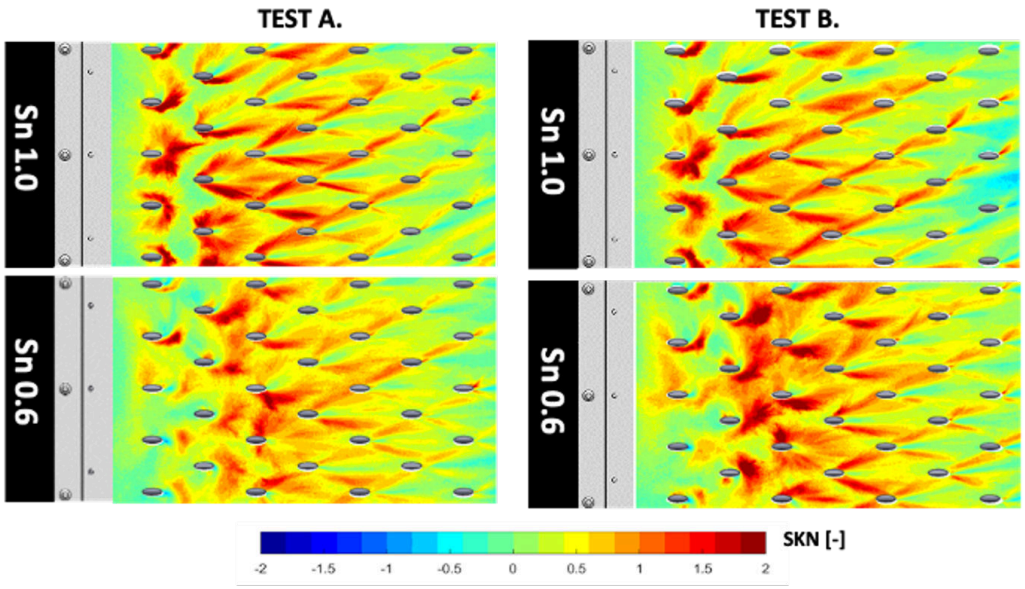

Figure 5.13: Top: adiabatic effectiveness SKN contours by varying the Sn; test conditions A and B.

SKN positive values, synonymous with larger oscillations, as Sn increases. On the other hand, the lateral oscillations increase with the tangential component of the swirling flow. Moving on to test condition B, the mass flow rate ratio imbalance reverses the trend observed in A. In this case, as the Sn decreases, the lateral oscillations of the jets appear greater for Sn06, while it is shown a more stable configuration for Sn10.

Conclusions

The shown research activity has been aimed at an experimental unsteady characterization of the interaction between effusion cooling and swirling flows in a gas turbine combustor model. To achieve this goal, a linear single sector test rig, working in ambient conditions, has been designed. It was scaled up with respect to engine dimensions to increase spatial resolution and reduce the unsteadiness frequencies. Understanding the effects of the swirling flows on the near-wall coolant sub-layer is fundamental to support the development of better effective cooling schemes and improve combustors durability. For this reason, three axial swirler injectors have been designed to assess the impact of the Swirl number parameter (Sn = 0.6 - 0.8 - 1.0) on the near-wall effusion behavior. The tests were also carried out by varying the feeding pressure drop of the effusion plate to evaluate the effect of reducing the jets momentum in the presence of swirling main flows. The measurement techniques developed for the experimental characterization were: a Time-Resolved Particle Image Velocimetry for the flow field measurements and the Fast Responding Pressure Sensitive Paint technique for those of adiabatic effectiveness. The acquisition frequency of the measurement setups (TRPIV = 5-5000Hz, FPSP = 1000Hz) and the spatial resolution allowed to detect and analyze the main instabilities of both flows. The acquired data allowed a wide range of analyzes for both measurement techniques. The flow field measurements results have been shown in terms of mean values, Time-Resolved snapshots, turbulence levels, spectral analysis of kinetic energy, integral length scale analysis, tracking of the oscillatory behavior of the cooling jets, and jets vorticity analysis. Concerning the adiabatic effectiveness measurements were shown in terms of mean values, Time-Resolved

snapshots, statistical processing with descriptive statistics parameters (Root Mean Square and Skewness) to evaluate the unsteady behavior of the jets trace on the liner. The unsteady analysis of adiabatic effectiveness made it possible to link the various instabilities of the flow field to their impact on the effectiveness values on the effusion plate.

These analyses showed that the coolant sub-layer is profoundly influenced by the swirling flow, with significant sensitivity to the Sn and the plate feeding pressure drop. Varying the Sn, the distance between the swirling jet impact zone and the injector changes. Such distance increases when the Sn reduces. This modifies the relative position of the rows of effusion holes with respect to the principal features of the main flow close to the wall: the outer recirculation zone, and the swirling main jet impact, re-acceleration and deceleration zones. From a steady and unsteady point of view, the behavior of the jets varies greatly in correspondence with these different wall areas. It can be summarized that the analysis showed that the jets behavior is strongly affected by the swirling flow and its swirl number in terms of deflection of the jets trajectory, unsteady jets oscillatory behavior, and modification of the steady and unsteady flow structures of the jets: the weakening of the Kelvin-Helmholtz instabilities, destruction of the Counter Rotating Vortex Pairs substituted by new secondary flow structures of the single rotating vortex type. The effects of the swirl number on these behaviors of the coolant sub layer are manifold, presenting many trends. In average terms, an increase of Sn is associated with a more significant deviation of the trajectory of the jets. Downstream of the impact zone, when Sn is higher, the jets are more squashed to the wall, and their vertical oscillations are reduced. Consequently, the stability of the coolant sub-layer increases, producing benefits in effectiveness values. On the other hand, in the ORZ in reverse flow conditions, the jets are detached from the wall and are affected by wide oscillations which increases with the Sn. In general, with an increase of the lateral jets oscillations, downstream the swirling flow impact zone, the adiabatic coverage will become more smoothed and homogeneous, but the overall mixing with the main flow increases. Reducing the Sn, the shear layer vorticity of

the coolant jets is less affected by the main flow: higher values of vorticity connected to the KH instabilities were measured. This means that, as the Sn decreases, the turbulent contribution of the jets increases in the coolant sub-layer, promoting the mixing with the main flow and a reduction of the film effectiveness. Furthermore, with the statistical analysis of the adiabatic effectiveness values, the contribution promoted by the CRVP and the single rotating vortices in terms of wall effectiveness fluctuation was identified. Finally, by reducing the feeding pressure drop of the plate, the mixing increases significantly between coolant and the main flow.

To summarize, a strong impact of the Sn on the effusion flow was recognized by analyzing the fluid mechanisms that lead the interaction between main and coolant flow. The measurements made it possible to obtain deep knowledge about the unsteady interaction between swirling main and coolant flow for a gas turbine combustor model. These results also constitute a large database for experimental and numerical comparisons in a context, as shown by the bibliographic analysis, which is relatively lacking in data, especially of the unsteady type. The simplicity of the geometry and operating conditions makes the collected data useful for validating numerical and CFD modeling methods of cooling systems. Furthermore, the high spatial resolution and frequency results, synthesized statistically, allow to evaluate the predictive capabilities of numerical analysis of complex unsteady fluid dynamics mechanisms of this type. The results also provide relevant information in terms of strategy for designing combustor liners. The various zones of the liner that interact with the swirling flow differently (ORZ, impact zone, deceleration zone) suggest using different geometric patterns of effusion holes in terms of porosity and inclination. In the ORZ, an increase in the holes inclination would bring benefits in film effectiveness due to the reverse flow conditions of the main flow with respect to the jets trajectories. Furthermore, in the ORZ and the swirling jet impact zone, an increase in the holes density is necessary due to the strong interaction and flow mixing with the swirling flow. Moving away from the swirler, a reduction in the liner porosity could be applied, taking into account the superimposing effects and the coolant sub-layer stability. Finally, the data showed also represents one of the re-

search contributions of the University of Florence within the SOPRANO European project. One of its objectives, within which the work of this thesis is placed, is the increase of the reliability of cooling design for durable combustors through the improvement of the accuracy in the prediction of the metal temperature of combustors liners and the cooling systems effectiveness by using new experimental measurement on realistic test cases.

Bibliography

[1] A. H. Lefebvre. *Gas Turbine Combustion*. Taylor & Francis, 1998.

[2] R. Krewinkel. A review of gas turbine effusion cooling studies. *International Journal of Heat and Mass Transfer*, 66:706–722, November 2013. ISSN 0017-9310.

[3] N. Syred and J. M. Be r. Combustion in swirling flows: A review. *Combustion and Flame*, 23(2):143–201, October 1974. ISSN 0010-2180.

[4] O. Lucca-Negro and T. O'Doherty. Vortex breakdown: a review. *Progress in Energy and Combustion Science*, 27(4):431–481, January 2001. ISSN 0360-1285.

[5] Zakaria Mansouri, Aouissi Mokhtar, and Toufik Boushaki. A numerical study of swirl effects on the flow and flame dynamics in a lean premixed combustor. *International Journal of Heat and Technology*, 34:227–235, 06 2016.

[6] Dmitriy Markovich, S. Abdurakipov, Leonid Chikishev, Vladimir Dulin, and Kemal Hanjalic. Comparative analysis of low- and high-swirl confined flames and jets by proper orthogonal and dynamic mode decompositions. *Physics of Fluids*, 26:065109, June 2014.

[7] Ilker Yilmaz. Effect of swirl number on combustion characteristics in a natural gas diffusion flame. *Journal of Energy Resources Technology*, 135:042204, December 2013.

[8] St M., R. Sadanandan, and W. Meier. Phase-resolved characterization of vortex-flame interaction in a turbulent swirl flame. *Experiments in Fluids*, 51(4):1153–1167, October 2011. ISSN 1432-1114.

[9] Hao Qin, Yuzhen Lin, and Jibao Li. Precessing motion in stratified radial swirl flow. *Chinese Journal of Aeronautics*, 29(2):386–394, April 2016. ISSN 1000-9361.

[10] Edward Canepa, Pasquale Di Martino, Piergiorgio Formosa, Marina Ubaldi, and Pietro Zunino. Unsteady aerodynamics of an aeroengine double swirler lean premixing prevaporizing burner. *J. Eng. Gas Turbines Power*, 128(1):29–39, July 12/7. ISSN 0742-4795.

[11] M. Berrino, D. Lengani, F. Satta, M. Ubaldi, P. Zunino, S. Colantuoni, and P. Di Martino. Investigation of the dynamics of an ultra low nox injection system by pod data post-processing. Number 56680, page V04AT04A049, 2015.

[12] Rohit Sharma, Fabio Cozzi, and Aldo Coghe. *Phase-averaged characterization of turbulent isothermal free swirling jet after vortex breakdown.* July 2016.

[13] H. Ek, I. Chterev, N. Rock, B. Emerson, J. Seitzman, T. Lieuwen, N. Jiang, and W. Proscia. Feature extraction from time resolved reacting flow data sets, July 12/7. ISSN 978-0-7918-5106-7.

[14] Theodore Providakis, Philippe Scouflaire, Laurent Zimmer, and S bastien Ducruix. Time-resolved piv measurements applied to a non-reactive dodecane-air mixture in a two-staged multi-injection burner. pages 5–8, August 2010.

[15] Richard J. Goldstein, Thomas F. Irvine, and James P. Hartnett. Film cooling. In *Advances in Heat Transfer*, volume 7, pages 321–379. Elsevier, January 1971.

[16] J. Han, S. Dutta, and S. Ekkad. *Gas Turbine Heat Transfer and Cooling Technology*, pages 129–249. Taylor & Francis, 2000.

[17] T. F. Fric and A. Roshko. Vortical structure in the wake of a transverse jet. *Journal of Fluid Mechanics*, 279:1–47, 1994.

[18] K. Thole, M. Gritsch, A. Schulz, and S. Wittig. Flowfield measurements for film-cooling holes with expanded exits. *ASME Journal of Turbomachinery*, 120(2):327–336, April 1998.

[19] J. J. Scrittore, K. A. Thole, and S.W. Burd. Investigation of velocity profiles for effusion cooling of a combustor liner. *Proc. ASME Turbo Expo*, (GT2006-90532), 2006.

[20] Robert P. Schroeder and Karen A. Thole. Thermal field measurements for a shaped hole at low and high freestream turbulence intensity. *J. Turbomach*, 139(2), August 2017. ISSN 0889-504X.

[21] K. Kadotani and R. J. Goldstein. On the nature of jets entering a turbulent flow: Part a–jet-mainstream interaction. *J. Eng. Power*, 101 (3):459–465, August 12/8. ISSN 0022-0825.

[22] K. Kadotani and R. J. Goldstein. On the nature of jets entering a turbulent flow: Part b–film cooling performance. *J. Eng. Power*, 101 (3):466–470, August 12/8. ISSN 0022-0825.

[23] A. Kohli and D. G. Bogard. Effects of very high free-stream turbulence on the jet-mainstream interaction in a film cooling flow. *J. Turbomach*, 120(4):785–790, August . ISSN 0889-504X.

[24] Christian Saumweber, Achmed Schulz, and Sigmar Wittig. Free-stream turbulence effects on film cooling with shaped holes. *J. Turbomach*, 125 (1):65–73, August 2003. ISSN 0889-504X.

[25] Christian Saumweber and Achmed Schulz. Free-stream effects on the cooling performance of cylindrical and fan-shaped cooling holes. *J. Turbomach*, 134(6), August 2012. ISSN 0889-504X.

[26] M. K. Eberly and K. A. Thole. Time-resolved film-cooling flows at high and low density ratios. *ASME Journal of Turbomachinery*, 136(6): 061003–061003–11, November 2013.

[27] M. Straubald, K. Schmid, M. Hagen, and M. Pfitzner. Experimental and numerical investigation of turbulent mixing in film cooling applications. In *Proc. ASME Turbo Expo*, number GT2017-64650, 2017.

[28] Michael Strau wald, Tobias Sander, Amirabas Bakhtiari, and Michael Pfitzner. High-speed velocity measurements of film cooling applications at high-turbulence main flow conditions, August 2018.

[29] Wenwu Zhou, Di Peng, Xin Wen, Yingzheng Liu, and Hui Hu. Unsteady analysis of adiabatic film cooling effectiveness behind circular, shaped, and sand-dune-inspired film cooling holes: Measurement using fast-response pressure-sensitive paint. *International Journal of Heat and Mass Transfer*, 125:1003–1016, October 2018. ISSN 0017-9310.

[30] Wenwu Zhou, Han Chen, Yingzheng Liu, Xin Wen, and Di Peng. Unsteady analysis of adiabatic film cooling effectiveness for discrete hole with oscillating mainstream flow. *Physics of Fluids*, 30(12):127103, December 2020. ISSN 1070-6631.

[31] Mohamed Qenawy, Wenwu Zhou, Han Chen, Hongyi Shao, Di Peng, and Yingzheng Liu. *Unsteady Analysis of Adiabatic Film Cooling Effectiveness Behind a Row of Circular Holes Fed by Internal Crossflow.* June 2019.

[32] C. Abram, P. Schreivogel, B. Fond, M. Straubald, M. Pfitzner, and F. Beyrau. Investigation of film cooling flows using thermographic particle image velocimetry at a 6 khz repetition rate. *18th International Symposium on the application of Laser and Imaging Techniques to Fluid Mechanics*, July 2016.

[33] B. Wurm, A. Schulz, H.J. Bauer, and M. Gerendas. Impact of swirl flow on the cooling performance of an effusion cooled combustor liner. *ASME J Eng Gas Turb Power*, 134(12):121503–121503, 2012.

[34] B. Wurm, A. Schulz, and Hans-Joerg Bauer. *A New Test Facility for Investigating the Interaction Between Swirl Flow and Wall Cooling Films in Combustors*, volume 3. January 2009.

[35] A. Andreini, G. Caciolli, B. Facchini, and F. Picchi, A. andTurrini. Experimental investigation of the flow field and the heat transfer on a scaled cooled combustor liner with realistic swirling flow generated by a lean-burn injection system. *ASME J. Turbomach.*, 137(3):031012–031012, 2014.

[36] A. Andreini, R. Becchi, B. Facchini, L. Mazzei, A. Picchi, and F. Turrini. Adiabatic effectiveness and flow field measurements in a realistic effusion cooled lean burn combustor. *ASME J Eng Gas Turb Power*, 138(3): 031506–031506–11, September 2015.

[37] Antonio Andreini, Riccardo Becchi, Bruno Facchini, Alessio Picchi, and Antonio Peschiulli. The effect of effusion holes inclination angle on the adiabatic film cooling effectiveness in a three-sector gas turbine combustor rig with a realistic swirling flow. *International Journal of Thermal Sciences*, 121:75–88, 2017. ISSN 1290-0729.

[38] Yongbin Ji, Bing Ge, Zhongran Chi, and Shusheng Zang. Overall cooling effectiveness of effusion cooled annular combustor liner at reacting flow conditions. *Applied Thermal Engineering*, 130:877–888, February 2018. ISSN 1359-4311.

[39] M. Greifenstein, J. Hermann, B. Boehm, and A. Dreizler. Flame-cooling air interaction in an effusion-cooled model gas turbine combustor at elevated pressure. *Experiments in Fluids*, 60(1):10, December 2018. ISSN 1432-1114.

[40] J. Hermann, M. Greifenstein, B. Boehm, and A. Dreizler. Experimental investigation of global combustion characteristics in an effusion cooled single sector model gas turbine combustor. *Flow, Turbulence and Combustion*, 102(4):1025–1052, April 2019. ISSN 1573-1987.

[41] ASME. Measurement uncertainty. *Instrument and Apparatus, Vol. ANSI/ASME PTC 19.1-1985 of Performance Test Code*, 1985.

[42] S. J. Kline and F. A. McClintock. Describing uncertainties in single sample experiments. *Mechanical Engineering*, 1953.

[43] J. Westerweel. Fundamentals of digital particle image velocimetry. *Meas. Sci. Technol.*, 8:1379–1392, 1997.

[44] R J Adrian. Dynamic ranges of velocity and spatial resolution of particle image velocimetry. *Measurement Science and Technology*, 8(12):1393–1398, dec 1997.

[45] R. J. Adrian. Twenty years of particle image velocimetry. *Experiments in Fluids*, 39(2):159–169, August 2005. ISSN 1432-1114.

[46] Arne Henning and Klaus Ehrenfried. Frequency resolution of high-speed piv. *ODAS 2007 - 8th ONERA-DLR Aerospace Symposium*, pages 1–12, January 2007.

[47] A. R. Oxlade, P. C. Valente, B. Ganapathisubramani, and J. F. Morrison. Denoising of time-resolved piv for accurate measurement of turbulence spectra and reduced error in derivatives. *Experiments in Fluids*, 53(5):1561–1575, November 2012. ISSN 1432-1114.

[48] Steven Beresh. *Denoising 400-kHz Postage-Stamp PIV using Uncertainty Quantification.* January 2018.

[49] J r me V tel, Andr Garon, and Dominique Pelletier. Denoising methods for time-resolved piv measurements. *Experiments in Fluids*, 51(4):893–916, October 2011. ISSN 1432-1114.

[50] R. Mei. Velocity fidelity of flow tracer particles. *Experiments in Fluids*, 22(1):1–13, November 1996. ISSN 1432-1114.

[51] C.J. Kahler, B. Sammler, and J. Kompenhas. Generation and control of tracer particles for optical flow investigations in air. *Experiments in fluids*, 33, 2002.

[52] Dantec Dynamics. *FlowManager software and Introduction to PIV Instrumentation.* 2000.

[53] M. Raffel, C. E. Willert, and J. Kompenhans. *Particle Image Velocimetry - A pratical guide.* Springer, 1997.

[54] K. Navarra. Development of the pressure- sensitive paint (psp) technique for advanced turbomachinery applications. 1997.

[55] J. W. Gregory, Keisuke Asai, Masaharu Kameda, Tianshu Liu, and J. P. Sullivan. A review of pressure-sensitive paint for high-speed and unsteady aerodynamics. *Proceedings of The Institution of Mechanical Engineers Part G-journal of Aerospace Engineering - PROC INST MECH ENG G-J A E*, 222, February 2008.

[56] Edward T. Schairer. Optimum thickness of pressure-sensitive paint for unsteady measurements. *AIAA Journal*, 40(11):2312–2318, December 2012. ISSN 0001-1452.

[57] Hirotaka Sakaue, James W. Gregory, John P. Sullivan, and Surya Raghu. Porous pressure-sensitive paint for characterizing unsteady flowfields. *AIAA Journal*, 40(6):1094–1098, December 2002. ISSN 0001-1452.

[58] T. V. Jones. Theory for the use of foreign gas in simulating film cooling. *International Journal of Heat and Fluid Flow*, 20(3):349–354, June 1999. ISSN 0142-727X.

[59] Diganta P. Narzary, Kuo-Chun Liu, Akhilesh P. Rallabandi, and Je-Chin Han. Influence of coolant density on turbine blade film-cooling using pressure sensitive paint technique. *J. Turbomach*, 134(3), April 12. ISSN 0889-504X.

[60] R. J. Goldstein and H. H. Cho. A review of mass transfer measurements using naphthalene sublimation. *Experimental Thermal and Fluid Science*, 10(4):416–434, May 1995. ISSN 0894-1777.

[61] R. L. Simpson and R. L. Field. A note on the turbulent schmidt and lewis numbers en a boundary layer. *International Journal of Heat and Mass Transfer*, 15(1):177–180, January 1972. ISSN 0017-9310.

[62] D. Charbonnier, P. Ott, M. Jonsson, F. Cottier, and Th. Ko¨bke. Experimental and numerical study of the thermal performance of a film cooled turbine platform, April 12/4. ISSN 978-0-7918-4884-5.

[63] G. Caciolli, B. Facchini, A. Picchi, and L. Tarchi. Comparison between psp and tlc steady state techniques for adiabatic effectiveness measurement on a multiperforated plate. *Experimental Thermal and Fluid Science*, 48:122–133, July 2013. ISSN 0894-1777.

[64] Brandon Wilson and Barton Smith. Taylor-series and monte-carlo-method uncertainty estimation of the width of a probability distribution based on varying bias and random error. *Measurement Science and Technology*, 24:35301–11, March 2013.

[65] Chris Freitas. *Verification and Validation in Computational Fluid Dynamics and Heat Transfer: PTC 61.* January 2006.

[66] *Appendix B: Taylor Series Method (TSM) for Uncertainty Propagation*, pages 257–269. John Wiley & Sons, Ltd, 2009. ISBN 9780470485682.

[67] *Uncertainty Analysis Particle Imaging Velocimetry - ITTC Recommended Procedures and Guidelines.* ITTC, 2008.

[68] John J Charonko and Pavlos P Vlachos. Estimation of uncertainty bounds for individual particle image velocimetry measurements from cross-correlation peak ratio. *Measurement Science and Technology*, 24 (6):065301, apr 2013.

[69] Tim Persoons. Time-resolved high-dynamic-range particle image velocimetry using local uncertainty estimation. *AIAA Journal*, 53(8): 2164–2173, 2015. doi: 10.2514/1.J053651.

[70] Bernhard Wieneke. PIV uncertainty quantification from correlation statistics. *Measurement Science and Technology*, 26(7):074002, jun 2015. doi: 10.1088/0957-0233/26/7/074002.

[71] Edward Canepa, Pasquale Di Martino, Piergiorgio Formosa, Marina Ubaldi, and Pietro Zunino. Unsteady aerodynamics of an aeroengine double swirler lean premixing prevaporizing burner. *J. Eng. Gas Turbines Power*, 128(1):29–39, 2008. ISSN 0742-4795.

[72] Jacques Lewalle and David Ashpis. Estimation of time scales in unsteady flows in a turbomachinery rig. March 2004.

[73] Stephen B. Pope. *Turbulent Flows*. Cambridge University Press, 2000. doi: 10.1017/CBO9780511840531.

[74] A. Bakhtiari M.Pfitzner M. Strau wald, T. Sander. High-speed velocity measurements of film cooling applications at high-turbulence main flow conditions. In *Proc. ASME Turbo Expo*, 2018.

[75] T. Lenzi, L. Palanti, A. Picchi, T. Bacci, L. Mazzei, A. Andreini, B. Facchini, and I. Vitale. Time-resolved flow field analysis of effusion cooling system with representative swirling main flow. *Journal of Turbomachinery*, 2020.

[76] M. Surace and L. Toni. Test conditions for effusion cooling geometries and compound impigement arrays. *Intellect DM*, (Avio - UFLOR Internal Report), 2006.

[77] B. Sen, D. L. Schmidt, and D. G. Bogard. Film cooling with compound angle holes: Heat transfer. *ASME J. Turbomach.*, 118:800–806, 1996.

[78] D. L. Schmidt, B. Sen, and D. G. Bogard. Film cooling with compound angle holes: Adiabatic effectiveness. *J. Turbomach*, 118(4):807–813, 1996. ISSN 0889-504X.